
Electronic Theses and Dissertations, 2004-2019

2010

Fabrication Of Functional Nanostructures Using Polyelectrolyte Nanocomposites And Reduced Graphene Oxide Assemblies

Anindarupa Chunder
University of Central Florida

 Part of the [Chemistry Commons](#)

Find similar works at: <https://stars.library.ucf.edu/etd>

University of Central Florida Libraries <http://library.ucf.edu>

This Doctoral Dissertation (Open Access) is brought to you for free and open access by STARS. It has been accepted for inclusion in Electronic Theses and Dissertations, 2004-2019 by an authorized administrator of STARS. For more information, please contact STARS@ucf.edu.

STARS Citation

Chunder, Anindarupa, "Fabrication Of Functional Nanostructures Using Polyelectrolyte Nanocomposites And Reduced Graphene Oxide Assemblies" (2010). *Electronic Theses and Dissertations, 2004-2019*. 4231. <https://stars.library.ucf.edu/etd/4231>

FABRICATION OF FUNCTIONAL NANOSTRUCTURES USING POLYELECTROLYTE
NANOCOMPOSITES AND REDUCED GRAPHENE OXIDE ASSEMBLIES

by

ANINDARUPA CHUNDER

B.Tech. The University of Calcutta, India. 2003

A dissertation submitted in partial fulfillment of the requirements
for the degree of Doctor of Philosophy
in the Department of Chemistry
in the College of Sciences
at the University of Central Florida
Orlando, Florida

Summer Term

2010

Major Professor: Lei Zhai

© 2010 Anindarupa Chunder

ABSTRACT

A wide variety of nanomaterials ranging from polymer assemblies to organic and inorganic nanostructures (particles, wires, rods etc) have been actively pursued in recent years for various applications. The synthesis route of these nanomaterials had been driven through two fundamental approaches - 'Top down' and 'Bottom up'. The key aspect of their application remained in the ability to make the nanomaterials suitable for targeted location by manipulating their structure and functionalizing with active target groups. Functional nanomaterials like polyelectrolyte based multilayered thin films, nanofibres and graphene based composite materials are highlighted in the current research.

Multilayer thin films were fabricated by conventional dip coating and newly developed spray coating techniques. Spray coating technique has an advantage of being applied for large scale production as compared to the dip coating technique. Conformal hydrophobic/hydrophilic and superhydrophobic/hydrophilic thermal switchable surfaces were fabricated with multilayer films of poly(allylaminehydrochloride) (PAH) and silica nanoparticles by the dip coating technique, followed by the functionalization with thermosensitive polymer-poly(*N*-isopropylacrylamide)(PNIPAAm) and perfluorosilane. The thermally switchable superhydrophobic/ hydrophilic polymer patch was integrated in a microfluidic channel to act as a stop valve. At 70 °C, the valve was superhydrophobic and stopped the water flow (close status) while at room temperature, the patch became hydrophilic, and allowed the flow (open status). Spray-coated multilayered film of poly(allylaminehydrochloride) (PAH) and silica nanoparticles was fabricated on polycarbonate substrate as an anti-reflection (AR) coating. The adhesion between the substrate and the coating was enhanced by treating the polycarbonate surface with

aminopropyltrimethoxysilane (APTS) and sol-gel. The coating was finally made abrasion-resistant with a further sol-gel treatment on top of AR coating, which formed a hard thin scratch-resistant film on the coating. The resultant AR coating could reduce the reflection from 5 to 0.3% on plastic.

Besides multilayered films, the fabrication of polyelectrolyte based electrospun nanofibers was also explored. Ultrathin nanofibers comprising 2-weak polyelectrolytes, poly(acrylic acid) (PAA) and poly(allylaminehydrochloride) (PAH) were fabricated using the electrospinning technique and methylene blue (MB) was used as a model drug to evaluate the potential application of the fibers for drug delivery. The release of MB was controlled in a nonbuffered medium by changing the pH of the solution. Temperature controlled release of MB was obtained by depositing temperature sensitive PAA/poly(*N*-isopropylacrylamide) (PNIPAAm) multilayers onto the fiber surfaces. The sustained release of MB in a phosphate buffered saline (PBS) solution was achieved by constructing perfluorosilane networks on the fiber surfaces as capping layers. The fiber was also loaded with a real life anti-depressant drug (2,3-tertbutyl-4-methoxyphenol) and fiber surface was made superhydrophobic. The drug loaded superhydrophobic nanofiber mat was immersed under water, phosphate buffer saline and surfactant solutions in three separated experiments. The rate of release of drug was monitored from the fiber surface as a result of wetting with different solutions. Time dependent wetting of the superhydrophobic surface and consequently the release of drug was studied with different concentrations of surfactant solutions. The results provided important information about the underwater superhydrophobicity and retention time of drug in the nanofibers.

The nanostructured polymers like nanowires, nanoribbons and nanorods had several other applications too, based on their structure. Different self-assembled structures of semiconducting

polymers showed improved properties based on their architectures. Poly(3-hexylthiophene) (P3HT) supramolecular structures were fabricated on P3HT-dispersed reduced graphene oxide (RGO) nanosheets. P3HT was used to disperse RGO in hot anisole/N, N-dimethylformamide solvents, and the polymer formed nanowires on RGO surfaces through a RGO induced crystallization process. The Raman spectroscopy confirmed the interaction between P3HT and RGO, which allowed the manipulation of the composite's electrical properties. Such a bottom-up approach provided interesting information about graphene-based composites and inspired to study the interaction between RGO and the molecular semiconductor-tetrasulphonate salt of copper phthalocyanine (TSCuPc) for nanometer-scale electronics. The reduction of graphene oxide in presence of TSCuPc produced a highly stabilized aqueous composite ink with monodispersed graphene sheets. To demonstrate the potential application of the donor (TSCuPc) –acceptor (graphene) composite, the RGO/TSCuPc suspension was successfully incorporated in a thin film device and the optoelectronic property was measured. The conductivity (dark current) of the composite film decreased compared to that of pure graphene due to the donor molecule incorporation, but the photoconductivity and photoresponsivity increased to an appreciable extent. The property of the composite film overall improved with thermal annealing and optimum loading of TSCuPc molecules.

*Dedicated
to
My loving parents*

ACKNOWLEDGMENTS

First I must give thanks to the almighty, my creator who has given me life and guided me in the paths of righteousness. May my work honor and glorify His name.

As I complete my dissertation, I take the pleasant opportunity to convey my gratitude to the people who contributed to my success directly and indirectly.

My deepest gratitude goes to my parents for their unconditional love and support throughout my life. I am indebted to my mother. This dissertation would not have been possible without her encouragement and sacrifices. I thank my father for his love and care. He is the most successful person I have ever seen, who wrote his own fortune with sincerity and hard-work. To my parents, I dedicate my dissertation.

I would like to express my sincere gratitude to my advisor Professor Lei Zhai for his support and encouragement. It has been an honor to be his 1st PhD student. I thank him for his contributions of time, ideas, and funding to make my PhD experience productive and stimulating. The joy and enthusiasm he has for his research was contagious and motivational for me, even during tough times in the PhD pursuit. I am also thankful for the excellent example he has provided as a successful scientist, professor and overall an excellent human being.

I am grateful to my committee members Professor Qun Huo, Professor Andre J. Gesquiere, Professor Diego J. Diaz and Professor Linan An for their detailed review, constructive criticism and valuable advices during my proposal and dissertation defense. I would like to thank my group members Sourangsu, Binh, Qiang, Ken, Hoa, Carl, Dr. Weifeng Fei, Dr. Jianhua Liu, Dr. Jianhua Jou and Dr. Raj Sharma for providing me with a friendly and convivial work

environment to conduct my research. I express my sincere thanks to my collaborators, Professor Hyoung Jin Cho, Professor Saiful I. Khondaker, Dr. Ghanshyam Londe, Dr. Tanusri Pal, Dr. Surajit Ghosh, Daeha Joung and Vipra Dhir. The associated experience broadened my perspective on various scientific and practical aspects of several research fields. I would also like to thank a friendly undergraduate student in our lab, Kenneth Etcheverry, who worked with me in couple of research projects. I appreciate his enthusiasm, intensity and willingness in conducting experiments. I owe my sincere thanks to my childhood teacher whose guidance was and will always be a constant source of knowledge and enthusiasm in my life. I thank my friends and colleagues at my previous work place 'Akzo Nobel' for encouraging me to pursue doctoral research. I also acknowledge the fruitful discussions, help and suggestions from all of my undergraduate mentors, PhD committee members, research group members and collaborators.

My special thanks goes to my loving, supportive, encouraging, and patient husband Debasis. His support, advice, care and company made my stay at Orlando full of joy and always kept me active and energetic in my research during PhD. I thank him for just being a wonderful person in my life. With him, I would like to convey my sincere acknowledgment to my extended family. I owe my sincere gratitude to my grandma and maternal uncle for their love and encouragement, my brother Alok for his support and sharing the colorful days of my childhood and my in-laws for their blessings. I wish to thank my sister-in-law Kaveri, cousin brother Abhisek, sisters and their family for their endless love and support.

My time at University of Central Florida (UCF) was made enjoyable in large part due to many friends at my work place Nanoscience Technology Center (NSTC) and groups that became part of my life. It is my pleasure to convey my sincere acknowledgement to Satyender. He has been my friend, philosopher and guide in true sense for everything I persuaded during my graduate

studies. I am also grateful for the friendship and time spent with my friends Tanusri, Shruba, Surajit, Soumitra, Satarupa, Ranita, Sourangsu, Anirban, Sudip, Subhas, Jaya, Atryee, Keka, Indra and many other people. Our memorable trips to the mountains and the famous Florida beaches are unforgettable. My stay at Orlando was also enriched by the friends from ‘Bengali Society of Florida’. I acknowledge them for arranging social get-togethers which never made me feel away from home.

I appreciate the camaraderie and expertise of Kirk Scammon and Mikhail Klimov at AMPAC for helping me in operating instruments. I thank all of my colleagues and friends at NSTC and UCF.

At last but not the least, I gratefully acknowledge the financial support from NanoScience Technology Center and Department of Chemistry, University of Central Florida which enabled me to successfully complete my dissertation.

I certainly have overlooked the help and kindness of many others. Please forgive me for the unintentional oversight.

TABLE OF CONTENTS

LIST OF FIGURES	xiv
LIST OF TABLES	xix
ABBREVIATIONS	xx
CHAPTER 1 INTRODUCTION	1
1.1 Overview of Nanotechnology and Nanomaterials	1
1.1.1 Polymer based nanomaterials	3
1.1.1.1 Electrospun polymeric nanofibers	3
1.1.1.2 Conducting polymers	5
1.1.1.2.1 Poly(3-alkylthiophene) [PAT]	8
1.1.1.2.2 Regioregular P3HT – synthesis and structure – property relationship	9
1.1.2 Carbon based nanomaterials	13
1.1.2.1 Carbon nanotubes (CNTs)	14
1.1.2.2 Graphene	16
1.1.3 Hybrid nanostructured materials: multilayer films	17
1.2 Functionalization Nanomaterial Surface	19
1.2.1 Processing of carbon nanotubes	20
(1) Mechanical exfoliation	20
(2) Chemical surface modification	20
(3) Third component-assisted dispersion	21
1.2.2 Processing of graphene	22
(1) Intercalation of small molecules by mechanical exfoliation	23
(2) Oxidation of graphite	25
(3) Surface functionalization of graphite oxide	27
1.2.3 Stimuli responsive functionalized multilayer films	29
1.2.3.1 Temperature responsive multilayer film	31
1.2.3.2 pH responsive multilayer film	32
1.3 Outlook	33
1.3.1 Diverse applications of nanotechnology	33
1.3.2 Theme of the research	35
CHAPTER 2 CONFORMAL SWITCHABLE SUPERHYDROPHOBIC / HYDROPHILIC SURFACES FOR FLOW CONTROL IN MICROFLUIDIC CHANNEL	39
2.1 Abstract	39
2.2 Introduction	39
2.2.1 Overview on microfluidics	39
2.2.2 Microvalves	40
2.2.3 Smart surfaces used as microvalve	41

2.2.4	Working principle of hydrophobic valve.....	41
2.2.5	Role of thermoresponsive polymer in creating switchable surface	44
2.3	Results and Discussion.....	46
2.3.1	Fabrication of the microvalve.....	54
2.4	Experimental	57
2.4.1	Materials and chemicals.....	57
2.4.2	Fabrication of rough PAH/silica nanoparticle coatings.....	57
2.4.3	Initiator coupling.....	58
2.4.4	Poly(N-isopropylacrylamide) (PNIPAAm) grafting.....	58
2.4.5	Characterization.....	59
2.5	Conclusion.....	59

CHAPTER 3 FABRICATION OF ANTIREFLECTION COATINGS ON PLASTICS USING SPRAYING LAYER-BY-LAYER SELF ASSEMBLY TECHNIQUE

61

3.1	Abstract	61
3.2	Introduction	61
3.3	Results and Discussion.....	65
3.3.1	Modification of the PC substrate with APTS	65
3.3.2	Layer-by-layer deposition of PAH/silica nanoparticle AR coatings on APTS modified polycarbonate substrates	69
3.3.3	Sol-gel coating on APTS-modified PC substrate	71
3.3.4	Fabrication of abrasion resistant AR coatings	74
3.4	Experimental	77
3.4.1	Chemical and Materials	77
3.4.2	Polycarbonate surface functionalization with APTS	77
3.4.3	Sol-gel preparation.....	77
3.4.4	Spin coating of the sol-gel solution	77
3.4.5	Layer-by-layer (spraying) deposition	78
3.4.6	Layer-by-layer (dipping) deposition.....	79
3.4.7	Characterization.....	79
3.5	Conclusion.....	79

CHAPTER 4 FABRICATION OF ULTRATHIN POLYELECTROLYTE FIBERS AND THEIR CONTROLLED RELEASE PROPERTIES

80

4.1	Abstract	80
4.2	Introduction	80
4.3	Results and Discussion.....	82
4.3.1	Fiber fabrication.....	82
4.3.2	Loading methylene blue.....	84
4.3.3	Release of MB under nonbuffered conditions	85
4.3.4	Sustained MB release in a PBS solution.....	89

4.3.5	Temperature controlled MB release in a PBS solution.....	91
4.4	Experimental	93
4.4.1	Materials and chemicals.....	93
4.4.2	Fabrication of fibers.....	94
4.4.3	Loading methylene blue in fibers	94
4.4.4	Assembly of poly(acrylic acid)/poly(N-isopropylacrylamide) (PAA/PNIPAAm) multilayers on PAA/PAH fibers.....	95
4.4.5	Measurement method.....	95
4.5	Conclusion.....	96

CHAPTER 5 EFFECT OF SURFACTANT ON SUSTAINED RELEASE OF DRUG FROM SUPERHYDROPHOBIC NANOFIBER 97

5.1	Abstract	97
5.2	Introduction	97
5.3	Results and Discussion:.....	100
5.3.1	Under water superhydrophobicity	103
5.3.2	Effect of the surfactant structure on wetting phenomena	106
5.3.3	The time dependent wetting and the retention time.....	108
5.4	Experimental:	109
5.4.1	Fabrication of drug loaded superhydrophobic fiber	109
5.4.2	Measurement.....	109
5.5	Conclusion.....	110

CHAPTER 6 POLY(3-HEXYLTHIOPHENE) SUPRAMOLECULAR STRUCTURE ON REDUCED GRAPHENE OXIDE NANOSHEETS 111

6.1	Abstract	111
6.2	Introduction	111
6.3	Results and Discussion.....	113
6.4	Experimental	120
6.4.1	Materials	120
6.4.2	GO Dispersion	120
6.4.3	Characterization	120
6.4.4	X-ray photoelectron spectroscopy (XPS) characterization of GO and RGO	121
6.4.5	P3HT Synthesis and In-Situ UV-Vis Spectroscopic Studies of RGO induced P3HT crystallization Process	122
6.4.6	Dispersing RGO Using P3HT and Fabricating P3HT Supramolecular Structures on RGO Nanosheets	125
6.5	Conclusion.....	125

CHAPTER 7 GRAPHENE-COPPER PHTHALOCYANINE COMPOSITE THIN FILM WITH OPTOELECTRONIC PROPERTIES 126

7.1	Abstract	126
7.2	Introduction	126
7.3	Results and Discussion.....	128
7.3.1	Characterization of the composite ink	128
7.3.2	Measurement of the optoelectronic property	134
7.4	Experimental Method.....	138
7.4.1	Synthesis and characterization of graphene/TSCuPc composite ink.....	138
7.4.2	Device fabrication.....	139
7.4.3	Measurement of optoelectronic properties	139
7.5	Conclusion.....	139
	SUMMARY AND OUTLOOK.....	141
	REFERENCES	147
	LIST OF RELEVANT PUBLICATIONS	168

LIST OF FIGURES

Figure 1.1	Schematic diagram of electrospinning setup. (Reprinted from [1] with permission from Elsevier)	4
Figure 1.2	Structures of different conducting polymers.....	8
Figure 1.3	(A) Diad and triad structures of P3HT (B) Synthesis scheme of P3HT in GRIM method.....	13
Figure 1.4	(a) Graphite (b) Diamond (c) Carbon Nanotubes. (Reprinted from [1] with permission from Elsevier).....	14
Figure 1.5	Isocyanate treatment of GO where organic isocyanate reacts with the hydroxyl and carboxyl groups of the graphene oxide sheets. ¹⁰⁶ (Reprinted from [106] with permission from Elsevier).....	28
Figure 1.6	Lahann ¹²⁰ shows that it is possible to change the surface from hydrophilic to hydrophobic and reverses by applying a voltage between a gold electrode coated with a SAM layer and a reference electrode in water. (Reprinted from [120] with permission from The American Association for the Advancement of Science)	30
Figure 1.7	Changing of the surface from hydrophobic to hydrophilic and reverses by immersing the samples with toluene or water. ¹²¹ (Reprinted from [121] with permission from American Chemical Society)	30
Figure 1.8	Diverse applications of nanotechnology.....	34
Figure 2.1	Young's model showing water droplet on smooth surface.....	43
Figure 2.2	Wenzel model showing water droplet on rough surface.....	43
Figure 2.3	Cassie Baxter model showing water droplet sitting on the trapped air in roughness grooves.....	43
Figure 2.4	Thermosensitive wettability of a PNIPAAm modified smooth surface (a) Change in advancing contact angle of a water droplet when the temperature was increased from 25 °C to 40 °C i.e. above LCST of PNIPAAm (b) Formation of intermolecular hydrogen bonding of PNIPAAm and water molecules and intramolecular hydrogen bonding within PNIPAAm chain. ¹¹⁷ (Reprinted from [117] with permission from Wiley-VCH Verlag GmbH & Co. KGaA.).....	45
Figure 2.5	Schematic of the synthesis route of grafting PNIPAAm from a surface of PAA. ..	47
Figure 2.6	AFM height images of (A) annealed PAH/SiO ₂ multilayer film with dual-length scale structures (B) A very thin layer of PNIPAAm deposited on rough multilayer film (sample 1). (C) A thick layer of PNIPAAm deposition after 2 hours polymerization which reduces roughness (sample 2) (D) Nanoscale roughness is	

reintroduced with silica nanoparticle deposition on the thick PNIPAAm polymer film (sample 3) The size of all images (A-D) are 1 μ m and the numbers at left corner on each image indicates surface roughness (rms) (E) Schematic illustration of the structure of Sample 2 (F) Schematic illustration of the structure of sample 3. 50

Figure 2.7	XPS analysis of the (A) surface composition of an annealed silica nanoparticle film, (B) a rough silica film covered with a thin layer of PNIPAAm (sample 1), (C) a rough silica film covered with a thick layer of PNIPAAm (sample 2), and (D) a rough PNIPAAm functionalized silica film covered with a layer of silica nanoparticles (sample 3).	50
Figure 2.8	The change of water contact angle Vs temperature on a hydrophobic/hydrophilic switchable surface.	53
Figure 2.9	The change of water contact angle Vs temperature on a superhydrophobic/hydrophilic switchable surface.	53
Figure 2.10	Schematic of fabrication of switchable valve in microchannel.	55
Figure 2.11	Testing of valve at 70 °C A. Dyed water approaches the junction B. Dyed water stops on the patch.	56
Figure 2.12	Testing of valve at 25 °C A. Dyed water approaches the junction B. Dyed water flows on the patch as it switched to hydrophilic.	56
Figure 3.1	(A) Fresnel reflection coefficient at an interface of two media with no AR coating (B) Refractive index of the Rayleigh's film (AR coating) in between air and glass for multiple reflections.	63
Figure 3.2	Schematic of Functionalization of PC with 3-APTS.	66
Figure 3.3	(a) Bare PC sample showing contact angle of 90° and (b) an APTS-modified PC sample showing contact angle of 40°.	67
Figure 3.4	XPS spectra of (a) a bare PC substrate, (b) an APTS-modified PC substrate, and (c) an APTS-modified glass sample.	68
Figure 3.5	Binding energies of the N 1S electrons in (a) urethane linkage of APTS-modified PC surface and (b) free amine of APTS-modified glass surface as obtained from high-resolution XPS analysis.	69
Figure 3.6	The film thickness and refractive-index changes with a number of bilayers deposited (symbolizes film thickness and symbolizes refractive index).	69
Figure 3.7	UV-visible transmittance spectra of the AR-coated PC substrate with a different number of bilayers as compared to a bare PC substrate.	71

Figure 3.8	UV–Visible transmittance spectra of (a) a sol-gel-modified PC substrate and (b) a bare PC substrate.....	71
Figure 3.9	UV–visible transmittance spectra of (a) 14 bi-layers of AR coating on one side of a sol-gel-modified PC substrate by dip-coating, (b) 10 bi-layers of AR coating on one side of a sol-gel modified PC substrate by spraying deposition, and (c) 24 bi-layers of AR coating on one side of the APTS-modified PC substrate by spray deposition.	74
Figure 3.10	AFM images of (a) 14 bi-layers of AR coating on one side of sol-gel-modified PC substrate by dip-coating and (b) 10 bi-layers of AR coating on one side of the sol-gel-modified PC substrate by spray coating. The scale of the images is 5 μm	74
Figure 3.11	UV–Visible transmittance spectra of (a) an AR coating on a PC substrate with the sol-gel treatment and (b) an AR coating on a PC substrate without the sol-gel treatment.	76
Figure 3.12	Photograph of PC substrates (A) with and (B) without AR coatings.	76
Figure 4.1	SEM image of PAA/PAH fibers electrospun from a 2:1 PAA/PAH (molar ratio) mixture.	83
Figure 4.2	FTIR spectra of uncrosslinked (A), the crosslinked (B) and NaOH treated crosslinked PAA/PAH fibers (C). The absorption peaks at 1700 cm^{-1} , 1691 cm^{-1} , and 1542 cm^{-1} are assigned to the C O stretching of carboxylic acid (COOH) group, the amide (CONH) group and the ionized carboxylate (COO ⁻) group, respectively.	85
Figure 4.3	Release of MB from crosslinked PAA/PAH fibers in water (pH~5.5).	88
Figure 4.4	Release profile of MB in aqueous solutions with different pH (The release is controlled by changing the solution pH).....	88
Figure 4.5	Release profile of MB in nonbuffered aqueous solutions of different pH (A); (B) the releasing profile of MB in first 40 min.	89
Figure 4.6	Release profile of MB from bare PAA/PAH fibers (A) and perfluorosilane coated PAA/PAH fibers (B) in PBS at pH 7.4. The release time of B is 100 times longer than that of A.	91
Figure 4.7	The releasing profile of MB from fibers coated with 11, 21 and 31 layers of PAA/PNIPAAm multilayers at room temperature ~25 $^{\circ}\text{C}$ (A) and 40 $^{\circ}\text{C}$ (B) in PBS.	93
Figure 4.8	Structures of the chemicals used in the study.	95
Figure 5.1	SEM image of the silica nanoparticle loaded superhydrophobic fiber. Inset is the contact angle of water droplet on the superhydrophobic fiber.	101

Figure 5.2	(A) Release profile of MB from normal crosslinked fiber in PBS buffer (B) release profile of neutral drug from superhydrophobic fiber and normal crosslinked fiber in PBS buffer solution.....	102
Figure 5.3	Release of neutral drug from superhydrophobic fiber in aqueous solution of SDS with different concentrations and the retention time of the drug in the fiber when immersed in different surfactant solutions (below).	103
Figure 5.4	Structure of SDS.	107
Figure 5.5	Change in contact angle with concentration of SDS. The red point indicates $C_s > 2CMC$	107
Figure 6.1	(Left) An AFM height image of monolayers of RGO/P3HT composites on a mica substrate (image size 15 μm). The inset is a higher resolution image (image size = 1 μm) of a RGO/P3HT monolayer with height analysis showing a thickness of about 1.2 nm. (Right) Reduced graphene oxide (RGO) suspension in anisole without P3HT (A) and with P3HT (B).....	114
Figure 6.2	TEM images of A) RGO/P3HT composites showing RGO with short P3HT nanowires and B) P3HT supramolecular structures on RGO formed in solution. The inset is the SAED pattern of the P3HT nanowires. The width of the nanowires is about 14 nm.....	115
Figure 6.3	AFM images of A) P3HT nanowires on RGO monolayers formed in solution on a mica substrate by drop casting (image size = 2 μm) and B) P3HT nanowires formed on surfactant free RGO monolayers on a mica substrate by drop casting followed by removal of the solution by spinning (image size = 5 μm).	116
Figure 6.4	Raman spectra of GO (A), RGO (B), P3HT nanowires (C), and RGO with P3HT nanowires (D).....	119
Figure 6.5	XPS Spectrum of (A) GO and (B) RGO.....	122
Figure 6.6	A. P3HT nanowires in anisole; B. P3HT with graphene oxide (GO); C. P3HT with reduced graphene oxide (RGO); D. P3HT nanowires in anisole B. D. UV-Vis absorbance change at 600 nm of the pure P3HT (triangles), P3HT with GO (squares), and P3HT with RGO (diamonds) suspension during the crystallization process.....	124
Figure 7.1	Tapping mode AFM image of the RGO-TSCuPc composite on mica. Inset shows (A) Reductuin of GO in presence of TSCuPc to form RGO-TSCuPc composite ink (B) Precipitate formed when GO reduced without TSCuPc.....	129
Figure 7.2	UV-Vis absorption spectra of RGO, TSCuPc and the composite film.....	130
Figure 7.3	C1s XPS peak of RGO-TSCuPc composite.....	132

Figure 7.4	XPS spectra of TSCuPc (upper row) and the composite (bottom row).....	132
Figure 7.5	Raman spectra of (A) RGO (B) TSCuPc film and (C) RGO –TSCuPc composite film.....	134
Figure 7.6	(a) Schematic diagram of the device and electron transport measurement setup. (b) Current-voltage characteristics of the RGO-TSCuPc (1:2.5) device (before annealing and after annealing), (c) Current-voltage characteristics of the annealed RGO-TSCuPc (1:2.5) device under dark and light illumination. The inset shows Current-voltage characteristics of the annealed RGO-only device under dark and light illumination. (d) Energy level diagram of TSCuPc and RGO.....	137

LIST OF TABLES

Table 1.1	Conducting polymers and their band gap energies. (Reproduced from [1] with permission from Elsevier).....	6
Table 1.2	Structure-property relationship of P3HT polymer. ²⁴	10
Table 1.3	The influence of ultrasonic solvent and ultrasonic power on the volume of expanded graphite. ⁸⁹ (Reproduced from [89] with permission from Elsevier).....	24
Table 7.1	Dark conductivity, Photoconductivity, photoresponsivity and photosensitivity for RGO/TSCuPc composite films (average film thickness was 120 nm and optical properties was measured under 100 mW/cm ² intensity of light).....	137

ABBREVIATIONS

ABMP	: 2, 2'- azobis (2-methylpropionamide) dichloride
AFM	: Atomic force microscopy
APTS	: 3-Amino (propyltrimethoxysilane)
AR	: Antireflection
CMC	: Critical micelle concentration
CNT	: Carbon nanotube
CVD	: Chemical vapor deposition
DI	: Deionized water
DMF	: Dimethylformamide
EDC	: N-(3- dimethylaminopropyl)-N-ethylcarbodiimide
FET	: Field effect transistor
GO	: Graphene oxide
GRIM	: Grignard metathesis
HH	: Head to head
HT	: Head to tail
LBL	: Layer-by-layer
LCST	: Lower critical solution temperature
MB	: Methylene blue
M_n	: Number average molecular weight
$Ni(dppp)Cl_2$:Nickel [propane-1,3-diylbis(diphenylphosphane)]chloride
P3HT	: Poly(3-hexylthiophene)
PAA	: Poly(acrylic acid)
PAH	: Poly(allylaminehydrochloride)
PAT	: Poly(3-alkylthiophene)

PBS	: Phosphate buffered saline
PC	: Polycarbonate
PDMS	: Polymethylsiloxane
Perfluorosilane:	Trichloro (1H, 1H, 2H, 2H-perfluorooctyl) silane
PNIPAAm	: Poly(N-isopropylacrylamide)
RGO	: Reduced graphene oxide
RR	: Regioregular
SAMs	: Self assembled monolayers
SDS	: Sodium dodecyl sulphate
SEM	: Scanning electron microscopy
TEM	: Transmission electron microscopy
TEOS	: Tetraethylorthosilicate
THF	: Tetrahydrofuran
TPC	: Three phase contact line
TSCuPc	: Sodium tetrasulphonate salt of copper phthalocyanine
UV-Vis	: Ultraviolet –Visible spectrophotometer
XPS	: X-ray photoelectron spectroscopy

CHAPTER 1 INTRODUCTION

1.1 Overview of Nanotechnology and Nanomaterials

Ever since the introduction of the concept of ‘Nanotechnology’ by physicist Richard Feynman in his talk titled ‘There’s Plenty of Room at the Bottom’ at an American Physical Society meeting in 1959, an exceptionally increasing demand was placed to build effective strategies to manipulate material’s properties at the nanoscale. Precisely, nanotechnology involved the processing of materials in their single atom or molecular level with size in multiples of nanometer (nm). The concept was generalized when nanotechnology implicated materials and devices within the size range of 100 nm or smaller in at least one dimension. Materials when reduced to size in few nanometers, surprisingly exhibited very different mechanical and electronic properties compared to what they showed in macroscale. The reason was attributed to the fact that the materials at nanoscale had increased ratio of volume to surface area owing to their very small size. The small size gave rise to a very significant ‘quantum size effect’ where electronic property of a solid altered appreciably due to its extensive size reduction (specially with semiconductors). The small feature size of nanomaterials also made them active at their surface and interfaces as compared to their bulk components. Bulk materials had very few atoms at or near the surface or interface whereas more than half of the atoms would be at the interface and surface for the nanomaterials enabling them to show unique surface properties due to different energy level, reactivity and electronic structure. However, the technological significance of the nanoscale phenomena in materials was realized more with the discovery of fullerenes in 1985 and carbon nanotubes in 1991, followed by the invention of inorganic fullerenes and anisotropic nanostructures which were major breakthroughs in the field of nanoscience and technology. Both fullerene and CNT were allotropes of carbon with the

dimension in nanoscale and had novel properties, which made them potentially useful in many applications in nanotechnology, electronics, optics and other fields of materials science. This revolutionary move in nanoscience put enormous expectation on the research of nanomaterials and its applications.¹ The research was based on two fundamental nanofabrication approaches. The ‘bottom up approach’ encompassed the concept of ‘molecular self assembly’ and ‘molecular recognition’ to build up useful conformations depending on their chemical properties. In ‘top down approach’, microfabrication techniques were used to cut, mill, and shape large entities into the desired nano objects. Nevertheless, functionally important nanomaterials and devices would emerge from the combination of these two complimentary nanofabrication approaches.

Classification of nanomaterials

Current nanomaterials can be classified in four different categories depending on their organic and inorganic sources.

1. Polymer based nanomaterials – Polymeric nanofibers, nanorods, nanoparticles, nanowires and dendrimers
2. Carbon based nanomaterials – Fullerenes, nanotubes, graphene
3. Metal based nanomaterials – Quantum dots, silver & gold nanoparticles, metal oxides
4. Nanocomposites – Multiphase material with dimension in nanoscale with nanostructured materials dispersed in bulk matrix such as colloids, gels, copolymers. This also includes hybrid systems like multilayer thin film which may contain polymers, metals, carbon nanostructures, nanoparticles etc. in their structure.

In the following sections, I will review some aspects of polymer and carbon based materials followed by an overview of functional multilayer thin films under the section hybrid nanostructures.

1.1.1 Polymer based nanomaterials

Research of one-dimensional polymeric nanomaterials made significant progress in the past decade and the technology had been explored for a wide range of applications. A number of synthetically novel approaches were successfully developed to prepare nanostructured polymers with desired properties and precise aspect ratio. Such routes involved electrospinning,² co-electrospinning,³ membrane based techniques,⁴ building tubes by fiber templates (TUFT),⁵ electrochemical polymerization⁶ within templates, chemical and self-assembly routes,^{7, 8} to name a few. Most of the recent efforts were focused on polymeric nanotubes, nanowires, nanofibers and nanorods. In the following section, general electrostatic scheme and the advancements made in the field of electrospun polymeric nanofibers will be discussed in brief followed by a short overview of conducting polymers which drew much attention in fabricating polymeric nanostructure based devices.

1.1.1.1 Electrospun polymeric nanofibers

The technique ‘electrospinning’ was one of the rapidly growing scientific approaches in creating novel nanomaterials with advanced applications. The practice attracted much attention as a wide variety of polymeric solutions could be spun using the technique, to form fibers consistently in submicron range as compared to the conventional fiber drawing techniques. In this process a polymer solution or melt was fed in a syringe fitted with a small diameter needle acting as an anode. When high voltage was applied to the tip of the needle, the liquid polymer was drawn like a jet and was collected onto a target cathode in the form of solid fibrous mat. The origin of this technique could be tracked back to 1934 with the first patent applied by Formhals for his invention related to the experimental setup for producing cellulose acetate based artificial filaments using electric charges.⁹ In later years, the field was populated with a number of

scientific groups across the world and the process was reviewed and modified continuously to spin fibers from a variety of polymers with rapid progress. In 1952, Vonnegut and Neubauer invented an electrical atomization to form highly charged droplets with uniform diameter in the range of 0.1 mm.¹⁰ In 1966, Simons successfully fabricated ultra thin, lightweight non-woven fibers by electrical spinning.¹¹ It was in 1969, the term “Taylor Cone” was associated with the technique of electrospinning in technological aspect after the name of scientist Sir Geoffrey Ingram Taylor. It referred to the shape of the polymer droplet formed at the tip of the needle when an electric field was applied. The shape of the droplet was conical termed as ‘Taylor Cone’. The liquid jet was ejected from the vertices of that cone, once the electrostatic force in that cone overcame the solution’s surface tension.

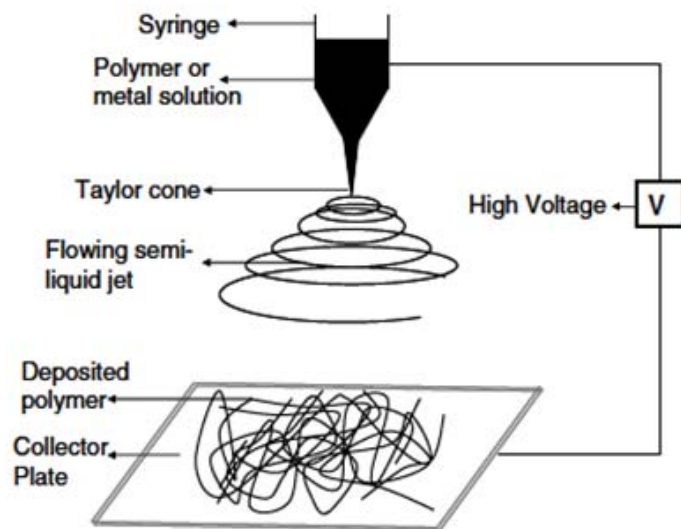


Figure 1.1 Schematic diagram of electrospinning setup. (Reprinted from [1] with permission from Elsevier)

However, in late 80s, the elegance of the electrospinning technique was more realized with respect to its versatility to spin wide range of polymeric fibers just by controlling few physical and chemical parameters.¹²⁻¹⁴ The fibers had diameter less than 100nm and were named as nanofibers. A solution of polyaniline was electrospun by MacDiarmid et al. to form fibers with

diameter below 30 nm.¹⁵ The nanofibers appeared with unique characteristics such as large surface to volume/mass ratio (approximately 100 m²/g for a fiber diameter of 100 nm¹⁴), high stiffness, tensile strength and flexibility of surface modification as compared to the other form of the material ever known. So far a wide variety of synthetic and natural polymers have been used to spin fibers using electrospinning. And a detailed analysis has been carried out on the influence of processing parameters on, fiber diameter, morphology and properties. Nanofibers contributed significantly in various fields like nanocatalysis, protective clothing, filtration, tissue scaffolds, drug delivery and optical electronics. Amongst the most interesting application was in tissue engineering for controlled drug release and tissue remodeling, because polymeric nanofibers had resemblance to natural extracellular matrix with respect to structure and function. Consequently the natural polymers like chitosan, collagen etc were favored over the synthetic polymers for the particular application due to their tissue compatibility and resorbable biodegradation products.

1.1.1.2 Conducting polymers

Out of the several aspects of polymeric nanostructured materials, research on conducting polymers was revolutionary. After the electronic/semiconductor industry reached their limitation with the conventional semiconductors, the immediate requirement for a novel nanomaterial beyond the scope of usual metal/metal oxide semiconductor was realized. At this time, conducting polymers emerged as a viable alternative to inorganic semiconductors, whose property and the working condition could be manipulated in the miniature electronic devices i.e. at nanolevel. Polymers were generally insulators/ semiconductors with very poor conductivity as evident from the lists of band gap energies of some polymers given in Table 1.1.

Table 1.1 Conducting polymers and their band gap energies. (Reproduced from [1] with permission from Elsevier)

Polymer	Band Gap (eV)
Polyacetylene	1.5-1.7 ¹⁶
Polypyrrole	3.2 ¹⁷
Polythiophene	2.0 ¹⁷
Polyaniline	3.6 ¹⁸

The poor conductivity stemmed from the fact that most of the polymers like polyethylene, polypropylene had their valence electrons bound in the sp^3 hybridized covalent bond. These σ bonded electrons were less labile and hence could not contribute to conductivity. However, polymers like polyaniline and polythiophene had their backbones made up of contiguous sp^2 hybridized carbon centers, where the valence electrons remained in delocalized p_z orbitals. Owing to the high mobility of these loosely bound electrons, the conductivity of the polymers could be increased by appropriate doping with oxidizing or reducing agents. Such polymers with conjugated π system had small ionization potential. So, an electron could be easily added (reduction) or removed (oxidation) from the outer orbital of the polymeric ion to obtain resonance state without disrupting the sigma (σ) bonds in the the polymer backbone. On doping, the insulating polymer was converted to charged ionic complex with polymeric cation/anion and its counterpart and resulted in electrical conductivity of several orders of magnitude. Different conducting polymers, when doped subsequently, were found to produce saturation of the conductivity at values around 0.1-10 kS/cm. The highest conductivity value reported so far for the conductivity of stretch oriented polyacetylene was around 80 kS/cm.^{16, 19-21} However, the mechanism of conduction in organic polymers is different from that of inorganic

semiconductors. Electrical conductivity in conjugated polymers depends on the defect states along the polymer chain. These defect states originate from the electronic excitations accompanied by a disorder or relaxation of the polymeric lattice. These states exist between the conduction and valence band, and are assumed to be the operating center for the polymer conductivity. Well studied classes of organic conducting polymers includes polyacetylenes, polypyrroles, polythiophenes, polyanilines, polythiophenes, poly(p-phenylene sulfide), and poly(p-phenylene vinylene)s (PPV), etc. They promise their application in different fields based on either their conductivity or electroactive properties. Electrostatic materials, conductive adhesive, antistatic clothings, piezoceramics, aircraft structures use conductivity of the polymers as the main property whereas, molecular electronics, electrical displays, drug release systems, optical computers utilize their electroactivity. Among all the conducting polymers named before, polythiophene and its derivatives emerged as an important class of conjugated polymers which formed some of the most thermally and environmentally stable materials for next generation of optical and electronic devices. I would confine my discussion in poly(3-alkylthiophene), a soluble and processable derivative of conducting polythiophene.

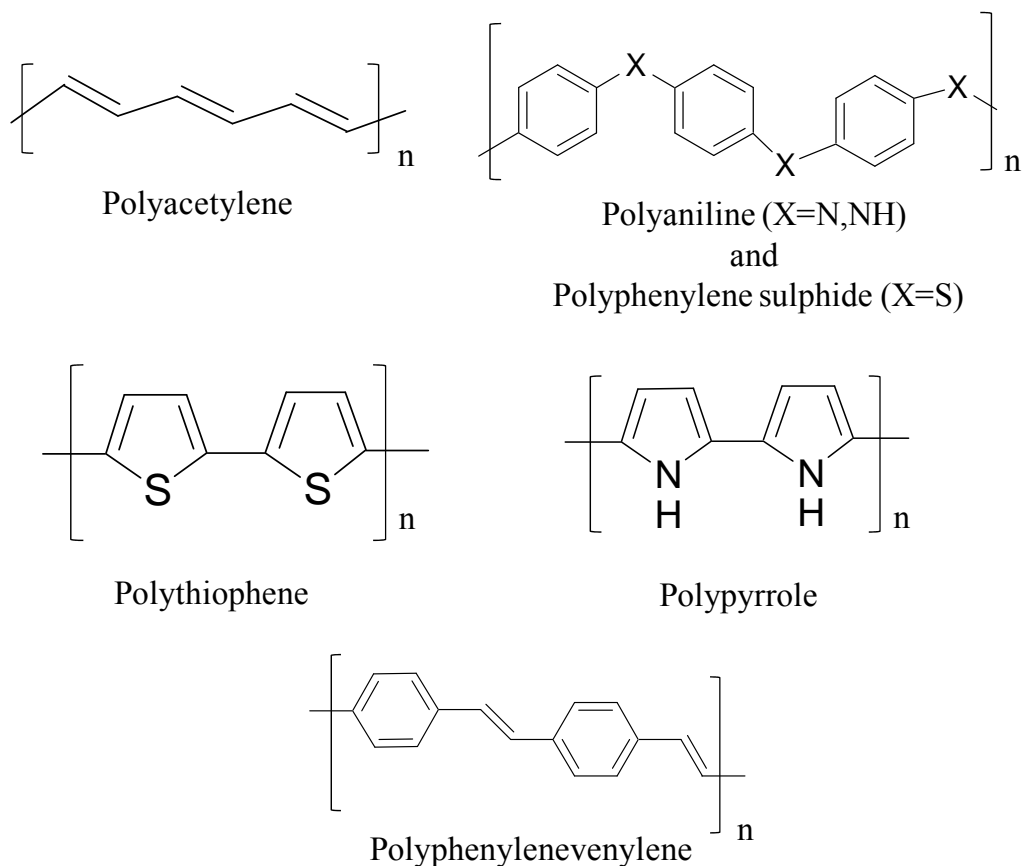


Figure 1.2 Structures of different conducting polymers.

1.1.1.2.1 Poly(3-alkylthiophene) [PAT]

Thiophene could form a variety of conjugated polymers when coupled appropriately. The highest mobility measured in solution-processed all-polymer ‘Field Effect Transistor’ (FET) device had been exhibited by thiophene polymers. Despite of exceptionally high thermal stability and electric conductivity of the polythiophene films, they had limited application in diverse fields due to poor processability. Most of the unsubstituted conjugated polymers had rod like morphology due to extended π delocalization and hence poor solubility. However, introducing substituent to the polymer backbone could enhance their solubility. The functionalized thiophene derivatives had crystalline structure and possessed excellent charge transport properties, too. Therefore, poly(3-alkylthiophene) [PAT] was synthesized in pursuit for a soluble and


processable conducting polythiophene. At first, 3-methylthiophene was polymerized but found to be insoluble. Later, the polymer with alkyl chain longer than butyl was found to be environmentally stable and soluble. Subsequently, it could readily form long-standing and continuous film exhibiting conductivity as high as 1-5 S/cm upon oxidation. So far, poly(3-hexylthiophene) (P3HT) is the most widely studied semiconducting polymer for charge transport applications.

1.1.1.2.2 Regioregular P3HT – synthesis and structure – property relationship

The three most popular routes to synthesize PAT were FeCl₃ method, the Grignard coupling method using Ni(dppp)Cl₂, and the electrochemical method.^{22, 23} Large quantity of PAT could be prepared using either of the methods with high molecular weight. However, ¹H NMR analysis of the product polymer revealed a common factor that the monomers were coupled only at the 2, 5 positions with random regiospecificity and there were almost no 2, 4(β) linkage, presumably due to the steric hindrance caused by the alkyl chain at the third position of the thiophene ring. The random regiospecificity of the product polymer was due to the asymmetric nature of 3-alkylthiophene monomers which could lead to three possible chemically distinct dyad structures and four spectroscopically different triad structures when coupled at 2, 5 positions. The so-called regio-irregular polymers contained three types of coupling [head to head (HH), head to tail (HT) and tail to tail (TT)] products whereas the regioregular (RR) polymers were consisted of only head to tail (HT) coupling product. Among all the possible regioisomers of PAT, the HT coupled dimers had *trans* coplanar orientation leading to lower energy conformation and hence showed better conjugation as compared to others. The difference in conformational energy between the HT and HH coupled isomers led to dramatic variation in electron mobility and conductivity

between regioregular and regiorandom PATs, the former having electrical conductivity two orders of magnitude higher than the later reported by McCullough et al.

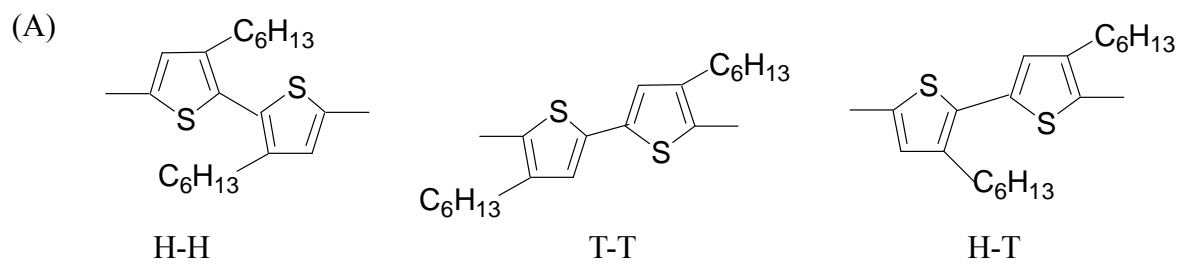
Table 1.2 Structure-property relationship of P3HT polymer.²⁴

	Polymer	Molecular Weight (M_n)	Uv-Vis spectroscopy (λ_{max}) (nm)			Conductivity σ (S/sec)
			Solution	Film	$\Delta\lambda_{max}^f$	
% head to tail combination (regioregularity) increases 	P1	4200	413	424	11	0.0089
	P2	5700	419	430	11	0.0074
	P3	2600	420	444	24	0.13
	P4	5600	425	462	37	0.14
	P5	12900	434	488	52	0.55
	P6	40600	440	505	65	6.00

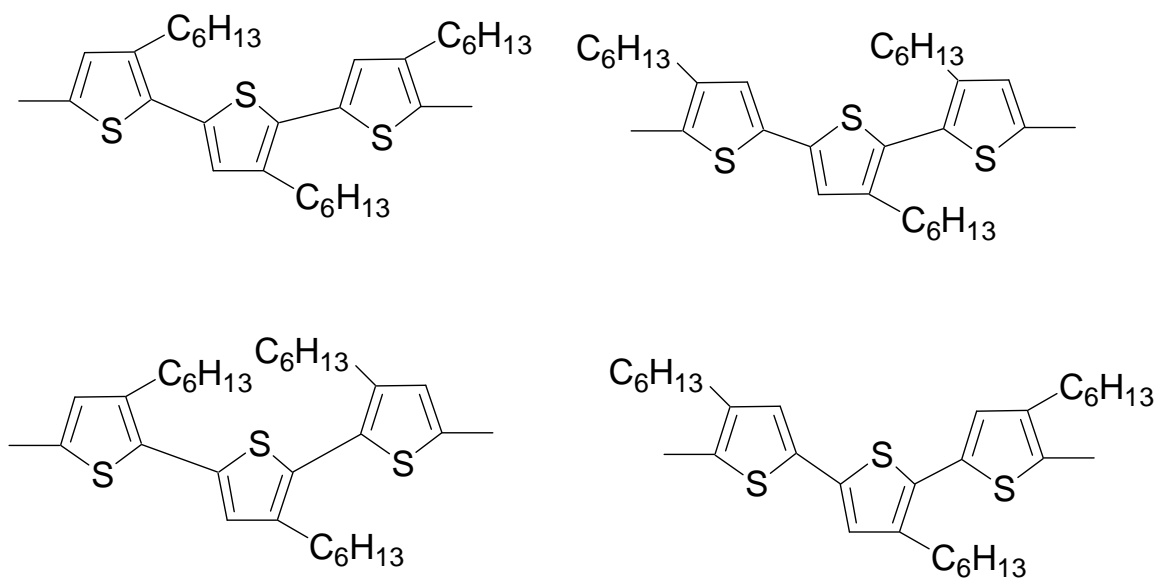
Synthesis: Several synthetic procedures were approached to prepare regioregular poly(3-hexylthiophene) [P3HT] using metal catalyzed cross coupling polymerization.²² The first synthesis of regioregular head-to-tail coupled poly(3-alkylthiophenes) (PATs) was reported by McCullough and Lowe²⁵ early in 1992, in which Grignard derivatives of 3-alkyl-2,5 dibromothiophene were coupled with nickel(II) catalyst to give high molecular weight regioregular PAT in good yield. In this method, highly RR polymers were produced with molecular weights (M_n) of 20 –40 K and with HT couplings over 98%. The second synthetic approach was reported by Rieke, which involved the reaction of 3-alkyl-2, 5 dibromothiophene with activated “Rieke” zinc at low temperature, followed by nickel(0) catalyzed polycondensation reaction. This route offered the advantage of high-functional group tolerance. In my research, P3HT was synthesized by Grignard Metathesis Reaction or GRIM method.^{26, 27} In this method, a solution of 2, 5-dibromo-3-alkylthiophene was allowed to react with one equivalent of an alkyl Grignard reagent. An alkylbromide and a mixture of 2-bromo-5-

magnesiobromo-3-alkylthiophene and 5-bromo-2-magnesiobromo-3-alkylthiophene (approximately in 85:15 ratio) were formed as a result of the metathesis reaction. Addition of Ni(dppp)Cl₂ catalyst to this reaction mixture initiated polymerization with the formation of highly RR polymers, in good molecular weight, low polydispersities, and high yield.

Structure-property: The alkyl side chains of P3HT, when regioregularly arranged in a head-to-tail configuration could give rise to enhanced charge carrier mobility.²⁸ This important observation provoked widespread interest in P3HT based research and RR-P3HT emerged as a benchmark-semiconducting polymer due to the advantages like easy availability, low cost, ease of solution-processing, and its promising electrical properties. The polymer molecular weight (M_n), polydispersity index and the regioregularity was found to be the key factors in determining polymer's crystallinity and orientation of the π conjugated thiophene backbone ring planes as they self assemble in a non-solvent or on a substrate from the solution. The supramolecular ordering in regioregular HT- PATs due to self-assembly was one of the most fascinating physical properties of P3HT, which led to large increase in electrical conductivity. Consequently by controlling the P3HT crystallization and its crystal dimension, it was possible to fabricate P3HT based device with high charge mobility. Recently, Liu et al.²⁹ reported a systematic study of P3HT crystallization by changing the polymer molecular weight (M_n), crystallization temperature, and polymer concentration in solution. The report explicitly demonstrated that P3HT could form different crystalline structures such as one-dimensional nanowhiskers based on crystallization temperature and polymer molecular weight, whereas, two-dimensional nanoribbons depending on polymer concentration. The synthesized nanoribbons showed more charge mobility ($0.012 \text{ cm}^2/(\text{V s})$) with an on/off ratio of 6.5×10^{-4}) than that of solution cast P3HT film.



Three structural diads of P3HT



Four spectroscopically distinct triad of P3HT

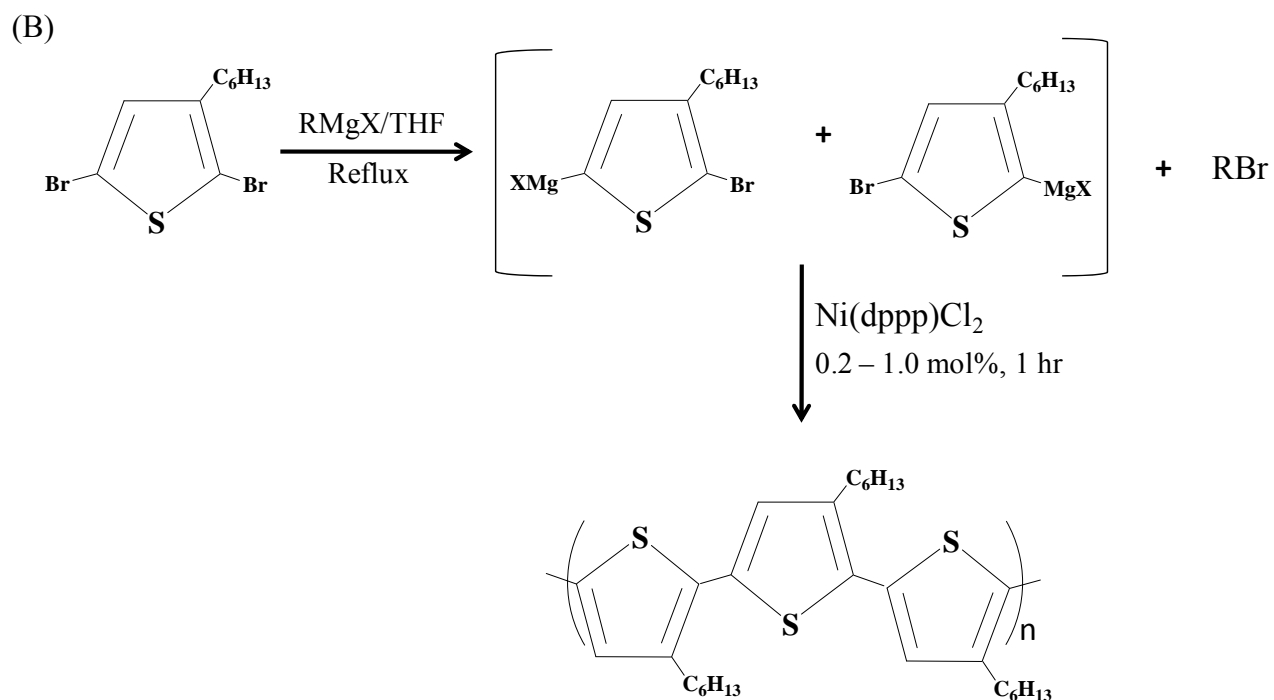


Figure 1.3 (A) Diad and triad structures of P3HT (B) Synthesis scheme of P3HT in GRIM method.

1.1.2 Carbon based nanomaterials

Only two broadly classified solid phase of carbon were known until the last decade: diamond and graphite. Diamond was the hardest material ever known with carbon in its sp^3 hybridization and graphite, a highly conducting soft material with carbon in sp^2 hybridization. Thus carbon could form various structures with different properties by rehybridization among sp^2 , and sp^3 . After discovery of fullerene and its derivatives, a number of different carbon nanostructured materials were found which resembled sp^2 hybridization based architecture like graphite. Carbon onions, carbon nanohorns (CNHs), carbon nanorods and CNTs are few of them. The discussion will be confined only to CNTs and graphenes pertaining to their relevance to my research.

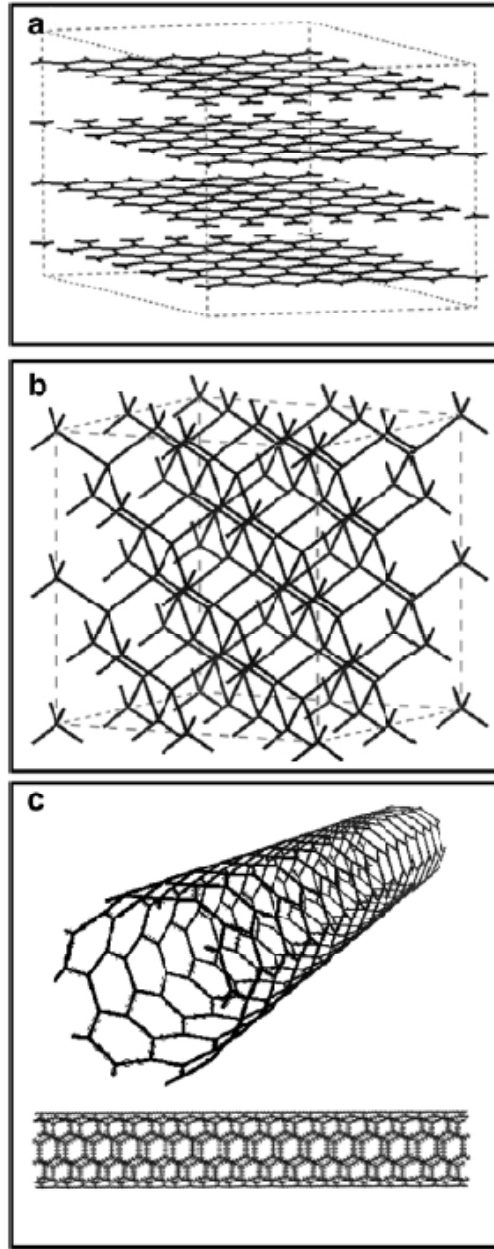


Figure 1.4 (a) Graphite (b) Diamond (c) Carbon Nanotubes. (Reprinted from [1] with permission from Elsevier)

1.1.2.1 Carbon nanotubes (CNTs)

Carbon nanotubes (CNTs) are cylindrical tubes derived from a honeycomb lattice representing an atomic layer of crystalline graphite, called graphene sheets. They can be single layered (known as SWCNT) or concentric tubes rolled over one another called multi-wall tubes

(MWCNT). The majority of bonding observed in these tubes is sp^2 , although it is mixed with an extent of sp^3 character because of its high curvature. The cap-end structure is formed with the combinations of 12 pentagonal (five) and 20 hexagonal (six membered) carbon rings. Both the forms have their unique properties leading to their applications from nanoelectronics, to sensors, energy conversion and storage devices (photovoltaics, batteries, fuel cells and supercapacitors), thermal management, and conductive nanocomposite. From the structural aspect, the circular curvature of CNT causes quantum confinement and σ - π rehybridization where, the three σ bonds are projected slightly out of plane³⁰ and the π orbital becomes more delocalized outside the tube. Consequently, the contribution of the p -character in the hybridization is high in CNTs than that of the graphite. Due to this π characteristic, nanotubes exhibits better electrical and thermal conductivity, mechanical strength and chemical and biological properties than graphite, but their processability becomes difficult as the tubes tend to agglomerate due to the strong van der Waals interaction among them. So, it is important to debundle and disperse CNTs homogeneously in the suitable solvents and/or polymer matrixes before they can be utilized effectively in polymer composites or single nanotube devices with complete realization of their unique properties. In order to achieve a good reproducibility in CNT based material fabrication and device function, the surface of the CNTs should be functionalized with target functional groups to improve their compatibility with various chemical agents or they can be mechanically stirred in suitable solvents to form dispersed CNT solution. However, achieving stable CNT dispersions in different solvent media and to functionalize the CNTs surfaces have always remained challenging due to the CNT's cylindrical structure and inert surface.

1.1.2.2 Graphene

Graphene is the basic building block of some of the carbon allotropes like carbon nanotubes, graphite and fullerene. It is a flat monolayer of sp^2 bonded carbon atoms tightly packed into a honeycomb lattice with C-C bond length of approximately 0.142 nm. It can be rolled into 0D bucy balls³¹ and 1D nanotubes or stacked into 3D graphite (Figure 1.4). From the view point of the atomic structure of single layer graphite or graphene, it is a 2D crystal. Even a bilayer of graphene is considered as a 2D crystal of very simple electronic structure consisting of one type of electrons and holes.³² They are referred to as zero band gap semiconductors. However, the electronic property rapidly evolves with the stacking of single graphene sheets together to form a 3D crystal structure. The electronic spectra of such 3D crystal has numerous electrons, holes and an overlapping conduction and valence band to incorporate metal like conductivity in the material. It has been found experimentally that for 3 or more layers of graphene, the electronic spectrum becomes complicated with several charge carriers and the semiconductor property is deployed. The structure is then considered as a thin film of graphite, a 3D material. The screening length in graphite is only 0.5 nm³³ and the interlayer distance is 0.34 nm.³⁴ Hence the surface and the bulk property of a thin graphite film can easily be distinguished if it consists of more than four layers.

Isolation of monolayer graphite or graphene from bulk in large scale and usable form remained as a challenge to material scientists and chemists for a decade. The scotch tape method³⁵ was unique but had limitations towards large scale application. Other methods included chemical exfoliation, intercalation and surface functionalization to obtain modified graphene in suitable form for diverse applications. But chemical modification such as oxidizing graphene to form graphene oxide (GO), certainly disrupted the electronic conjugation of the graphene plane and hence resulted in lower conductivity as compared to pristine graphene. The conductivity was

however regained by reducing and restoring the conjugation to a certain limit in reduced graphene oxide (RGO), which shared many of the properties of pristine graphite. RGO nanosheets had unique physical and electrical properties, were easy to prepare and manipulate and thus produced greater hope to make a revolutionary move from scientific research to exciting practical applications.

1.1.3 Hybrid nanostructured materials: multilayer films

Multilayer films fabricated by the Langmuir-Blodgett technique^{36, 37} and chemisorption from solution had been studied extensively in the past decades as it facilitated fabrication of multicomposite molecular assemblies of tailored architecture. However, those techniques were only useful with certain classes of molecules and so limited with their versatility. An alternative approach - layer-by-layer (LBL) sequential adsorption of different components, was introduced by Decher et al. in the early 1990s³⁸ to fabricate multilayer films. The driving force was the electrostatic interactions, which led consecutive adsorption of polyanions and polycations to give super lattice architecture of the film. The technique was more general, effective, simple and versatile to fabricate conformal coatings in micro and nanoscale with complex hetero structured materials. Hence, it received tremendous attention and made rapid progress in film preparative methodologies and functional film materials. Later extensive research on multilayer films found that the driving force for LBL film fabrication was diverse, including electrostatic interactions, hydrogen-bonds,^{39, 40} halogen-bonds,⁴¹ coordination bonds,^{42, 43} charge-transfer interactions,⁴⁴ biospecific interaction (e.g., sugar-lectin interactions),⁴⁵⁻⁴⁷ guest- host interactions,^{48, 49} cation-dipole interactions⁵⁰ and the synergetic interactions of the above forces. Depending on the desired application of the film, sequential adsorption process could also involve different materials. Decher et al^{50, 51} first used this technique with a combination of a polyelectrolyte and a

bolaform material, a rigid rod molecule with two cationic or anionic functional end groups. Besides using several polyelectrolytes like poly(acrylic acid), sulfonated polystyrene, poly(methacrylic acid), poly(allylamine) etc; Rubner and his group succeeded in fabricating functional organic multilayer thin films using conducting polymers, polymer precursors, proteins and in-situ polymerization of polypyrrole. Thus, multilayer films could exhibit wide range of functionalities for applications ranging from optoelectronic devices to drug delivery vehicles depending on the specific nature of the polyelectrolytes and nanomaterials used, solution conditions during and after formation, and the active ingredient, for example, colloids, luminescent nanoparticles, proteins, and so forth. For example, films made up with poly(aniline), and poly(thiophene-3-acetic acid)⁵²⁻⁵⁴ showed conductivity as high as 40 S cm^{-1} . Multilayer films incorporating DNA and proteins coupled ionically with polyelectrolytes were reported to have possible applications as a multi-protein system and in ecological schemes respectively. Charged metal oxide nanoparticles, buckyball and very recently graphene nanosheets were reported to incorporate in multilayer films with various applications. However, the significant progress in multilayer film based research stimulated scientists to develop environmental responsive multilayer-based devices in early 21st century. For the first time, Mendelsohn et al.⁵⁵ reported porosity transition in multilayer films, based on weak polyelectrolytes PAA and PAH, which were later suggested by others for their potential application in antireflection coatings⁵⁶, Bragg reflector⁵⁷ and optical shutters. Post deposition sequential pH treatment was employed to create nano or microporous structure in PEM film by Breg et al. , which eventually served as a device for loading and releasing of charged drug in a controlled manner⁵⁸. PAH/Silica nanoparticle based multifunctional nanoporous thin film coating and a self cleaning all nanoparticle thin film made up of silica and titania nanoparticless⁵⁹ were reported from Rubner's group. With precise

control over the nanoparticle size and the processing conditions (pH and concentration of the solution), the as prepared films became superhydrophilic, antifogging and antireflective in nature. Thus the propensity of some of the PEMs to change their characteristics at nano and macro scale in response to the external stimuli such as pH, temperature, ionic strength, magnetic field or light opened a new horizon to continue research on ‘stimuli responsive multilayer film’ or ‘smart surfaces’. In the following section 1.2.3, I will provide a brief overview on the responses of multilayer films towards pH and ionic strength and discuss about their response to temperature in detail.

1.2 Functionalization Nanomaterial Surface

In recent years, there is a notable interest in the design and controlled fabrication of the functional nanoscale materials. The interest in these materials stemmed from the fact that their physical, optical and electrical properties are function of their size, composition, and structural order. Therefore, effective strategies to build tailored nanomaterials reliably and predictably were required in order to meet the ever-increasing demands (e.g., structural and compositional complexity) placed on materials synthesis and performance by nanotechnology. To achieve the desired performance from nanomaterials, it was important to either activate their surface and functionalize with active ingredients or embed them in a workable matrix to create a hybrid system in which property of the nanomaterial and the matrix would complement each other. In the following sections, I will give an overview of modifying CNT, graphene and multilayer film surfaces through different processing techniques to accomplish various functional properties based on their nanoscale size.

1.2.1 Processing of carbon nanotubes

With the promising applications of CNT in nanoelectronics and energy storage devices, it is highly desirable to disperse and stabilize CNT in workable form with some suitable matrix. In this respect, functionalizing CNT surfaces with small molecules or CNT based polymer composites with well-dispersed CNTs were suggested from different fields to overcome challenges. Although enormous effort had been invested in this field, and nanocomposites with excellent combined mechanical and electrical properties had been reported from research labs, the commercial application of CNTs was still extremely limited, mainly due to the incompatibility between CNT and several solvents or polymers. Currently, there are three major approaches to disperse CNTs and each has its own advantages and disadvantages:

(1) Mechanical exfoliation

The most convenient method to achieve CNT dispersion was shear-intensive mechanical stirring or ultrasonication of CNT in appropriate solvent or polymer solution.^{60, 61} This method was mostly applicable for nanocomposite fabrication, but not suitable for applications which required a stable CNT dispersion in solution and CNT surface functionalization.

(2) Chemical surface modification

Functionalization of the CNT surface with active groups, ionically or covalently, was one of the most exploited techniques to achieve monodispersed CNT in solvents, especially in aqueous solutions. Treatment of CNT with strong oxidizing agents such as oleum, HNO₃ or KMnO₄/H₂SO₄,^{62, 63} functionalized CNT walls, ends and defect sites with hydrophilic groups like carboxylic acids, ketones, and alcohols.⁶⁴ These functional groups provided reactive sites on CNT surface, which led to the formation of covalent linkage to esters,

amides, zwitterions or grafts of polymer chains.^{65, 66} The functionalization helped in CNT purification and solubilization. However, due to the oxidative treatment, the conjugated electronic structure was disrupted and the electrical and mechanical properties of CNTs were deteriorated.

(3) Third component-assisted dispersion

The surfactants,^{67, 68} polymer electrolytes,^{69, 70} proteins,⁷¹ DNAs,⁷² conjugated polymers,⁷³⁻⁷⁸ and block copolymers⁷⁹⁻⁸¹ were of special interest in dispersing CNT in applicable form with non covalent interaction. They could debundle and stabilize CNT through sonication and therefore acted as third component chemicals. The important advantage of this system was that the conjugated structure in CNT remained intact due to the non covalent functionalization and therefore the electrical property of CNT was not disturbed. Among all the materials known so far and listed above, conjugated polymers, especially block co- polymers had shown particularly promising potential for third component-assisted CNT dispersion. Homopolymers had limitations in their solubility and miscibility in most of the organic solvents and water as they had strong π - π interaction in their solid state. P3HT had relatively better solubility and was the one and the most reported conjugated polymer known to disperse CNT. Other conjugated polymers like polypyrrole, polyphenylene were found to disperse CNT when they were polymerized in-situ in presence of exfoliated CNT. Block copolymers due to their unique structure and functionality could form stable dispersion of CNT. Their structure constituted of a conjugated or non conjugated building block which could form strong association with CNT surface and the remaining part took part in solubilizing CNT by providing steric interaction. Block copolymers such as poly(ethylene oxide) (PEO) with

poly(propylene oxide) (PPO) (PEO-PPO-PEO),⁸² polystyrene (PS) with poly(*t*-butylacrylate) (PBA) or poly(vinyl pyridine) (PVP) did not have conjugated building blocks but were reported to be efficient to disperse CNT. P3HT-*b*-PPEGA, P3HT-*b*-PAA, P3HT-*b*-PS, P3HT-*b*-PVP were the new addition to the block copolymer family having conjugated block in their structure. They had been found to have strong π - π interaction with CNT and good solubility in organic solvents.

1.2.2 Processing of graphene

The materials tailored at a nanometric level, such as fullerenes and carbon nanotubes (CNT) had been paid much attention as fillers in developing novel, ultra-strong and conductive nanocomposites due to their unique mechanical, thermal and electrical properties. However, high price and low availability of these materials limited their practical application. Recent studies showed that graphite nanoplatelets (GNP) or graphene could be used as a viable and inexpensive filler substitute for carbon nanotubes⁸³ in nanocomposites owing to the excellent in-plane mechanical, structural, thermal and electrical properties of graphite.⁸⁴ It was very obvious that these excellent properties were relevant at the nanoscale and the manufacture of the conducting nanocomposites was highly dependent on the exfoliation of the graphite down to single graphene sheet in the matrices. However, the challenge remained to achieve complete and homogeneous dispersion of individual graphene sheets in various solvents.⁸⁵ Like CNT and other nanomaterials, the key challenge in the synthesis and processing of bulk-quantity graphene sheets was aggregation. Graphene, a one-atom-thick planar sheet of sp^2 -bonded carbon atoms densely packed in a honeycomb crystal lattice had very high specific surface area. Unless well separated from each other, graphene tend to form irreversible agglomerates or even restack to form graphite through van der Waals interactions. The prevention of aggregation was of particular importance for

graphene sheets because most of their unique properties were only associated with individual sheets.

(1) Intercalation of small molecules by mechanical exfoliation

Agglomeration in graphite can be reduced appreciably by incorporating small molecules in between the layers of graphite or by non-covalently attaching molecules or polymers onto the sheets. In this context, graphite intercalation compounds (GIC) are very important and popular. In this type of compound, the graphite layers remain unaltered and the guest molecules or atoms are located in the interlayer galleries. When the layers of graphite interact with the guest molecules by charge transfer, the in-plane electrical conductivity generally increases but when the molecules form covalent bonds with the graphite layers as in fluorides or oxides the conductivity decreases as the conjugated sp^2 system is disrupted. The first graphite intercalation compound (GIC) or commonly known as expandable graphite was prepared by Schafhautl in 1841 while analyzing crystal flake of graphite in sulphuric acid solution. In laboratory, flake graphite was subjected to shear intensive mechanical stirring with ultrasonic solvent in the ultrasonic cleaning bath at room temperature to prepare expandable graphite. Experimental conditions involved ultrasonic solvent, ultrasonic power (nominal power of 500 W and 250 W) and ultrasonic time. After the treatment, the mixture was washed thoroughly with water to neutrality and dried below 60 °C for 60 min. The expandable graphite (GIC) was then expanded at 900 °C to obtain the expanded graphite (EG). The choice of ultrasonic solvent depended on the oxidation ability and water content of the solvents, which affected the volume of expanded graphite. Acetic acid, acetic acid anhydride, conc. sulfuric acid and hydrogen peroxide were the examples of few ultrasonic solvents. Among all those, concentrated sulfuric acid had been

proved to be the best ultrasonic solvent to provide optimum condition for preparing the expandable graphite. Such sulphuric acid intercalated graphite compound consisted of layers of hexagonal carbon structure within which H₂SO₄ was intercalated. EG could be prepared either by oxidation with a chemical reagent or electrochemically in the intercalating acid.^{86, 87} They could expand up to a hundred times in volume at high temperature⁸⁸ due to the thermal expansion of the evolved gases trapped between the graphene sheets. So it was reasonably assumed that oxidants and other molecules could enter in the interlayer space of EG more easily compared to natural graphite. The influence of ultrasonic solvent and ultrasonic power on the volume of expanded graphite could be analyzed from the data in Table 1.3.

Table 1.3 The influence of ultrasonic solvent and ultrasonic power on the volume of expanded graphite.⁸⁹ (Reproduced from [89] with permission from Elsevier)

Ultrasonic Power (W)	Ultrasonic Solvent	Ultrasonic Time (min)	Expanded Volume (mL/g)
500	Conc. sulphuric acid	60	500
500	Acetic acid	60	150
500	Hydrogen peroxide	60	140
500	Alcohol	60	120
250	Conc. sulphuric acid	60	380
250	Acetic acid	60	140
250	Hydrogen peroxide	60	100
250	Alcohol	60	80

Li et al. reported exfoliation-reintercalation-expansion of graphite⁹⁰ to produce high quality single layer graphene sheets stably suspended in organic solvents. Commercial expandable graphite was subjected to brief heating (60 s) at 1000 °C in forming gas. It was then ground with NaCl crystals and reintercalated with oleum. The exfoliated graphite was then dispersed in DMF and treated with TBA. TBA could insert into and increase the distance between adjacent layers of graphite facilitating the separation of GS in surfactant solution. The reintercalation and the rapid, brief heating of EG enabled the preparation of highly conducting graphene sheets without functionalizing the graphite.

(2) Oxidation of graphite

At present, chemical conversion of graphite to graphite oxide has been emerged to be a viable route to afford graphene based single sheets in considerable quantities.⁹¹⁻⁹⁵ Graphite oxide (GO) is a layered material produced by the controlled oxidation of graphite.^{96, 97} Compared to pristine graphite, GO is heavily oxygenated bearing hydroxyl and epoxy groups on sp^3 hybridized carbon on the basal plane, in addition to carbonyl and carboxyl groups located at the sheet edges on sp^2 hybridized carbon. Hence, GO is highly hydrophilic and readily exfoliate in water yielding stable dispersion consisting mostly of single layered sheets.^{92, 95, 98-100} Sufficiently dilute colloidal suspension of GO prepared by sonication are clear, homogeneous and stable indefinitely. AFM images of GO exfoliated by the ultrasonic treatment at concentrations of 1mg/mL in water always revealed the presence of sheets with uniform thickness (~1 nm). The pristine graphite sheet is atomically flat with the van der Waals thickness of ~0.34 nm, graphene oxide sheets are thicker due to the displacement of sp^3 hybridized carbon atoms slightly above

and below the original graphene plane and presence of covalently bound oxygen atoms. A similar degree of exfoliation of GO was also attained for N,N-dimethylformamide (DMF), tetrahydrofuran (THF), N-methyl-2-pyrrolidone (NMP) and ethylene glycol.¹⁰¹ Li et al.¹⁰² showed the surface charge of GO as of highly negative when dispersed in water by measuring the zeta potential. This was due to the ionization of the carboxylic acid and the phenolic hydroxyl groups. So the formation of stable GO colloids in water was because of not only its hydrophilicity but also the electrostatic repulsion. However, GO obtained in this way was electrically insulating and contained irreversible defects and disorders,^{100, 103} but the chemical reduction of GO could restore its conductivity partially^{100, 103, 104} at values orders of magnitude below that of pristine graphite. Chemical reduction of GO sheets had been tested with several reducing agents and hydrazine hydrate was found to be the best one in producing very thin and fine graphite-like sheets. During the reduction process, the brown colored dispersion of GO in water turned black and the reduced sheets aggregated and precipitated.^{100, 103} The reduced GO became less hydrophilic due to the removal of oxygen atoms and thus precipitated, although the question of how the hydroxyl oxygen was removed by hydrazine reduction remained unanswered. Li et al.¹⁰⁰ demonstrated preparation of stable aqueous suspension of reduced graphene oxide nanosheets by adjusting the pH (with ammonia solution) of the aqueous solution during reduction with hydrazine. The carboxylic acid groups were unlikely to be reduced by hydrazine and thus remained intact after hydrazine reduction. The adjustment of pH with ammonia solution deprotonated the carboxylic groups and thus the electrostatic repulsion among the charged groups on reduced GO enabled the formation of well-dispersed reduced graphene oxide colloids¹⁰² in water without any

stabilizers. But, unless stabilized by selected polymers, reduced graphene oxide in organic solvent tend to agglomerate due to their hydrophobic nature.^{100, 103} However, the reason of re-establishment of the conjugated graphene network could be attributed to the reaction pathway proposed by Stankovich et al.¹⁰⁰ Hydrazine took part in ring opening reaction with epoxides and formed hydrazino alcohols.¹⁰⁵ This initial derivative reacted further via the formation of an aminoaziridine moiety followed by the thermal elimination of diimide to form a double bond. Another possible route of chemical reduction of GO was with sodium borohydride¹⁰⁴ in aqueous solution. The NaBH₄ treatment eliminated all the parent oxygen containing groups and the resultant solid became IR inactive like pure graphite. Carbon elemental analysis revealed the evidence for the complete reduction of GO in this process.

(3) Surface functionalization of graphite oxide

Changing the surface functionality of GO by chemical modification could also alter the exfoliation behavior of GO. GO was treated with organic isocyanates to give a number of chemically modified GO.¹⁰⁶ Treatment of isocyanates reduced the hydrophilicity of GO by forming amide and carbamic ester bonds to the carboxyl and hydroxyl groups of GO, respectively. Consequently, isocyanate modified GO readily formed stable dispersion in polar aprotic solvents giving completely exfoliated single graphene sheets with thickness of ~1 nm. This dispersion also facilitated the intimate mixing of the graphene oxide sheets with matrix polymers, rendering a novel synthesis route to make graphene-polymer nanocomposite. Moreover, modified graphene oxide in the suspension could be chemically reduced in presence of the host polymer to render electrical conductivity in the nanocomposites.

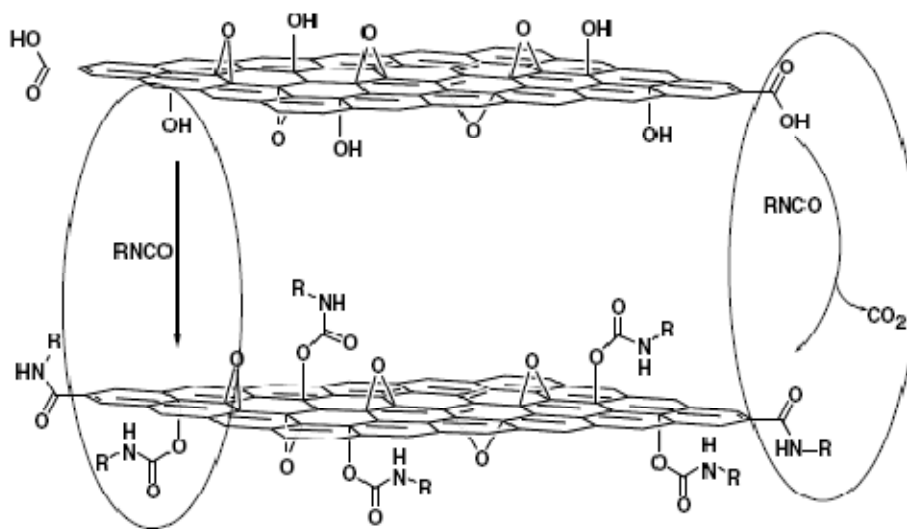


Figure 1.5 Isocyanate treatment of GO where organic isocyanate reacts with the hydroxyl and carboxyl groups of the graphene oxide sheets.¹⁰⁶ (Reprinted from [106] with permission from Elsevier)

Another type of functionalized graphene based material was proposed and made by Bourlinos et. al.¹⁰⁴ GO being an excellent matrix for the interlayer accommodation of long chain aliphatic hydrocarbons¹⁰⁷, transition metal ions¹⁰⁸ and hydrophilic molecules and polymers;¹⁰⁹ it can be used for fabrication of thin films with smart properties. Lerf et al. applied a wide range of chemical transformation on C-OH and epoxy groups of GO. The hydroxyl groups of GO reacted with acetic anhydride (AC₂O) and hexamethylenediisocyanate forming ester or urethane derivatives while epoxy groups formed nucleophilic substituted product with primary amine. Modification of GO with C₁₈H₃₇NH₂ led to the formation of an organophilic solid with its increased dispersion in the order of chloroform > THF > toluene > dichloromethane. Thus the method of preparation and incorporation of single graphene sheet in polymer matrices would develop a new class of nanocomposite material with improved properties and functionalities.

1.2.3 Stimuli responsive functionalized multilayer films

Multilayer films fabricated by layer-by-layer self-assembly technique offered many attractive features based on their various film properties (i.e., thickness, roughness, wettability, porosity and swelling behavior). These properties could be controlled precisely at nanoscale by varying assembly conditions such as pH, ionic strength, temperature, photo irradiation, solvent, mechanical force, polymer functionality, and polymer concentration¹¹⁰⁻¹¹² during film deposition. By manipulating the surface properties of the multilayer thin films, it was possible to achieve adaptive or responsive surface functions towards external physical or chemical stimuli. A number of efforts had already been made in fabricating responsive surfaces based on nanostructured multilayer thin films. The films thus prepared were of special importance towards their application in biological sensors or microfluidic devices.¹¹³⁻¹¹⁵ In particular, change in wettability and surface roughness of multilayer film depending on pH and temperature was paid special attention in my research. Surfaces could be made to switch reversibly from superhydrophobic to hydrophilic^{116, 117} by controlling external parameters like temperature,¹¹⁸ pH, light,¹¹⁹ electricity,¹²⁰ solvent¹²¹ and mechanical force.

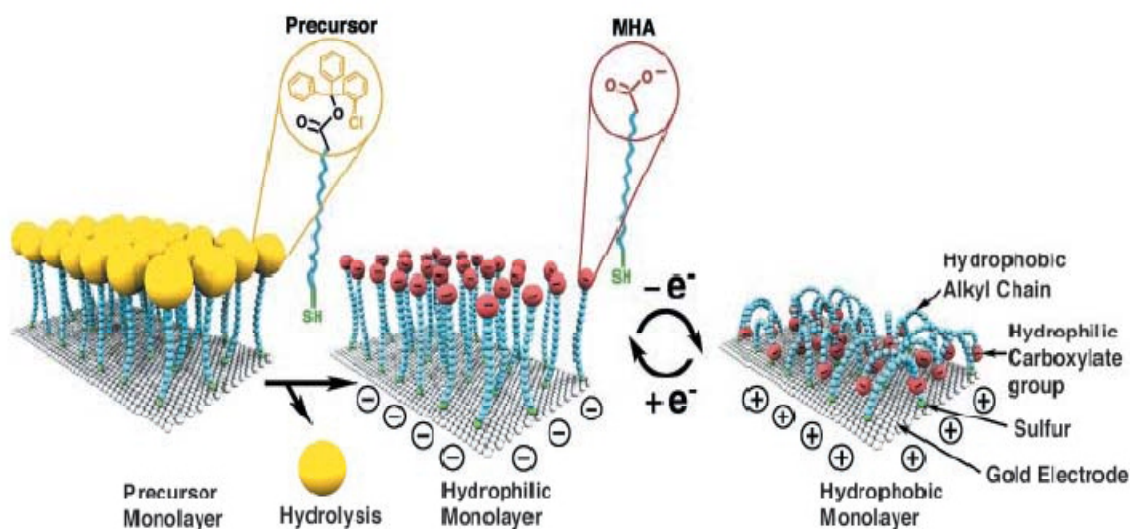


Figure 1.6 Lahann¹²⁰ shows that it is possible to change the surface from hydrophilic to hydrophobic and reverses by applying a voltage between a gold electrode coated with a SAM layer and a reference electrode in water. (Reprinted from [120] with permission from The American Association for the Advancement of Science)

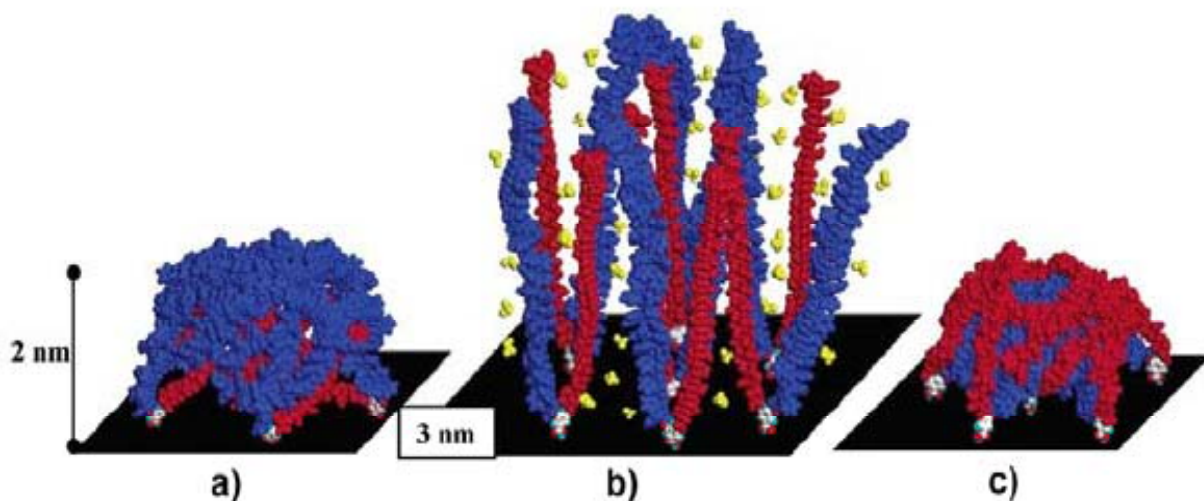


Figure 1.7 Changing of the surface from hydrophobic to hydrophilic and reverses by immersing the samples with toluene or water.¹²¹ (Reprinted from [121] with permission from American Chemical Society)

Also surface roughness could be precisely controlled by selecting assembly pH, salt concentration and size of silica nanoparticles. In the following section, the surface wetting, porosity, roughness of the surface as function of pH and temperature is discussed.

1.2.3.1 Temperature responsive multilayer film

Temperature responsive properties of thin polymer/nanoparticle¹¹⁷ based films on solid surface has been of great interest due to their various applications in the field of separation and controlled delivery. The building blocks of such films included the polymers which could respond to small change in temperature with large reversible change in their polymer coil structure and morphology. One of the most studied polymers of this type was poly(*N*-isopropylacrylamide) (PNIPAAm) and its derivatives, which showed phase transition of the polymer chains from solvated coil to dehydrated globules in aqueous solution when the temperature was increased above its lower critical solution temperature (LCST). PNIPAAm was soluble in water at room temperature through strong hydrogen bonding with water.¹²² Above 32 °C, which was known as LCST for PNIPAAm, the hydrogen bonding was disrupted and water no longer served as a suitable solvent for the polymer. Consequently, PNIPAAm chains formed globules where they made from hydrophobic bonds with neighboring polymer chains.^{122, 123} Layer-by-layer self-assembly was used to prepare thermoresponsive thin films of poly(*N*-isopropylacrylamide) (PNIPAAm) and poly(acrylic acid) (PAA) based on hydrogen bonding. The temperature of PNIPAAm adsorption was shown to significantly affect the film surface morphology and the mass proportion of PNIPAAm in the film.¹²⁴ The films prepared at temperatures closer to the LCST showed reduced surface roughness because of a tighter polymer packing. The authors also demonstrated that the film could be impregnated by low molecular weight dye whose absorption and release through the film could be highly influenced under

thermal stimulus. Dye loaded nanofibers covered with PNIPAAm and PAA multilayers showed different rate of release of the dye at different temperature.¹²⁵ Glinel et al.¹²⁶ demonstrated electrostatically self assembled multilayers and capsules based on copolymers of PNIPAAm with charged monomers. Other charged PNIPAAm derivatives varying in their structure and composition were successfully incorporated in polyelectrolyte assemblies which demonstrated strong stimuli responsive behavior depending on the microstructure of the polyelectrolyte used.

1.2.3.2 pH responsive multilayer film

Multilayer films built up with weak polyelectrolytes were of special interest because they pruned to respond to pH of the medium in their vicinity and consequently many of the physicochemical properties (i.e. acid-base dissociation, surface wettability, surface roughness, film morphology, surface friction, and layer thickness) of such multilayer films underwent dramatic variations with only slight changes in pH and ionic strength of assembly solutions. Weak polyelectrolytes which were popularly and abundantly used in multilayer film fabrication included poly(acrylic acid) and poly(allylaminehydrochloride). The response of the weak polyelectrolytes to pH depended on the presence of ionisable functional groups like carboxylic (-COOH) or amine (-NH₂) in their backbone. These groups readily protonated or deprotonated to attain charge (+/-) at certain pH depending on the pKa of the polymer. Hence, linear charge density along the polymer backbone could be controlled by adjusting the pH of the solution, when operated near the pka of the polymer. The PAA/PAH based multilayer film reported by Mendelshon⁵⁵ exhibited formation of high volume (up to 66%) of micropores in the film when immersed in acidic solution. The density of the pores was only 1/2 to 1/3 that of the original film and they resulted in the reduction in refractive index and dielectric constant of the film. The microporosity of the film was due to the cleavage of interchain ionic bonds by protonation of carboxylate groups in PAA at low pH,

which allowed large scale morphological reorganization and phase separation of the polymer from the acidic water solvent. In addition, porous multilayer films were also fabricated with colloidal silica nanoparticles and polyelectrolytes.¹²⁷ Silica nanoparticles could acquire negative charge due to the hydrolyzation of the silanol groups on their surface at high pH and could behave as polyelectrolytes. At low pH, silica nanoparticles aggregated to give big clusters whereas at high pH they could be used to bind with an oppositely charged polyelectrolyte as well separated small nanoparticles to give adequate surface roughness at nanoscale. Therefore silica nanoparticles also responded to pH and accordingly could change size to give surface roughness in micro and nano scale.

1.3 Outlook

1.3.1 Diverse applications of nanotechnology

The far ranging claims that have been imposed on the potential applications of nanotechnology in the future, involve various fields from all disciplines of basic science and engineering. Nanotechnology has also an impact on several aspects of biology and medical research. The interdisciplinary fields such as biomedical, bionanotechnology, and nanomedicine use unique properties of nanomaterials as contrast agents for cell imaging and therapeutics for treating cancer both in vitro and in vivo. Nanomaterials like dendrimers, block copolymers, NEMs, magnetic nanoparticles have applications in diagnostics, tissue engineering and drug delivery devices. Nanomaterials taking advantage of their increased surface area to volume ratio influence the mechanical and electrical properties of materials with unprecedented stability and huge functionality. Nanotechnology also holds key for reduction of energy consumption by fabricating light emitting diodes using quantum caged atoms, and increases the efficiency of the energy

production by high efficiency solar cells. Novel materials with tailored features and properties at nanoscale have found their applications in information technology (lab-on-chip, memory storage and semiconductor based devices) chemistry and environment (catalyst, ultrafiltration technique using nanoparticles) optoelectronic devices (quantum computers, displays), heavy industry (aerospace, construction, refinery), consumer goods (nano food, optics, textile, agriculture) to name a few.

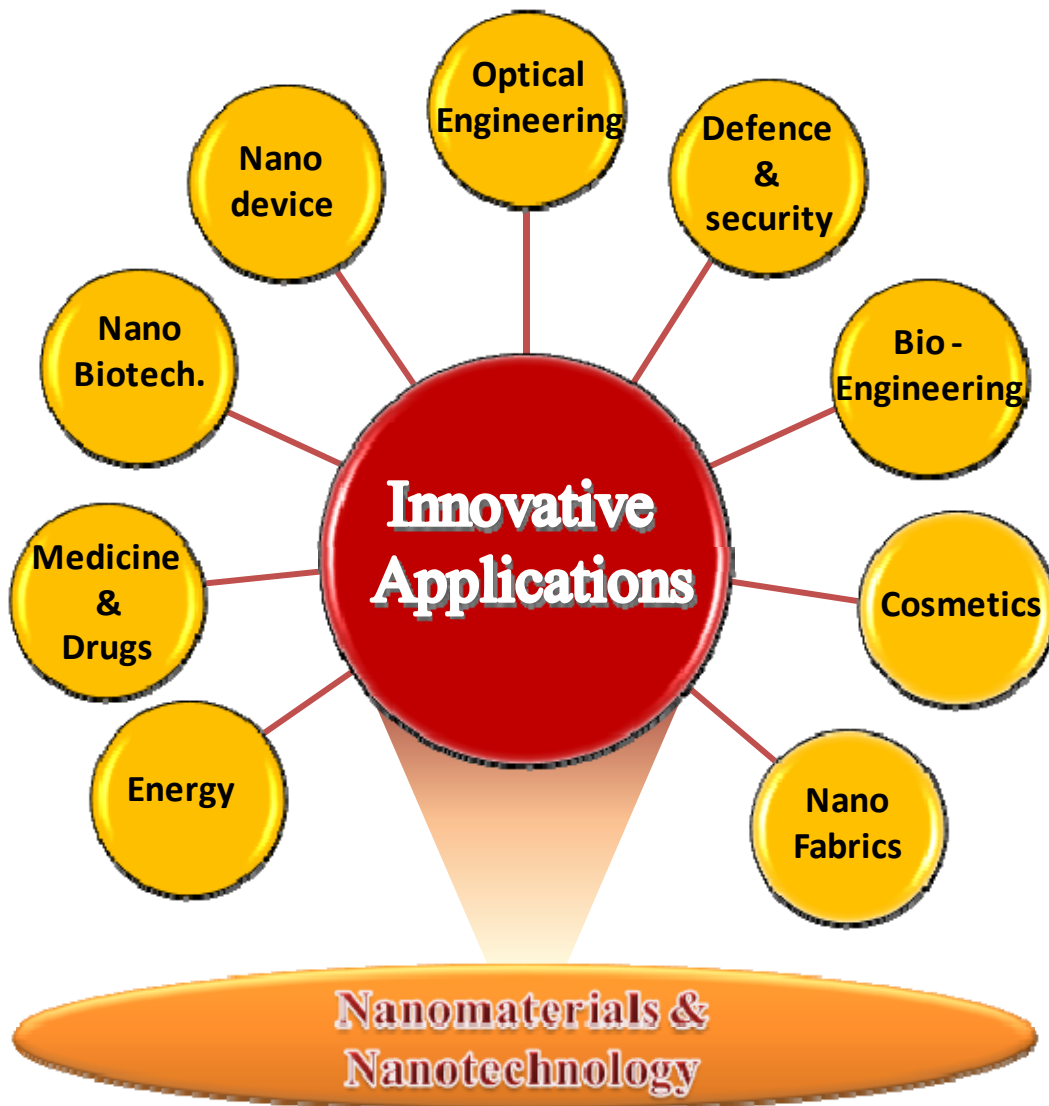


Figure 1.8 Diverse applications of nanotechnology.

1.3.2 Theme of the research

This dissertation research is focused on the synthesis and processing of nanomaterials towards their diverse applications. Nanostructured hybrid organic-inorganic materials are fabricated using basic techniques like LBL and electrospinning. Later, their structure and properties are precisely tuned by various surface treatments (covalent and non covalent functionalization of the surface) to accomplish desired applications. The main theme of this research work is based on the assembly of various nano-dimensional materials to build up a nanostructure in the form of film, fiber or simple composite. These nanostructured materials are then further processed and their surface is modified to endow them with interesting optical, electrical and surface properties. The assembly of nanomaterials is achieved through LBL or electrospinning technique and/or simple method of self assembly between two materials to give a composite structure. For example, polyelectrolyte (PAA, PAH, PSS, PNIPAAm etc.) based multilayer films and their properties are well known, but when the films are made up in combination with polyelectrolyte and silica nanoparticles, they provide flexibility to tune the roughness and refractive index of the film depending on the size of the nanoparticles and assembly pH of the solutions. In chapter two and three the statement has been explicitly demonstrated where the multilayered films made up with PAH and silica nanoparticles are used as a thermosensitive switchable superhydrophobic/hydrophilic surface in one application and antireflection (AR) coating in another. The surface with switchable wetting was achieved by tuning the roughness of the film and modifying the surface with the desired target groups as described in chapter two. The surface is then integrated in a microfluidic channel where it successfully performs as a passive valve ('stop-flow' valve for water). Similar PAH/silica nanoparticle based multilayer films are used as an AR coating on plastic in chapter three. The refractive index of the film is tuned depending on

the size of silica nanoparticles and the assembly pH. The surface of the plastic (PC) is functionalized to bind the multilayer film and the surface of the AR coating is modified to render it abrasion resistant. Additionally, a new approach is introduced to fabricate LBL film in this chapter. Spray coating technique is used to build the film instead of conventional dip coating and the advantage of the new technique over the current one is also demonstrated. Therefore chapter two and three use same technique (LBL) of film forming with similar materials (PAH and silica nanoparticles) but shows diverse applications depending on their processing and functionalization.

Chapter four and five uses a different technique of synthesizing the nanomaterial although the materials used are same as used in previous chapters – weak polyelectrolytes (PAA, PAH) and silica nanoparticles. Ultrathin nanofibers are fabricated by electrospinning technique with PAA and PAH and their pH dependent behavior is studied by testing the loading and releasing of a model cationic drug methylene blue (MB) under different pH conditions. The surface of the fiber is then coated with thermoresponsive layers and the controlled release of the drug is studied with temperature. The fiber surface is also modified with silica nanoparticles and perfluorosilane to make the surface superhydrophobic, and sustained release of drug from the superhydrophobic fiber is studied in different concentration of surfactant solutions in chapter five. So, chapter four and five have basics related to the properties of weak polyelectrolytes, but hold a different fabrication technique which lead to nanofibers which have advantage of having high surface area (high aspect ratio) compared to the multilayer films and can find different applications. Therefore, the research described in chapter four and five is unique and straight forward due to the simple technique of fabricating nanofibers and pH dependent releasing profile, which holds promise for its potential application as drug carrier in biomedical science.

Chapter six and seven deal with the approach of simple self-assembly between two nanomaterials. The materials used are polymeric and organic semiconductors such as P3HT, TSCuPc and reduced graphene oxide (RGO). Two composites are synthesized and studied. One is based on nanostructured 2D P3HT supramolecular structure on RGO nanosheets via self assembly and another TSCuPc dispersed RGO based composite ink. The crystallization process monitored by in-situ UV-Vis spectroscopy indicates the RGO induced P3HT nanowire formation. The testing of the optoelectronic property of the RGO-P3HT composite is due at present. However, the π - π and the charge transfer interaction between the materials are established through Raman and XPS analysis which provides an approach to manipulate the electrical properties of the composite. The RGO/TSCuPc composite is found to be highly photosensitive and holds promise for application in large area optoelectronic devices by the solution processing method. The research based on graphene-P3HT and graphene-TSCuPc composites will open new prospects in preparing molecular devices and generating nanoscale architecture.

In the following chapters of my dissertation, I have highlighted few techniques of material synthesis and described the processing and functionalization of the synthesized materials towards their various potential applications. I have used different techniques (LBL and electrospinning) to form different architectures (films and nanofibers) but with same materials (PAA, PAH, PNIPAAm, silica nanoparticles). The novelty of my research is that the synthesized materials are processed and functionalized precisely so that they all have their unique applications. At the end, I opted a different topic of research based on semiconductors and studied donor-acceptor interactions. The synthesized nano composites are expected to find their application in energy

research. I believe that my exposure to this new research area has given me opportunity to show my capability in conducting research in multidirection.

CHAPTER 2 CONFORMAL SWITCHABLE SUPERHYDROPHOBIC / HYDROPHILIC SURFACES FOR FLOW CONTROL IN MICROFLUIDIC CHANNEL

2.1 Abstract

The development of microvalves is essential to realize a fully integrated system for nano/microliter fluid handling in microfluidic devices. Microvalves that utilize passive fluidic manipulation employ a hydrophobic surface in a microchannel network in which the operation is controlled by the interfacial tension of the liquid–air–solid interface. In order to obtain a switchable valve in microfluidic channels, conformal hydrophobic/hydrophilic and superhydrophobic/hydrophilic thermal switchable surfaces were fabricated by the layer-by-layer deposition of poly(allylaminehydrochloride) (PAH) and silica nanoparticles followed by the functionalization of a thermosensitive polymer-poly(*N*-isopropylacrylamide) (PNIPAAm) and perfluorosilane. A fully integrated microfluidic valve using a thermal switchable superhydrophobic/ hydrophilic polymer patch has been fabricated. At 70 °C, the valve is superhydrophobic and stops the water flow (close status) while at room temperature, the patch becomes hydrophilic, and allows the flow (open status).

2.2 Introduction

2.2.1 Overview on microfluidics

The technology of processing and manipulating small volume of fluids (10^{-9} to 10^{-18} L) in channels with dimension of tens of micrometers was termed as ‘microfluidics’, which attracted increased attention of scientists all over the world. The history of microfluidics could be retraced to the early 1950s, when considerable effort was put to dispense small volume of liquid in nanoliter range, which actually found the basis of today’s inkjet technology. However, the nano and

microscale phenomena were more realized in the early 1980s with the invention of miniaturized gas chromatograph on a silicon wafer. Later, the technology was used for DNA chips, micro pump, micro propulsion, micro thermal technologies etc. Fluids behave differently at their microscale as compared to macroscale. The factors like surface tension, energy dissipation, and fluid viscosity can control the flow of fluid at the miniature level. The flow of a fluid in a microfluidic channel can be characterized by Reynolds's number. Due to the very small dimension of the channel, the Reynolds's number becomes very low (less than 100 and often less than 1.0). Consequently the flow becomes laminar, and fluids usually do not mix in a conventional way when they flow side by side in a channel with diameter of 100 nm to several hundred micrometers. Low Reynolds's number (<100) facilitate momentum based phenomenon like flow separation and laminar flow provides means of molecule transport in a predictable manner. At present, microfluidic devices have various applications in basic biomedical, pharmaceutical research, and chemical reaction and analysis.¹²⁸⁻¹³²

2.2.2 Microvalves

In microfluidic devices, microvalves are basic building blocks for creating stop-flow condition. These are used for delivering a sample fluid with precise regulation and flow rates at the reduced scale. Microvalves have been developed in the form of active or passive forms which are operated via mechanical, non-mechanical or external systems.¹³³ Compared to active valves, passive valves are easy to fabricate, and less prone to clogging as they do not include any moving component such as a membrane or a piston inside. Most popular passive valves are capillary hydrophobic valves which rely on the interfacial tension of the valve material and the sample liquid to manipulate liquid flow in microfluidic systems. For example, a hydrophobic material can be integrated inside the channel and used as a valve to stop the liquid flow.¹³⁴ A

great deal of work has been done on hydro gel based microfluidic valves where the valve changes volume in response to the external stimuli to stop the flow.^{135, 136} Although hydrogels can directly convert chemical energy into mechanical work, which eliminates the requirement of external power source, the fabrication of hydro gels in microfluidics with precise control of position and composition is challenging.

2.2.3 Smart surfaces used as microvalve

Switchable valves using “smart surfaces”¹³⁷ have been investigated for controlling the flow of liquid, and have attracted increasing attentions.¹³⁸⁻¹⁴⁴ The properties of these smart surfaces can be changed by external stimuli¹⁴⁵ such as temperature,¹⁴⁶ pH,¹⁴⁷ photolumination¹⁴⁸ and electric field.^{117, 149, 150} These switchable surfaces are based on the modification of the surface with responsive polymer molecules¹¹⁷ or self-assembled monolayers (SAMs).^{119, 120, 151-155} Such a reversible change of the surface morphology and chemical structures leads to the change of wettability of the surface in response to external stimuli. However, controlling the flow in microfluidic channels requires conformal micron scale valves in selected areas, and all these switchable surfaces and hydro gel based systems are limited by the challenges in micro level fabrication and conformability control.

2.2.4 Working principle of hydrophobic valve

Among various techniques to fabricate conformal coatings, the layer-by-layer (LBL) adsorption of materials through different interactions is now a well-established methodology for creating thin film coatings with precisely tuned physical and chemical properties. This technique involves sequential adsorption of materials that can form intermolecular interactions including opposite electrostatic interactions,¹⁵⁶ hydrogen bondings^{157, 158} and acid–base interactions.^{159, 160} Such

technique has been employed to fabricate superhydrophilic and superhydrophobic coatings^{127, 161-163} and provides a promising approach to fabricate conformal smart coatings for microfluidic valves. A hydrophobic valve utilizes the pressure caused by a hydrophobic patch at the solid–liquid–air interface to stop the liquid flow. The total interfacial energy at the interface, U can be presented as follows:

$$U = A_{sl}\gamma_{sl} + A_{sg}\gamma_{sg} + A_{lg}\gamma_{lg} \text{ -----} \quad \text{Equation 2.1}$$

where A_{sl} , A_{sg} and A_{lg} are solid–liquid, solid–gas, and liquid–gas interface areas, respectively, and γ_{sl} , γ_{sg} and γ_{lg} are their corresponding surface energies per unit area. As the liquid of volume V_L moves onto the hydrophobic patch, A_{sl} increases while A_{sg} decreases. The total energy U is a function of the volume V_L . Therefore, the pressure at the interface can be expressed as

$$P = -\frac{dU}{[dV_L]} \text{ -----} \quad \text{Equation 2.2}$$

The relation between the surface energies and the liquid contact angle θ_y at the solid–liquid–air interface line is expressed in Young’s equation as^{164, 165}

$$\gamma_{sl} = \gamma_{sg} - \gamma_{lg} \cos \theta_y \text{ -----} \quad \text{Equation 2.3}$$

The combination of Equations (2.1) and (2.3) gives

$$U = (A_{sl} + A_{sg})\gamma_{sg} - A_{sl}\gamma_{lg} \cos \theta + A_{lg}\gamma_{lg} = U_0 - A_{sl}\gamma_{lg} \cos \theta + A_{lg}\gamma_{lg} \quad \text{Equation 2.4}$$

where U_0 is constant because $A_{sl} + A_{sg}$ is constant throughout the process.

Including equation (2.4) into equation (2.2) leads to

$$P = -\frac{\partial U}{\partial V_L} = \gamma_{lg} \left(\cos \theta \frac{\partial A_{sl}}{\partial V_L} - \frac{\partial A_{lg}}{\partial V_L} \right) \text{ -----} \quad \text{Equation 2.5}$$

The liquid will flow over the patch when P is positive, and will stop at the patch when P is negative. If the thickness of the hydrophobic patch is negligible compared with the channel size, $\partial A_{lg}/\partial V_L$ is zero and $\partial A_{sl}/\partial V_L$ is positive. Therefore, P is negative when the patch is hydrophobic since the contact angle is larger than 90° . On the other hand, the contact angle at the solid–

liquid–air interface or the wettability of a solid surface largely depends on both its surface energy and roughness. The liquid wetting behavior on rough surfaces is presented by two classical theories.

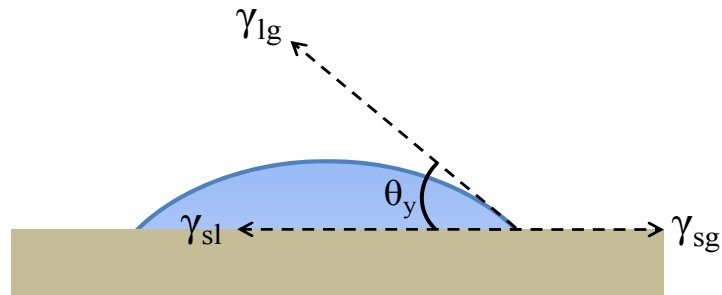


Figure 2.1 Young's model showing water droplet on smooth surface.

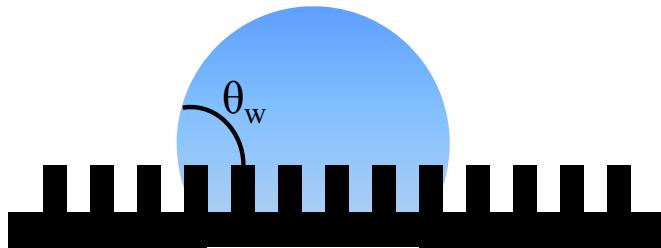


Figure 2.2 Wenzel model showing water droplet on rough surface.

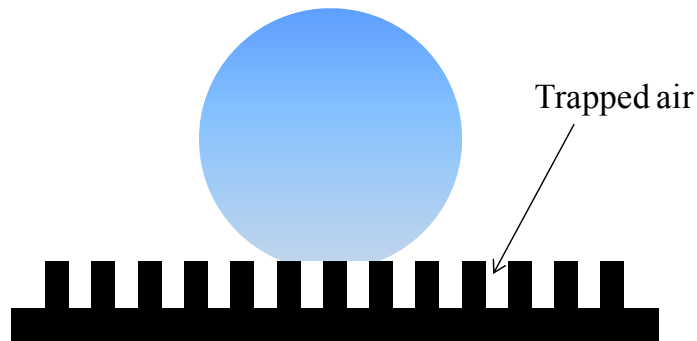


Figure 2.3 Cassie Baxter model showing water droplet sitting on the trapped air in roughness grooves.

Wenzel's model^{166, 167} describes the scenario where the liquid makes a good contact with the rough surface where the roughness increases the contact angle. The contact angle measured on

the rough surface (Wenzel's angle θ_w) can be expressed with the contact angle of the liquid on a flat surface obtained from Young's equation and the surface roughness r

$$\cos \theta_w = r \cos \theta_y \text{ -----} \quad \text{Equation 2.6}$$

In contrast, Cassie-Baxter model describes the wetting behavior of a liquid on a composite surface where a small volume of trapped air below the liquid droplet¹⁶⁸.

$$\cos \theta_c = f_1 \cos \theta_1 + f_2 \cos \theta_2 \text{ -----} \quad \text{Equation 2.7}$$

where θ_1 is the contact angle for component 1 with fraction f_1 and θ_2 is the contact angle for component 2 with fraction f_2 . This equation takes on special meaning when in a two component system with one component being air with a contact angle of 180°. With $f_2 = 1 - f_1$ and $\cos(180^\circ) = -1$, Equation. (2.7) can be reduced to

$$\cos \theta_c = f_1(\cos \theta_1 + 1) - 1 \text{ -----} \quad \text{Equation 2.8}$$

Since the liquid contact angle on a rough hydrophobic surface is larger than that on a flat hydrophobic surface, a rough hydrophobic surface can generate higher pressure to stop the liquid flow than a flat hydrophobic patch. Such concept is important in designing smart valves that can change their wettability to liquid with external stimuli.

2.2.5 Role of thermoresponsive polymer in creating switchable surface

Poly(*N*-isopropylacrylamide) (PNIPAAm) has been widely used in thermal switchable surfaces because PNIPAAm is a thermoresponsive polymer which exhibits its lower critical solution temperature (LCST) in an aqueous solution, and shows a sharp phase transition at ~32 °C.¹⁶⁹⁻¹⁷³ PNIPAAm is soluble in water below its LCST (~32 °C), while at temperatures above its LCST, it forms intramolecular hydrogen bonds and becomes insoluble (Figure 2.4). The water contact angle on a flat PNIPAAm surface is 63 °C and 92 °C at 25 °C and 40 °C, respectively.¹¹⁷

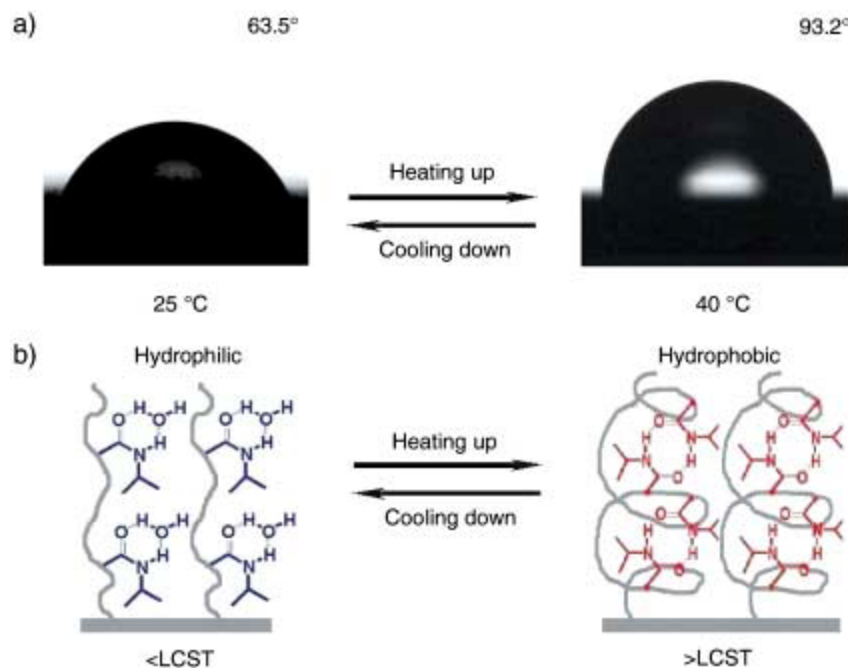


Figure 2.4 Thermosensitive wettability of a PNIPAAm modified smooth surface (a) Change in advancing contact angle of a water droplet when the temperature was increased from 25 °C to 40 °C i.e. above LCST of PNIPAAm (b) Formation of intermolecular hydrogen bonding of PNIPAAm and water molecules and intramolecular hydrogen bonding within PNIPAAm chain.¹¹⁷ (Reprinted from [117] with permission from Wiley-VCH Verlag GmbH & Co. KGaA.)

Such a small contact angle change is not sufficient to manipulate the flow. However, it is clear from the Wenzel model that the surface roughness can make a hydrophobic surface more hydrophobic and a hydrophilic surface more hydrophilic. Based on such concept, it was hypothesized that a conformal rough patch functionalized with PNIPAAm might be able to function as a thermo-stimulated switchable valve in microfluidic channels. The fabrication of a novel thermo-stimulated switchable superhydrophobic/hydrophilic surface and its applications as hydrophobic valve in microfluidic channel is reported in the following section. The layer-by-layer technique was used to build uniform and conformal multilayer films of poly(allylaminehydrochloride) (PAH) and silica nanoparticles with a precise control of film thickness and roughness. The surface was further functionalized with PNIPAAm and a low

surface energy material-(1H, 1H, 2H, 2H perfluorooctyl) silane (perfluorosilane). The combination of surface roughness and chemical composition created a switchable superhydrophobic/ hydrophilic surface. This unique switchable surface was incorporated in a microfluidic channel as a microvalve, and has demonstrated the capability of controlling the flow with the temperature change.

2.3 Results and Discussion

A thermally stimulated switchable superhydrophobic/ hydrophilic surface requires two components: a dual length scale structure that is necessary for building a superhydrophobic surface and a stable cover layer of thermal switchable molecules such as PNIPAAm. The temperature induced molecular formation change enables the hydrophobic or hydrophilic part of the molecular chain to become exposed to a liquid droplet, leading to different wetting behavior (i.e. hydrophilic and hydrophobic). In our studies, rough coatings with both micro- and nanostructures were fabricated by depositing 40 bilayers of PAH/SiO₂ nanoparticles (a mixture of 22 and 7 nm silica nanoparticles) and 3 bilayers of PAH/SiO₂ (7 nm silica nanoparticles) on glass substrates through the layer-by-layer self-assembling technique.¹⁷³ The rough coating was heated at 400 °C for 2 hours to anneal the silica nanoparticles to obtain a robust film. From the atomic force microscopy (AFM) image (Figure 2.5) of the film, both micro- and nanostructures could be clearly observed. Additionally, a layer of perfluorosilane was deposited onto the film via a chemical vapor deposition. After the perfluorosilane treated sample was heated at 140 °C for 2 hours, it demonstrated superhydrophobicity (advancing contact angle = 163° and receding contact angle = 160°), suggesting that such film could provide the structures to generate superhydrophobicity.

In order to generate a uniform stable PNIPAAM layer on the top of the film, PNIPAAM should be grafted from the rough surface. The radical polymerization of *N*-isopropylacrylamide initiated by 2,2'-azobis(2-methylpropionamidine) dichloride (ABMP) was reported to graft PNIPAAM from surfaces with carboxylate groups.¹⁷⁴ In our studies, since no carboxylate groups were available on the annealed surface to immobilize ABMP, two bilayers of PAH/PAA were deposited onto the annealed film via the LBL technique to introduce carboxylate groups on the surface. ABMP was then coupled with the carboxylate group via a coupling reaction catalyzed by *N*-(3-dimethylaminopropyl)-*N*-ethylcarbodiimide (EDC). The subsequent polymerization of *N*-isopropylacrylamide generated a stable PNIPAAM coating on the top the rough surface (Scheme 1).¹⁷⁴

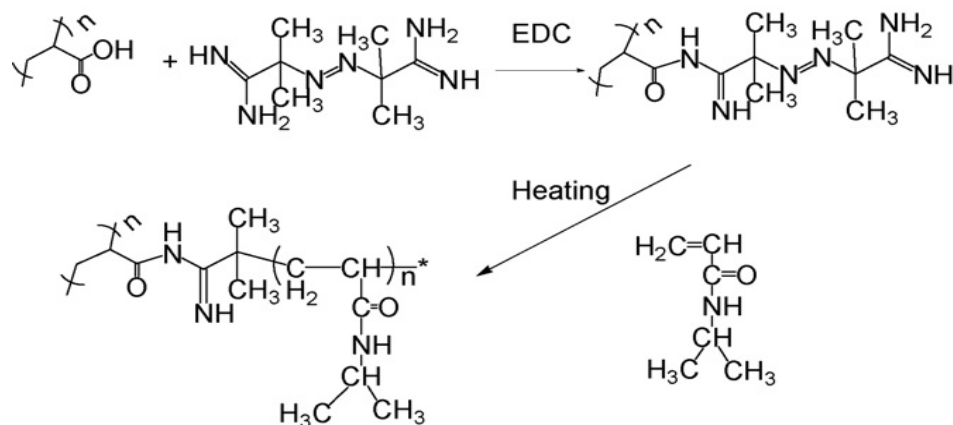


Figure 2.5 Schematic of the synthesis route of grafting PNIPAAM from a surface of PAA.

As described in the Wenzel model, the surface roughness could increase the hydrophobicity of a hydrophobic surface. Therefore, it was important to control the polymerization time because excess PNIPAAM was expected to fill the pores on the rough surface and reduce the roughness. Two samples with different polymerization time were prepared and examined to reveal the relationship between the surface wetting behavior and surface morphology. In the polymerization reaction, one sample (sample 1) was taken out from the reaction solution when the solution

turned milky while the other sample (sample 2) was kept in the reaction solution for 2 hours after the solution turned milky. The surface morphology and surface chemical composition of these two samples were examined by AFM and XPS, respectively. Compared with the AFM image of annealed sample (Figure 2.6 A), the shape of individual silica nanoparticles was still visible in the AFM image of sample 1 (Figure 2.6 B) but was not observable in the AFM image of sample 2 (Figure 2.6 C). This suggested that the short polymerization time would lead to a thin PNIPAAm layer on the rough surface while the long polymerization will generate a thick PNIPAAm layer that would fill the pores on the rough surface and eliminate the nanoscale roughness. However, the nanoscale roughness could be easily regenerated by depositing a layer of silica nanoparticles onto sample 2 by immersing sample 2 into a silica nanoparticle solution. As shown in the Figure 2.6 D, the silica nanoparticles were visible in the AFM image of the resultant sample (sample 3).

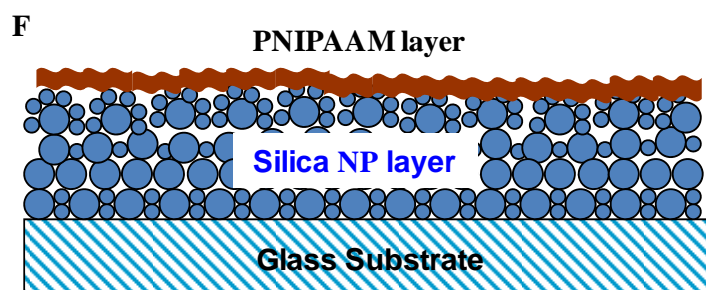
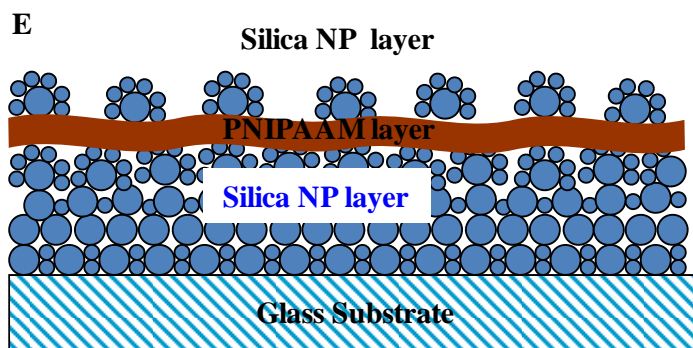
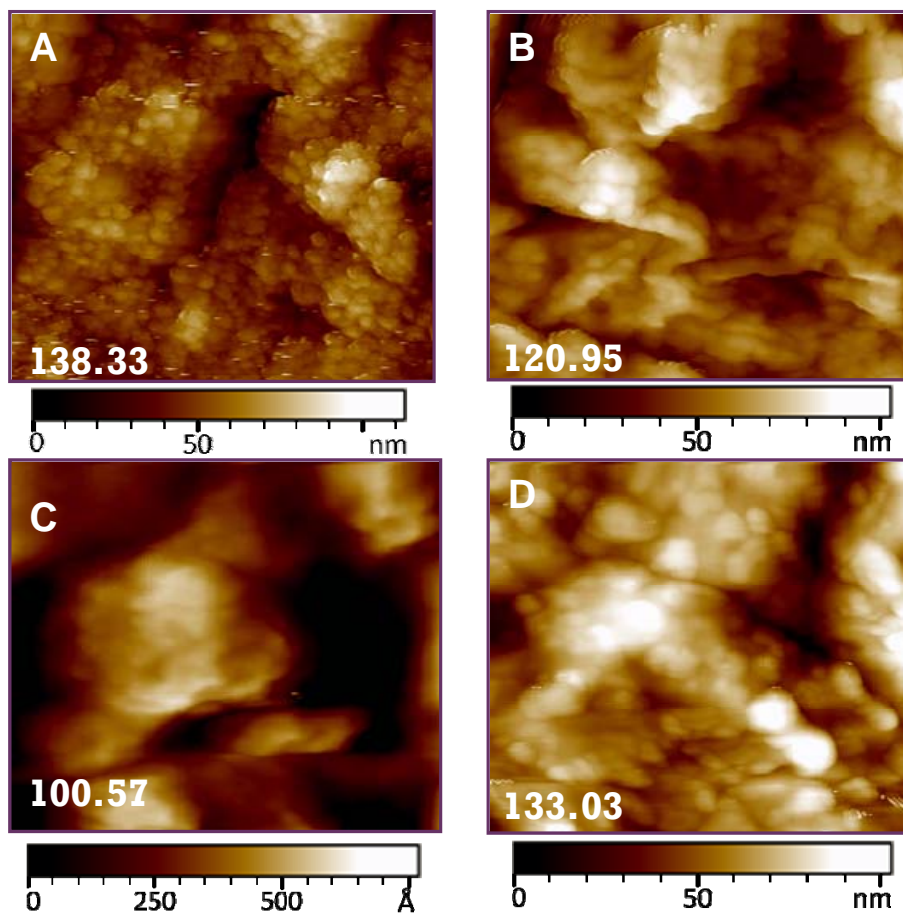


Figure 2.6 AFM height images of (A) annealed PAH/SiO₂ multilayer film with dual-length scale structures (B) A very thin layer of PNIPAAm deposited on rough multilayer film (sample 1). (C) A thick layer of PNIPAAm deposition after 2 hours polymerization which reduces roughness (sample 2) (D) Nanoscale roughness is reintroduced with silica nanoparticle deposition on the thick PNIPAAm polymer film (sample 3) The size of all images (A-D) are 1 μm and the numbers at left corner on each image indicates surface roughness (rms) (E) Schematic illustration of the structure of Sample 2 (F) Schematic illustration of the structure of sample 3.

The XPS survey spectrum of sample 1 (Figure 2.7) showed the reduction of the Si 2p³ peak that was assigned to silica nanoparticles on the annealed film (Figure 2.7) and the appearance of the N peak that was attributed to PNIPAAm, suggesting the formation of a thin layer of PNIPAAm. However, the presence of the Si 2p³ peak indicates that the PNIPAAm layer did not cover the surface completely. In contrast, no Si 2p³ peak was observed in the XPS survey spectrum of sample 2 (Figure 2.7), suggesting that the silica layer was completely covered by the PNIPAAm polymer layer. The appearance of Si 2p³ peak and the absence of N peak in Figure 2.7 indicated that PNIPAAm was covered by silica nanoparticles in sample 3.

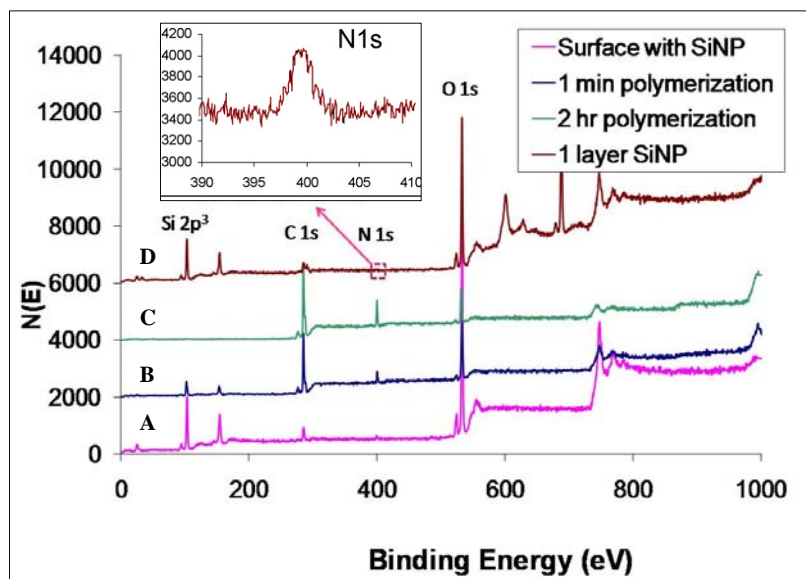
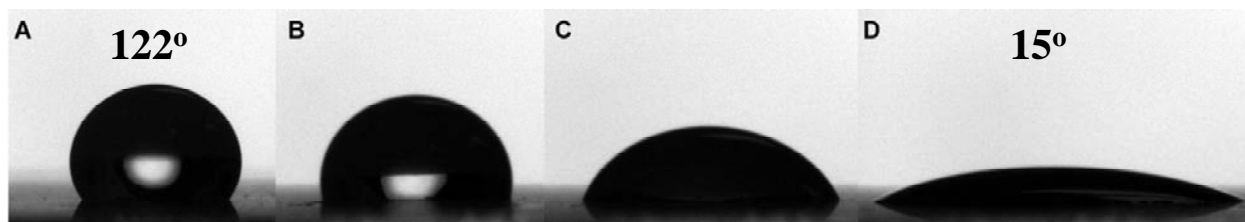


Figure 2.7 XPS analysis of the (A) surface composition of an annealed silica nanoparticle film, (B) a rough silica film covered with a thin layer of PNIPAAm (sample 1), (C) a rough silica film covered with a thick layer of PNIPAAm (sample 2), and (D) a rough PNIPAAm functionalized silica film covered with a layer of silica nanoparticles (sample 3).

The thermo-stimulated switchable wetting behavior of sample 1 and sample 2 was investigated by monitoring the change of water contact angle with temperature. Figure 2.8 showed the change of water contact angle with temperature for sample 1. The largest water contact angle was 122° at 70°C and it decreased with the decrease of temperature. A fast decrease of the contact angle took place around 32°C (LCST of PNIPAAm) due to the change of the PNIPAAm molecular structure from intramolecular hydrogen bond (hydrophobic) to intermolecular hydrogen bond (hydrophilic). Although a superhydrophobic surface was not obtained from sample 1, the difference between the largest contact angle (122° at 70°C) and the smallest contact angle (17° at 20°C) is 105° which is much larger than that on a flat PNIPAAm surface (29°).¹⁷⁵ This result was consistent with the Wenzel model and suggested that a rough surface could greatly increase the hydrophobic/hydrophilic contrast of a switchable surface. In contrast, the water contact angle changed from 92° to 65° on sample 2 due to the reduced surface roughness. Sample 3 was superhydrophilic due to the coverage of silica nanoparticles on the surface. After it was coated with perfluorosilane, it turned into superhydrophobic but did not show any superhydrophobic/hydrophilic switching properties. We believed that PNIPAAm was buried underneath the silica nanoparticles, and did not contribute to surface wetting properties. Therefore, in order to generate a superhydrophobic/hydrophilic switching surface, silica nanoparticles should not fully cover the PNIPAAm surface, which would allow the exposure of PNIPAAm. To make a superhydrophobic/hydrophilic switchable surface, a surface roughness and a partial exposure of PNIPAAm was required. The PNIPAAm grafted surface (sample 2) was immersed into a 0.01M solution of poly(acrylic acid) [PAA] for 1 minute followed by dipping into 0.01M solution of poly(allylaminehydrochloride) [PAH] for 1 minute to prepare a adhesive layer for silica nanoparticles on the surface. A layer of silica nanoparticles was then deposited on the sample 2

surface using a 0.02% silica nanoparticle solution and the short dipping time (2 minutes) to introduce nanoscale roughness and partially cover the PNIPAAm layer. A layer of perfluorosilane was then deposited on the sample surface followed by the heat treatment to alter the surface wetting properties. The partial coverage of the PNIPAAm was determined and optimized with the help of AFM and testing the switching performance of the surface. High resolution XPS analysis reveals the presence of N on the surface and confirms a scattered deposition of silica nanoparticle onto the PNIPAAm layer (Figure 2.7). The thermo-stimulated switchable wetting behavior of the sample was investigated by monitoring the change of water contact angle with temperature. As shown in Figure 2.9, the largest water contact angle is 160° at 70°C with a receding contact angle of 151° . Such superhydrophobic surface is attributed to the combination of surface structures and hydrophobic silica nanoparticles and PNIPAAm at this temperature. The small hysteresis (5°) suggests that PNIPAAm chains maintain their hydrophobic structures at high temperature with the exposure to water. The water contact angle decreases with the decrease of temperature and reaches 70° at 28°C . At this temperature, PNIPAAm becomes hydrophilic and change the surface wetting properties. The dramatic decrease in contact angle was observed around 32°C , which suggested that PNIPAAm turned into hydrophilic at its LCST and changed the surface from hydrophobic to hydrophilic. The superhydrophobic/hydrophilic switchable surface was used to build a thermo-stimulated valve in a microfluidic channel.



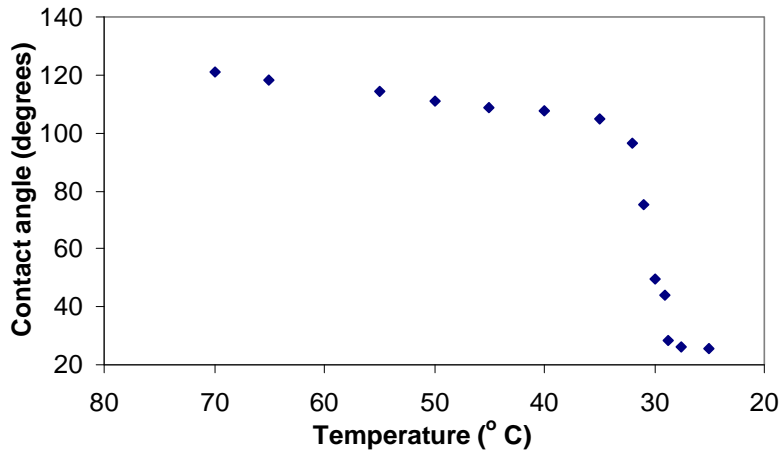


Figure 2.8 The change of water contact angle Vs temperature on a hydrophobic/hydrophilic switchable surface.

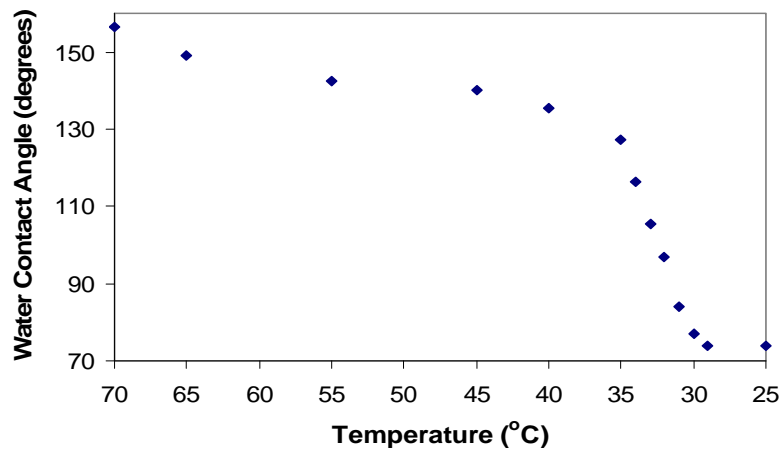


Figure 2.9 The change of water contact angle Vs temperature on a superhydrophobic/hydrophilic switchable surface.

2.3.1 Fabrication of the microvalve

The valve was made by wet etching a glass substrate to create channels of around 50 μ m in depth (Figure 2.10). A positive photoresist (Microposit S1813, Shipley) was spin coated on the etched glass slide and patterned photo lithographically to produce openings for the selective polyelectrolytes deposition on the exposed area of the channel¹⁷⁶. The superhydrophobic/hydrophilic surface was built by the deposition of different materials according to the following sequence: 40 bilayers of PAH/silica nanoparticles, annealing the sample, 3 bilayers of PAH/PAA, the coupling of initiator 2,2'-azobis (2-methylpropionamide) dichloride (ABMP) with PAA catalyzed by *N*-(3 dimethylaminopropyl)-*N*-ethylcarbodiimide (EDC), polymerization of NIPAAM, one layer of silica nanoparticles, chemical deposition of perfluorosilane, and heat treatment at 90 °C for overnight. The photoresist was removed using acetone. The channel was sealed with a polydimethyl siloxane (PDMS) slab with three openings (Figure 2.10). The scanning electron microscope images of the channel cross section Figure 2.10) show that the multilayer deposition and subsequent functionalization creates a conformal uniform coating (about 2 μ m thick) on the opening of the etched channel. The patch thus created has a dimension of 2mm \times 1.4mm. For the valve test, the device was heated with the help of a micro heater up to a temperature of 70 °C. A programmable syringe pump (Harvard PHD 2000) was used to pump dye-colored water heated at 70 °C at a flow rate of 20 μ l/h into the inlet reservoir. As soon as the water entered the channel in the device, the pumping was stopped and the liquid was allowed to flow in the microchannels under capillary action only. Figure 2.11 shows the operation of the switchable valve at 70 °C at which the PNIPAAM forms intramolecular hydrogen bonds and becomes superhydrophobic. The dyed water could not pass over the film surface after it filled a branch of the channel by a capillary effect. This created the

“stop” condition of the valve. Then the heating source was withdrawn and the device along with the water inside was allowed to cool down to room temperature by placing the whole system on a metal plate. The metal plate acted as a heat sink and the temperature dropped at 30 °C in 15 min. PNIPAAm forms intermolecular hydrogen bonds and become hydrophilic at room temperature of around 30 °C. The hydrophilic patch at low contact angle allowed the aqueous solution to flow through (Figure 2.12). This generated the flow condition of the valve. The “stop” and “flow” state of the valve could be achieved back and forth for multiple times via the cycle of heating-cooling-washing with DI water to remove the possible residue-drying.

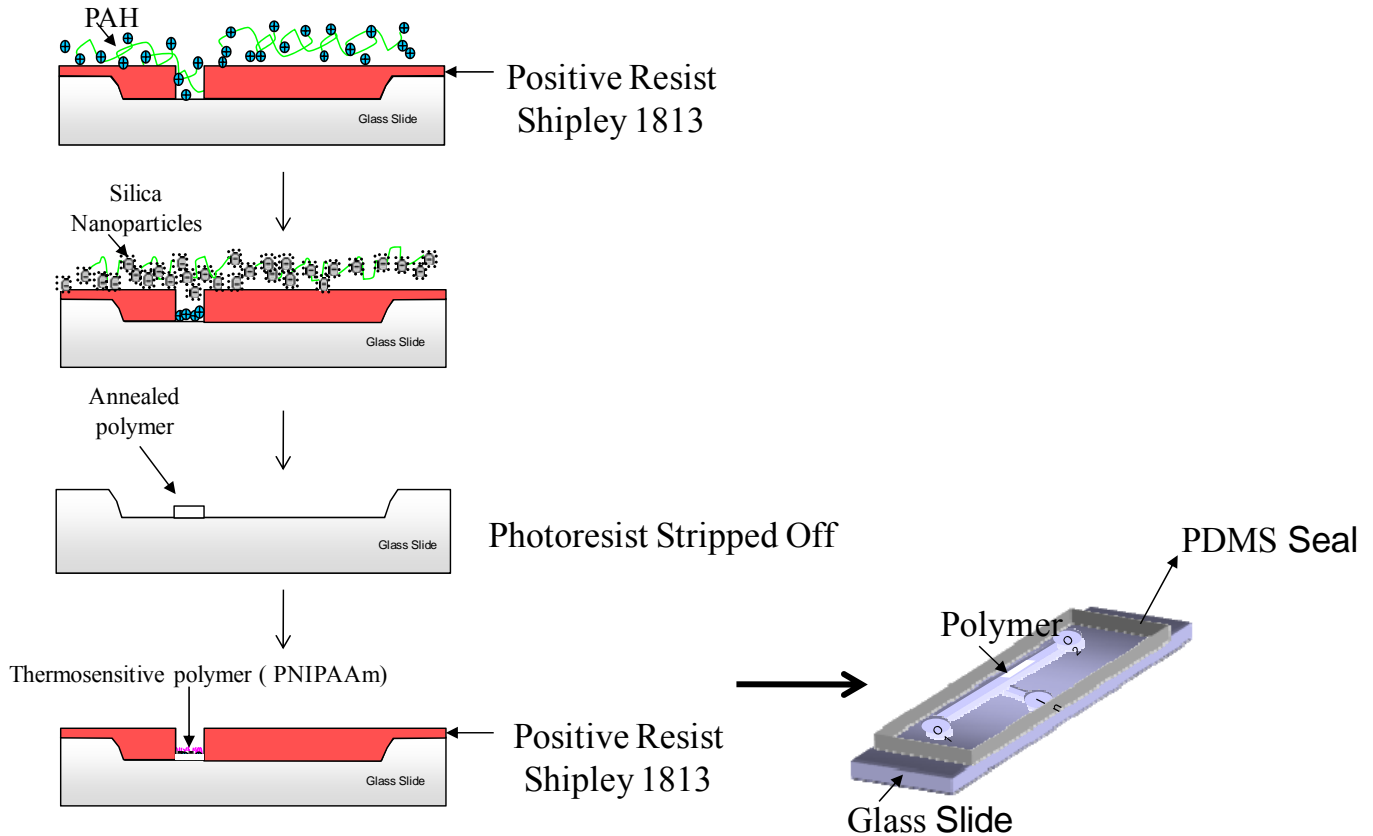


Figure 2.10 Schematic of fabrication of switchable valve in microchannel.

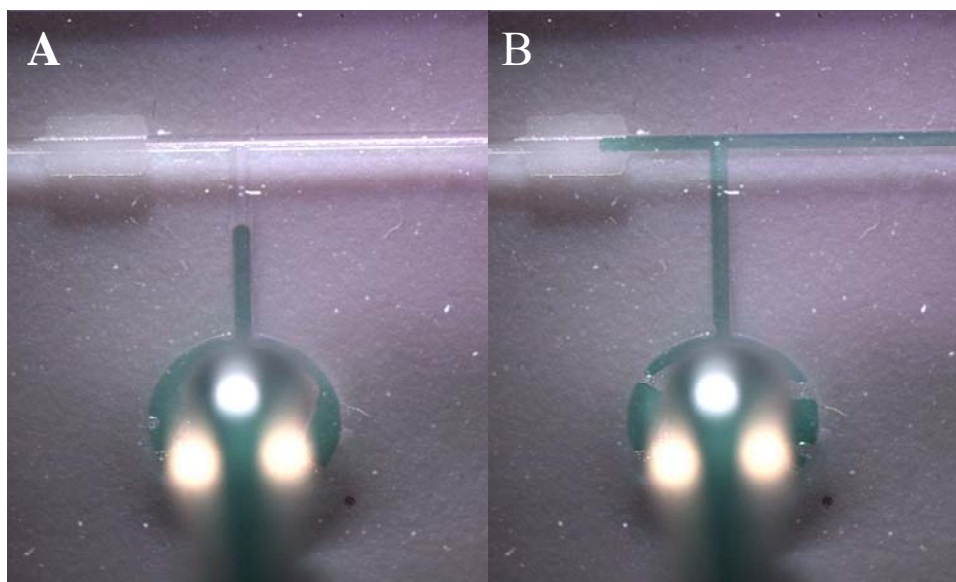


Figure 2.11 Testing of valve at 70 °C A. Dyed water approaches the junction B. Dyed water stops on the patch.

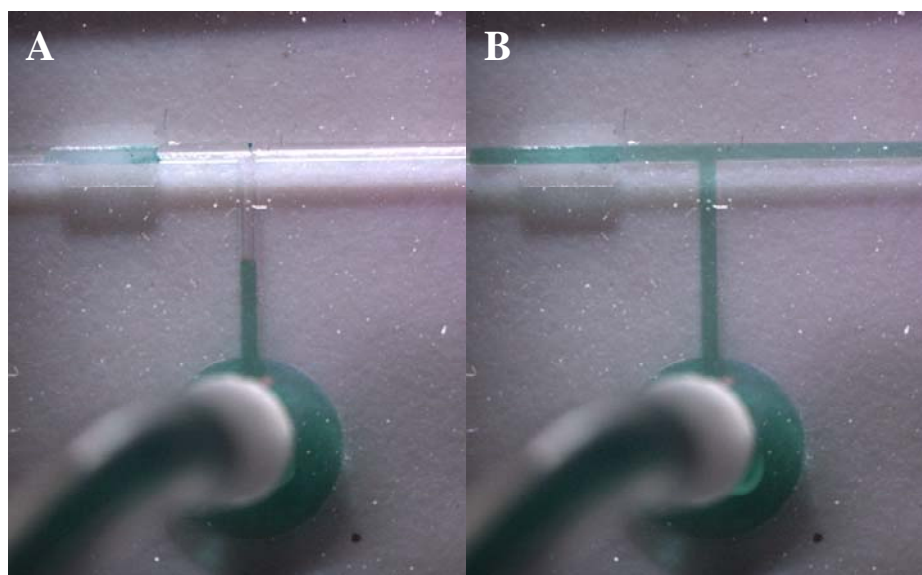


Figure 2.12 Testing of valve at 25 °C A. Dyed water approaches the junction B. Dyed water flows on the patch as it switched to hydrophilic.

2.4 Experimental

2.4.1 *Materials and chemicals*

Pol(allylaminehydrochloride) (PAH) ($M_w \sim 70,000$), poly(sodium 4-styrene sulfonate) (SPS) ($M_w \sim 70,000$) (1H, 1H, 2H, 2H-perfluorooctyl)silane, the colloidal silica nanoparticles Ludox TM-40 (40 wt% SiO₂ suspension in water, average particle size of 22 nm) and Ludox SM-30 (30 wt% SiO₂ suspension in water, average particle size of 7 nm) were obtained from Sigma Aldrich (St. Louis, MO). Poly(acrylic acid) (PAA) (25% aqueous solution, $M_w \sim 90,000$) was obtained from Polysciences (Warrington, PA). Deionized water ($>18\text{M}\Omega\text{cm}$, Millipore Milli-Q) was used in all aqueous solutions and rinsing procedure.

2.4.2 *Fabrication of rough PAH/silica nanoparticle coatings*

A rough multilayer film was prepared by the layer-by-layer (LBL) assembly of negatively charged SiO₂ nanoparticle and positively charged PAH on glass substrates at room temperature. In a typical LBL deposition, the substrate was first dipped into a cationic solution for 15 min followed by one 2 min and two 1 min rinsing steps using Milli-Q water. Then, the substrate was dipped into an anionic solution for 15min, followed by the same rinsing steps. Prior to the deposition of the PAH/SiO₂ layer, the glass substrates were coated with five bilayers of poly(allylaminehydrochloride) and poly(styrene sulfonate), which acted as an adhesive layer between the glass substrate and the PAH/SiO₂ multilayer. The silica solution consisted of 0.069% (w/v) Ludox SM 30 nanoparticle suspension and 0.081% (by w/v) Ludox TM 40 nanoparticle suspension in a 0.1M NaCl solution. The pH of PAH solution and silica nanoparticle solution was maintained at 7.5 and 9.0, respectively. The LBL created a rough, multilayered, porous polymer film on the glass substrate. On the top of the rough surface, 3

bilayers of PAH and silica nanoparticles were deposited as a topping layer. The pH of PAH solution is maintained at 7.5. The silica solution consists 0.03% (w/v) Ludox SM 30 nanoparticle suspension. The silica nanoparticles decorated the rough polymer surface and increased its roughness. After the film was annealed, 2 bilayers of PAH (pH 8.5) and PAA (pH 3.5) was deposited onto the film with PAA on the top to provide carboxylate groups to couple the initiator.

2.4.3 Initiator coupling

The initiator solution consisted of 1 g of 2,2'-azobis(2-methylpropionamide) dichloride (ABMP) and 0.494 g of *N*-(3-dimethylaminopropyl)-*N*-ethylcarbodiimide (EDC) dissolved in 100 mL of water. The glass substrate with the PAA functionalized nanoparticle film was placed into the aqueous solution of the free radical initiator and allowed to react for 2 hours. Such treatment created an initiator layer on the rough polymer film from which the thermosensitive PNIPAAm could be grafted. The initiator-derivatized sample was rinsed in deionized water, dried, and used immediately for polymerization.

2.4.4 Poly(*N*-isopropylacrylamide) (PNIPAAm) grafting

Thermosensitive PNIPAAm was grafted from the ABMP modified rough surfaces. ABMP modified sample was placed in a 1% NIPAAm aqueous solution, follow by 15min nitrogen gas purge to remove the dissolved oxygen. 0.135 g of ABAH was then added quickly to the solution and the reaction vessel was sealed immediately. Polymerization reaction was carried out typically at 65 °C which was indicated by the change of the clean reaction solution into a milky white suspension. The sample was removed from the reaction vessel as soon as the solution turned milky to ensure a very thin layer of polymer on the film. Another sample was prepared

with 2 hours polymerization to deposit a thick layer of PNIPAAm onto the film. The samples were rinsed with deionized water and dried. The chemical vapor deposition of (1H, 1H, 2H, 2H-perfluorooctyl) silane (perfluorosilane) was performed by putting perfluorosilane and the sample under 1 bar vacuum for 45 min.

2.4.5 Characterization

Atomic force microscopy (AFM) height and phase images were collected using an AFM microscope (Pico SPM) in tapping mode. AFM images were obtained with scan sizes ranging from 500 nm to 1 μ m. All images were obtained using tapping mode imaging with a single silicon probe (force constant of 0.5–9.5 N/m). The scan angle was maintained at 0°, and the images were captured in the trace direction with a scan rate of 56–58 kHz. Contact angles were measured using a Goniometer. The morphology of polymer deposited nanoporous film on glass substrate was characterized using JEOL 6400F scanning electron microscopy (SEM) system with an accelerating voltage of 5 kV for imaging. The chemical state of the elements in the SiO₂ nanoparticle incorporated multilayer film and the grafted polymer was studied by X-ray photoelectron spectroscopy (XPS) with a take-off angle of 90°. The specimen was kept under a vacuum of about 10⁻⁹ Torr inside the chamber of XPS system. The spectrometer was calibrated using a metallic gold standard (Au_{47/2} = 84.0 ± 0.1 eV). Charging shifts produced by the samples were corrected by using the binding energy referenced to that of C (1s) of the adventitious carbon at 284.6 eV.

2.5 Conclusion

Conformal hydrophobic/hydrophilic and superhydrophobic/ hydrophilic thermo-stimulated switchable surfaces were prepared and optimized for a wide range of wettability control by the

layer-by-layer deposition of PAH and silica nanoparticles followed by surface modification. The surface characteristics including morphology and composition in relation to the wettability of the surface were studied. Using a novel synthesis and grafting route, a switchable polymer surface was fabricated and fully integrated into a microfluidic channel. A smart surface-based microvalve was created and tested through the combination of the layer-by-layer self-assembly technique and microfabrication, which promises various new applications in micro flow regulation. The following research work was based on integrating a micro-heater and channels for running cooling water into the device, which helped to decrease the time lag between the open and close status of the valve in the microfluidic channel.¹⁷⁷

CHAPTER 3 FABRICATION OF ANTIREFLECTION COATINGS ON PLASTICS USING SPRAYING LAYER-BY-LAYER SELF ASSEMBLY TECHNIQUE

3.1 Abstract

Anti-reflection (AR) coatings on plastic substrates have been extensively investigated with the development of large-area LCD and LED displays. A robust AR coating on plastics requires strong adhesion to the substrate, precise thickness and refractive index, and abrasion resistance. In this chapter, abrasion-resistant AR coatings were fabricated on polycarbonate substrates using the layer-by-layer spraying deposition of poly(allylaminehydrochloride) (PAH) and silica nanoparticles. The adhesion between the substrates and coatings was enhanced by treating the polycarbonate surfaces with aminopropyltrimethoxysilane (APTS). The porous low-refractive index PAH/silica-nanoparticles multilayers were constructed by the layer-by-layer spraying of PAH and silica-nanoparticles aqueous solutions onto the functionalized substrates. The subsequent treatment of the porous coatings with tetrahydroxysilane leads to stable abrasion-resistant AR coatings. The resultant AR coatings can reduce the reflection from 5 to 0.3%. The reported technique provides a cost-effective method for large-scale production of AR coatings on plastic substrates.

3.2 Introduction

Anti-reflection (AR) coatings have numerous applications in optical and display devices due to their capability of removing ghost images and enhancing the transmittance of light. For the application in display devices such as CRTs, PDPs, and LCDs, the AR coatings should be designed to achieve the highest transmittance in the visible region. The first important homogenous AR coating developed was the single layer film with an optical thickness that is

equal to one quarter of the wavelength at which the coating is effective.¹⁷⁸ In order to obtain zero reflectance, the refractive indices of the substrate n_s , medium n_m , and coating material n_c must satisfy the relation $n_c = (n_s n_m)^{1/2}$. It means that to achieve zero reflectance at the interface between air ($n_m = 1$) and a plastic substrate ($n_s = 1.5-1.6$), the refractive index of the coating material should be ~ 1.25 .¹⁷⁹ However, the most commonly used AR material (MgF_2) has a refractive index of 1.38. If a dense MgF_2 layer is applied to a plastic surface, the reflectance of the air/plastics interface is only reduced from 4 to 1.5%. Two approaches have been utilized to overcome such limitations. One solution is to use multilayer coatings with various refractive indices. Such approach can achieve broadband anti-reflection properties, but the materials with the exact refractive indices required by the theoretical design are not always available.^{180, 181} The other approach is to produce layers with a controlled porosity in order to reduce the refractive index of the layer to the required value of 1.25. However, this method is limited by the fabrication process and the narrow anti-reflection region. On the other hand, Mother Nature has provided a perfect example for efficient broadband anti-reflection coatings. It was first discovered by Bernhard in 1967 that the reflection from the corneas of night-flying moths was close to zero for the purpose of camouflage. Such a high-antireflective property is attributed to a surface layer in which the refractive index varies gradually from unity to that of the bulk material. Without such a layer, the Fresnel reflection coefficient at an interface of two media is equal to $[(n_1 - n_2)/(n_1 + n_2)]^2$, where n_1 and n_2 are the refractive indices of the media (Figure 3.1). However, if there is a gradual change of index, the net reflectance can be regarded as the resultant of an infinite series of reflections at each incremental change in index. Because of this continuous variation, each reflection comes from a different depth from the surface and will have

a different phase. If the transition takes place over an optical distance of $\lambda/2$, all phases are present, there will be destructive interference, and the reflectance will fall to zero.¹⁸²

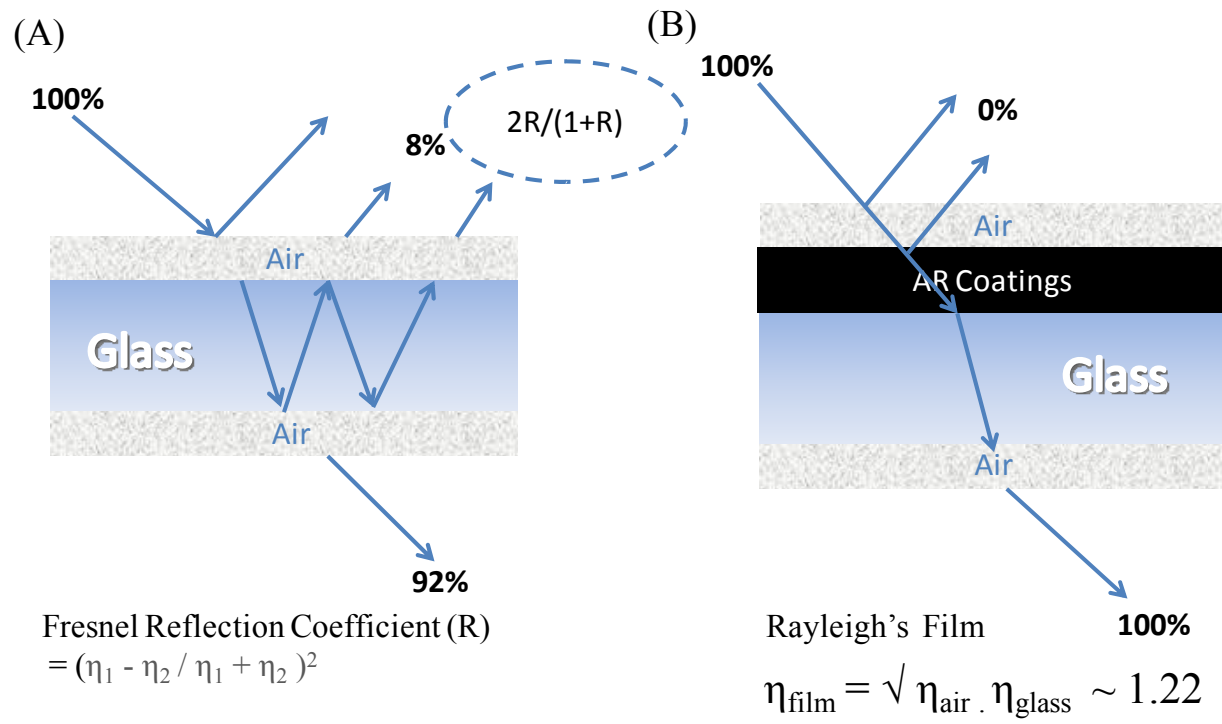


Figure 3.1 (A) Fresnel reflection coefficient at an interface of two media with no AR coating (B) Refractive index of the Rayleigh's film (AR coating) in between air and glass for multiple reflections.

With the development of large-area LCD and LED displays, AR coatings on plastic substrates have been extensively investigated. A robust AR coating on plastics requires strong adhesion to the substrate, precise coating thickness and refractive index, and scratch resistance. Up to now, vacuum coating processes such as chemical vapor deposition (CVD)^{183, 184} and plasma-ion-assisted deposition (PIAD)¹⁸⁵ are the major techniques for producing interference coatings that require a thickness precision in the range of 1 or 2 nm. However, a vacuum-coating process is not cost effective. Another approach to fabricate AR coatings uses wet-chemical coatings such as sol-gel coatings where the low-refractive-index layer is generated by baking at a high

temperature and burning out the organic particles which are in a suspension within a sol-gel coating.^{38, 186, 187} Such an approach is only applicable to temperature-stable substrates instead of plastics. On the other hand, the layer-by-layer (LBL) molecular level adsorption of materials through different interactions is now a well-established methodology for creating conformal thin-film coatings with precisely tuned physical and chemical properties. This technique involves sequential adsorption of materials that can form intermolecular interactions. Intermolecular interactions including opposite electrostatic interactions,¹⁵⁷ hydrogen bonds,^{158, 188} and acid–base interactions¹⁸⁹ have been used in building layer by- layer self-assembled multilayer systems. The monolayer growth of the film is a bottom-up approach and allows the precise control of film composition and dimension in nanoscale. Such technique provides a versatile platform for the assembly of materials and nanostructures of interest in making AR coatings.¹⁹⁰ Besides the conventional dipping procedure, the coatings can be fabricated by the spraying technique, which has the potential to meet the demand for techniques that create AR coatings on plastics in mass production. In this chapter, we report the fabrication of abrasion-resistant AR coatings on polycarbonate (PC) substrates using the aqueous-solution-based layer-by-layer assembly of poly(allylaminehydrochloride) (PAH, positively charged) and silica nanoparticles (negatively charged) combined with a sol-gel treatment. The low-refractive-index porous PAH/ silica nanoparticle coatings were fabricated by alternating sprays of PAH and silica-nanoparticle solutions onto the substrates. The scratching resistance was introduced by treating the PAH/silica nanoparticle porous layer with a sol-gel solution. The resultant AR coatings are able to reduce the reflection from 5 to 0.3%. Such a technique will provide a simple, cost-effective approach to build AR coatings on large area plastic substrates.

3.3 Results and Discussion

Polycarbonates (PCs) are mechanically strong, dimensionally stable, and transparent thermoplastics with extensive applications such as the automotive displays, lenses for eyeglasses, and non automotive vehicle windows. Since a PC substrate has a high refractive index (1.58)¹⁹¹ that leads to more than a 5% reflection on each side, all these optical surfaces require AR coatings to avoid unwanted reflections, improve the contrast of the displays, and increase the transmittance of light. AR coating on the optical glass is a well-established field, whereas the coating on the polymers is under extensive investigation. A robust AR coating on polycarbonate with high optical performance and mechanical properties requires strong adhesion to the substrate, precise coating thickness and refractive index, and abrasion resistance. In this study, various approaches including surface modification, layer-by-layer spraying deposition of PAH and silica nanoparticles, and sol-gel annealing have been applied to build robust AR coatings on polycarbonate substrates.

3.3.1 *Modification of the PC substrate with APTS*

The mechanical properties of the AR coatings on the polycarbonate substrates depend on the interfacial properties between coatings and substrates. Polycarbonates are polymers having functional groups linked together by carbonate groups, which are not able to provide strong adhesion with silica-based AR coatings. In order to generate silanol (Si–OH) groups on the polycarbonate surfaces, the substrates were immersed in a 5% 3-APTS solution for 2 hours, where the 3-APTS slightly penetrated through the PC surface and reacted with the carbonate group (Figure 3.2).

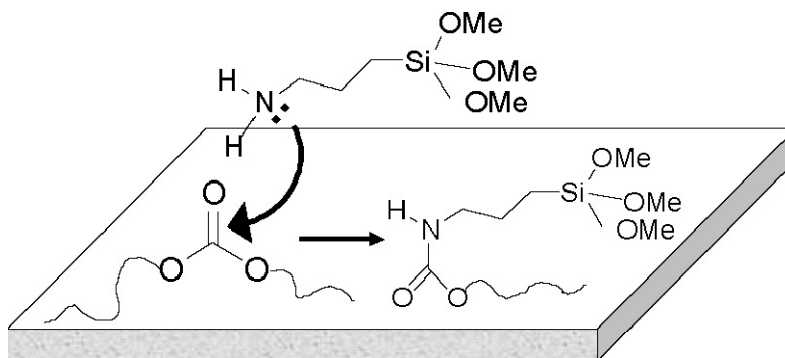


Figure 3.2 Schematic of Functionalization of PC with 3-APTS.

The chemical bonding mechanism of the 3-APTS and polycarbonate surface is based on the aminolysis of the carbonate groups. The selective chain scission of the polycarbonate enabled the trimethoxysilyl groups to react with carbonate groups to form urethane linkage.¹⁹² When the samples were treated with water, the reacted and unreacted 3-APTS molecules were partially hydrolyzed and condensed on the surface as a thin layer of silanol groups. The chemical composition of a 3-APTS modified polycarbonate surface was examined by x-ray photoelectron spectroscopy (XPS) which clearly indicated the presence of silica ($\text{Si } 2p^3$) and nitrogen ($\text{N } 1s$) peaks [Figure 3.4(b)]. This XPS survey spectrum of was compared to that of a bare polycarbonate substrate [Figure 3.4(a)] and a 3-APTS treated glass substrate, which served as a free-amine reference sample [Figure 3.4(c)]. The XPS data of the samples would give the chemical information of the free-amine nitrogen and the urethane nitrogen and ensure the aminolysis reaction on the PC surface. The bare polycarbonate substrate had only carbon ($\text{C } 1s$) and oxygen ($\text{O } 1s$) peaks [Figure 3.4(a)] which were enhanced in the XPS spectra of the APTS-modified PC sample [Figure 3.4(b)]. The enhancement of the carbon and oxygen peak was due to the methoxy groups and the propyl group of the APTS molecules attached to the PC surface. The free-amine nitrogen of the APTS-modified glass surface and the nitrogen of the urethane linkage on the APTS-modified PC substrate could be clearly distinguished by comparing the

binding energies of the N 1S electrons obtained from the high-resolution XPS spectrum of the respective samples (Figure 3.5). The high resolution XPS data showed that the binding energy of the N 1s electron for the 3-APTS modified PC samples was at 400.0 eV [Figure 3.4(a)], while the binding energy of the N 1s electron for the free-amine reference (glass substrate) was at 398.9 eV [Figure 3.5(b)]. Therefore, the XPS nitrogen peak of the APTS-modified PC indicates the formation the urethane groups instead of amine groups.

Additionally, the thin APTS layer on the PC substrate increased the hydrophilicity of the surface, which was confirmed by the contact-angle measurement as in shown Figure 3.3. After the surface modification, the water contact angle changes from 90° to 40°. The increased wettability of the PC surface facilitated the subsequent steps of spray coating and the sol-gel deposition.

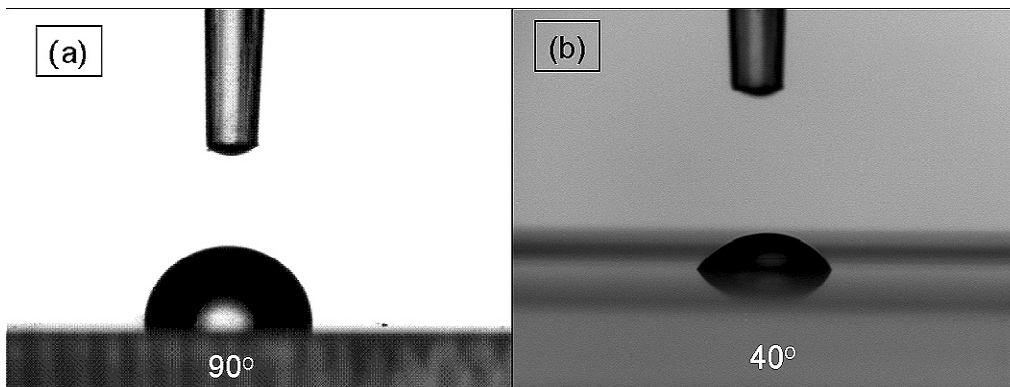


Figure 3.3 (a) Bare PC sample showing contact angle of 90° and (b) an APTS-modified PC sample showing contact angle of 40°.

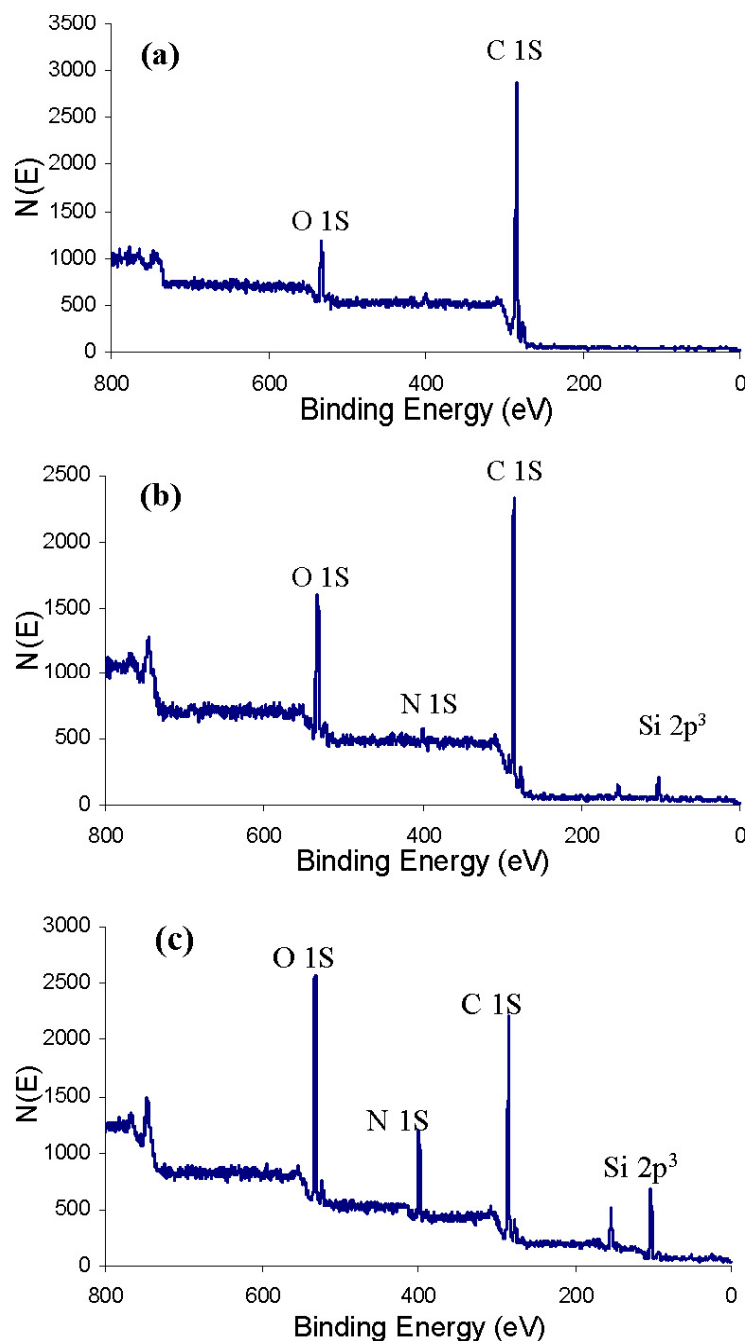


Figure 3.4 XPS spectra of (a) a bare PC substrate, (b) an APTS-modified PC substrate, and (c) an APTS-modified glass sample.

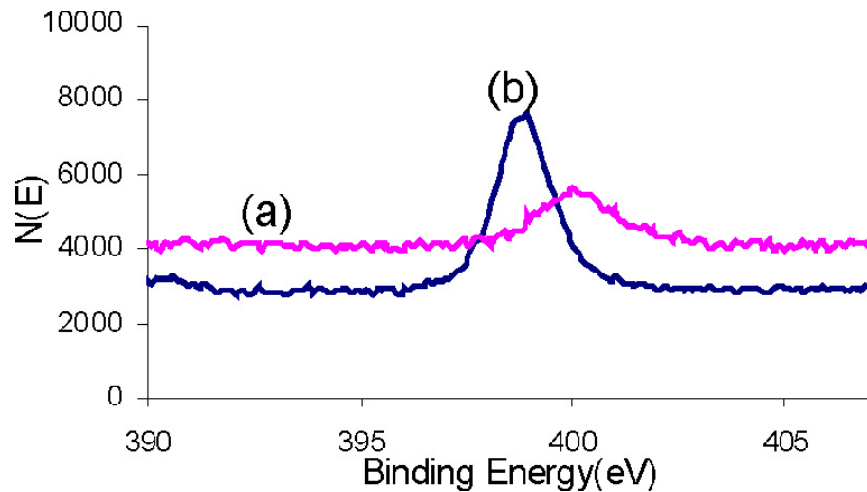


Figure 3.5 Binding energies of the N 1S electrons in (a) urethane linkage of APTS-modified PC surface and (b) free amine of APTS-modified glass surface as obtained from high-resolution XPS analysis.

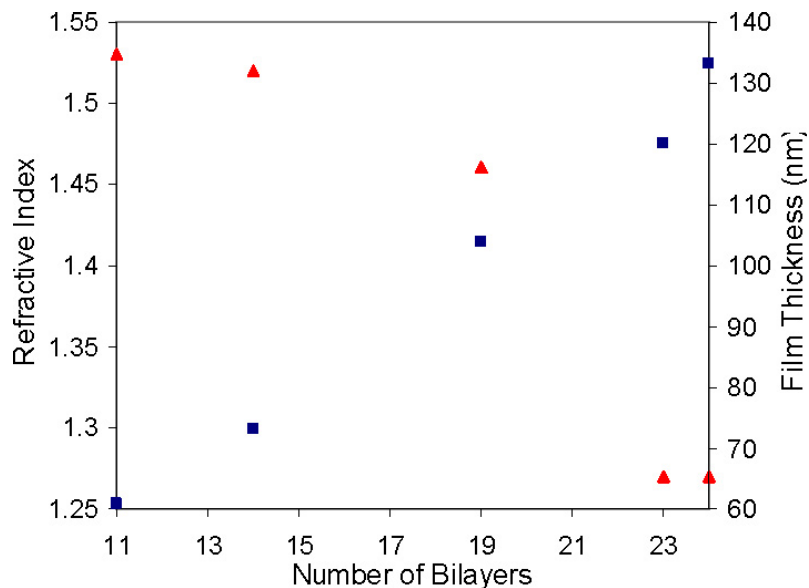


Figure 3.6 The film thickness and refractive-index changes with a number of bilayers deposited (■ symbolizes film thickness and ▲ symbolizes refractive index).

3.3.2 Layer-by-layer deposition of PAH/silica nanoparticle AR coatings on APTS modified polycarbonate substrates

The AR coating was fabricated on the APTS-modified PC surface by the alternating layer-by-layer spraying deposition of PAH and silica-nanoparticle solutions with intermediate rinsing

cycles. To achieve the lowest reflection, the refractive index of the AR coatings should be 1.26, the square root of the refractive index of the PC substrate. Different deposition parameters including the pH of the solutions, the number of layers, and rinsing time were optimized to achieve the highest transmittance with the least number of spraying cycles. In our studies, the refractive index of the coating decreases with the number of PAH/silica-nanoparticles bilayer deposited, which is consistent with the results reported by Rubner et al.¹⁸⁹ (Figure 3. 6). Figure 3.7 shows the UV–Visible transmittance spectra of a sample with 11 bi-layers to 24 bi- layers of PAH/silica nanoparticles deposited on one side of a PC substrate. In Figure 3.6, the transmittance of the coating increases with the film thickness due to the decrease of the refractive index. The highest transmittance (94.6% at 700 nm) is obtained using an AR coating containing 24 bi-layers of PAH/silica nanoparticles with a refractive index of 1.27. Since one side of the polycarbonate substrate is coated with the AR coating while both sides contribute to the reflection. The reflectance of the coated sample includes 5% reflectance of the uncoated side and the reduced reflectance of the coated side. Therefore, the reflectance of the coated side can be calculated by subtracting 5% (reflectance of uncoated side), 94.6% (transmittance at 700 nm), and 0.05% (absorbance) from 100%, which leads to 0.35%. If the transmittance at 550 nm (93%) is considered, the reflectance is reduced from 5 to 1.95%. The adhesion between the AR coating and the APTS modified substrate was examined using a Scotch tape test where a tape is pressed on the AR coating and peeled off at 45°. The AR coatings on the APTS-modified PC carbonate were undisturbed while the AR coating on the bare PC substrate was completely removed with the tape. This result suggests that APTS-modified PC surfaces provide sufficient functional groups to form strong bonding with silica-based coatings. APTS-modified PC substrates were also used in the subsequent studies of sol-gel-modified AR coatings.

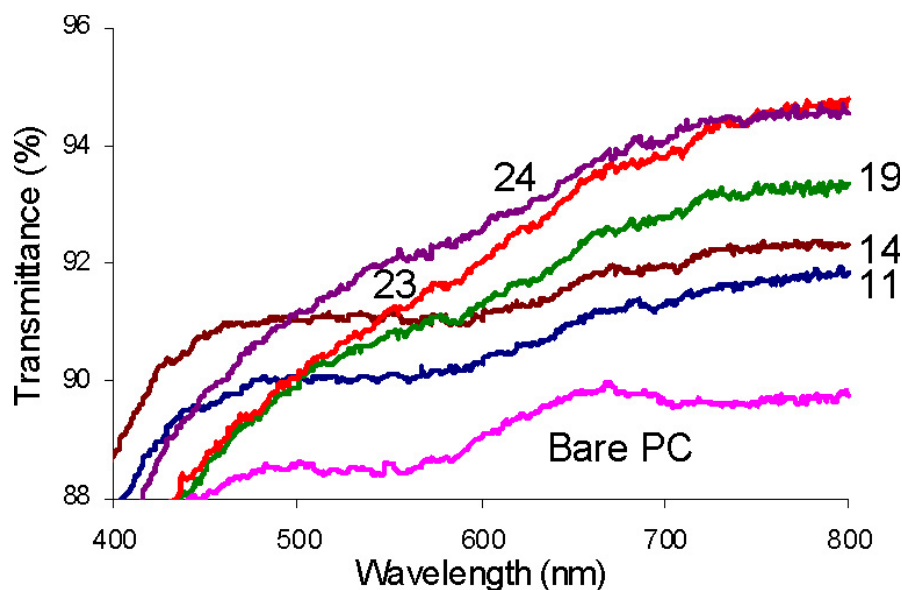


Figure 3.7 UV-visible transmittance spectra of the AR-coated PC substrate with a different number of bilayers as compared to a bare PC substrate.

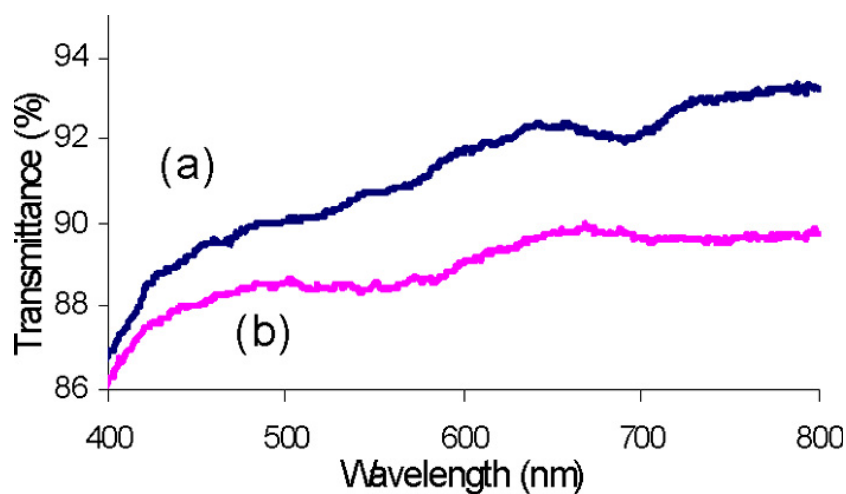


Figure 3.8 UV-Visible transmittance spectra of (a) a sol-gel-modified PC substrate and (b) a bare PC substrate.

3.3.3 Sol-gel coating on APTS-modified PC substrate

It is also observed in Figure 3.7 that a steep drop in transmittance occurs for the coating with 24 bi-layers of PAH/silica nanoparticles at short wavelength, and the reflection is only reduced from 5 to 2% at 550 nm. Such a narrow AR region is probably due to the large difference between the

refractive index of the polycarbonate substrate (1.58) and that of the AR coating (1.27). Reducing the refractive-index difference and building an index gradient has been demonstrated by nature to be an efficient approach to generate high-quality AR coatings. A broadband AR coating with high transmittance in the visible light region has been fabricated by using two layers of coatings with different refractive indices.⁵⁶ Therefore, it is expected that the AR properties at short wavelength will be improved by incorporating one layer of coatings with a refractive index between 1.58 and 1.27 between the APTS-modified PC substrate and the porous AR coating. A sol-gel solution (1.88% by weight) was spin-coated on one side of the APTS-modified PC substrate with a spin rate of 2750 rpm. After aging at room temperature overnight, the sol-gel coating formed a uniform strong silica coating on the APTS-modified PC through the formation of siloxane (Si–O–Si) bonds. The sol-gel layer had a refractive index of 1.52 and thickness of 61 nm. As shown in Figure 3.8, such a thin silica layer has AR properties because it has a lower refractive index than the PC substrate.

Besides improving the AR properties, the sol-gel layer enhanced the attaching of PAH/silica nanoparticles onto the substrate in the layer-by-layer spraying deposition due to the high density of silanol groups on the surface. It was found that the number of bi-layers on the sol-gel-modified surface to achieve optimum transmittance was much less than the number of bi-layers on the APTS-modified substrates. Only 10 bi-layers of PAH/silica-nanoparticle coating on one side of the sol-gel-modified PC substrate are able to produce AR coatings with 94.5% transmittance. In contrast, 24 bi-layers of PAH/silica nanoparticles are required on the APTS-modified substrate to achieve the comparable result [Figure 3.9(c)]. The AR coatings on the sol-gel-modified surfaces had a broad-band transmittance of 93% over a range of 600–800 nm.

Additionally, the AR coating on the sol-gel modified PC [Figure 3.9(b)] has 1% higher transmittance at 500 nm than the AR coating on the APTS-modified PC [Figure 3.9(c)].

Compared with a conventional dipping method, the spraying technique has the potential for mass production. Therefore, it is important to compare the AR qualities of AR coatings fabricated using dipping and spraying deposition. As shown in Figure 3.9(a), the sol-gel-modified PC substrate dip coated with 14 bi-layers of PAH/silica nanoparticles has a similar transmittance in the range of 600–800 nm but higher transmittance at shorter wavelengths compared with the sol-gel-modified PC substrate spraying coated with five bi-layers of PAH/silica nanoparticles [Figure 3.9(b)]. Such dissimilarity is attributed to the different packing density of the silica nanoparticles in dipping and spraying deposition. The surface morphology of the spray-coated and dip-coated AR PC samples was analyzed by an atomic-force microscope (AFM). As shown in Figure 3.10, silica nanoparticles deposited via a spraying approach form looser structures than those deposited via a dipping approach. The loose structure leads to larger thickness and smaller refractive index for each bi-layer of PAH/silica nanoparticles. Therefore, the less number of bilayers of PAH/silica nanoparticles is required to achieve comparable AR properties using the spraying deposition.

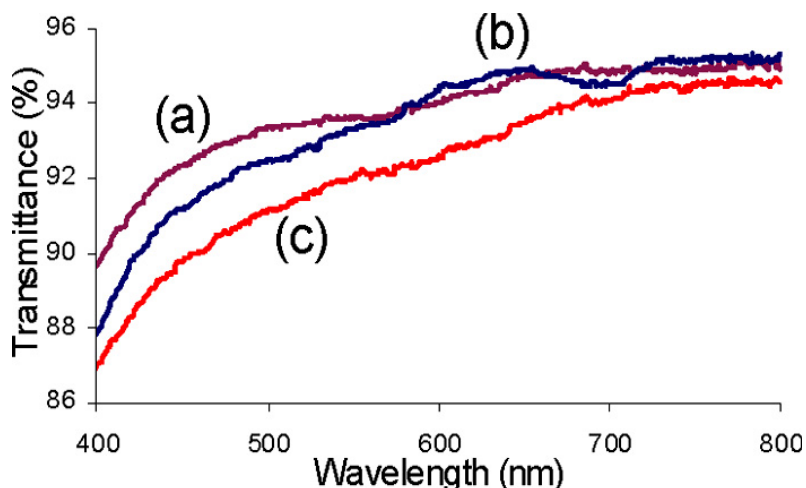


Figure 3.9 UV-visible transmittance spectra of (a) 14 bi-layers of AR coating on one side of a sol-gel-modified PC substrate by dip-coating, (b) 10 bi-layers of AR coating on one side of a sol-gel-modified PC substrate by spraying deposition, and (c) 24 bi-layers of AR coating on one side of the APTS-modified PC substrate by spray deposition.

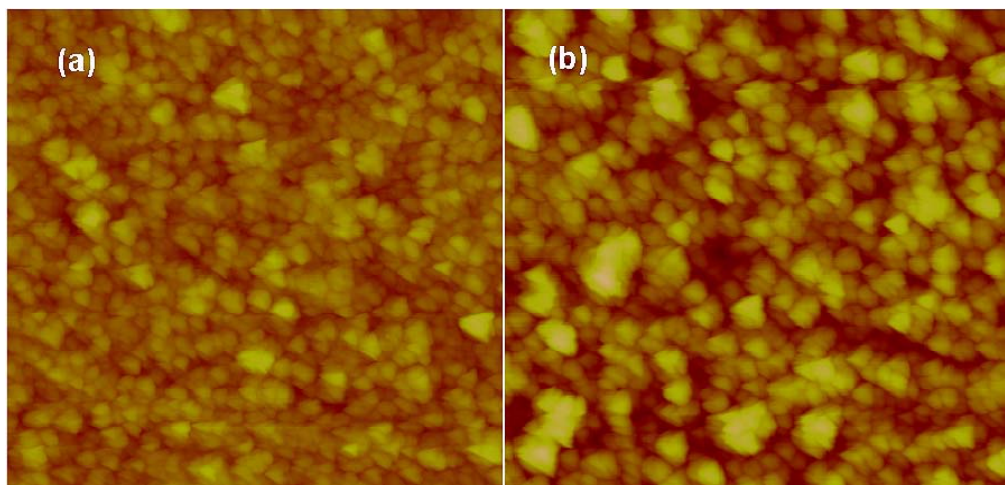


Figure 3.10 AFM images of (a) 14 bi-layers of AR coating on one side of sol-gel-modified PC substrate by dip-coating and (b) 10 bi-layers of AR coating on one side of the sol-gel-modified PC substrate by spray coating. The scale of the images is 5 μm .

3.3.4 Fabrication of abrasion resistant AR coatings

As discussed previously, the spraying layer-by-layer deposition of PAH/silica nanoparticles provides a cost-effective approach to build AR coatings in PC substrates. However, the AR

coatings are very fragile due to the weak bonds (electrostatic bonds) between PAH and silica nanoparticles. The AR coatings can be easily damaged by wiping them with Kimwipes. Therefore, it is essential to toughen the AR coatings for their practical applications. Rubner et al. have made strong AR coatings from polyelectrolyte/silica nanoparticle systems through a hydrothermal treatment where the hot steam (124–134 °C) catalyzed the fusing of neighboring silica nanoparticles.¹⁹³ In our studies, the mechanical performance of the AR coating was improved by treating the porous AR coatings with a sol-gel solution (1% by weight). After the sample was heated at 100 °C overnight, the silica nanoparticles were fused through the reaction with tetrahydroxyl silane in the sol-gel solutions, leading to a uniform hard AR coating. The abrasion-resistant test was evaluated by rubbing the coatings with Kimwipes. No scratches formed on sol-gel-treated coatings, suggesting the abrasion resistant properties. The UV–Visible transmittance of the antireflective PC samples after the sol-gel annealing treatment is shown in Figure 3.11, which indicates that the sol-gel treatment did not affect the antireflection properties of the AR coating. In Figure 3.12, the PC with AR coatings (left slide) shows much lower reflection than the bare PC (right slide). The AR coating not only greatly enhanced the transmittance, but also was abrasion resistant when tested by rubbing with Kimwipes.

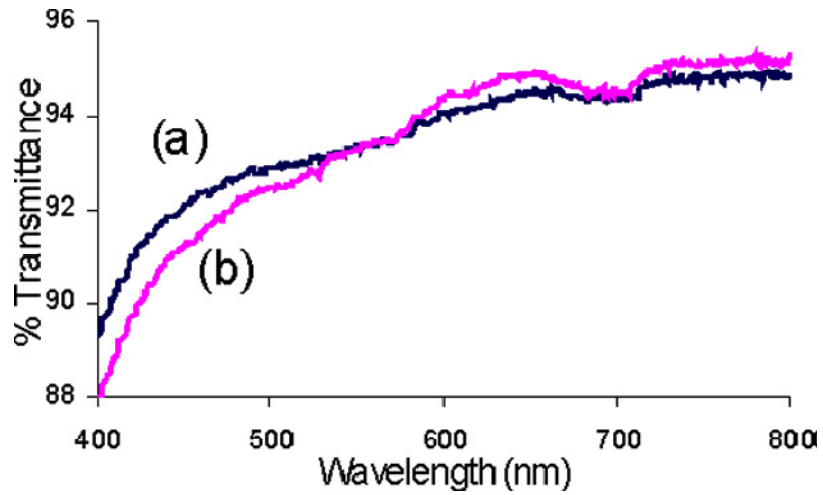


Figure 3.11 UV-Visible transmittance spectra of (a) an AR coating on a PC substrate with the sol-gel treatment and (b) an AR coating on a PC substrate without the sol-gel treatment.

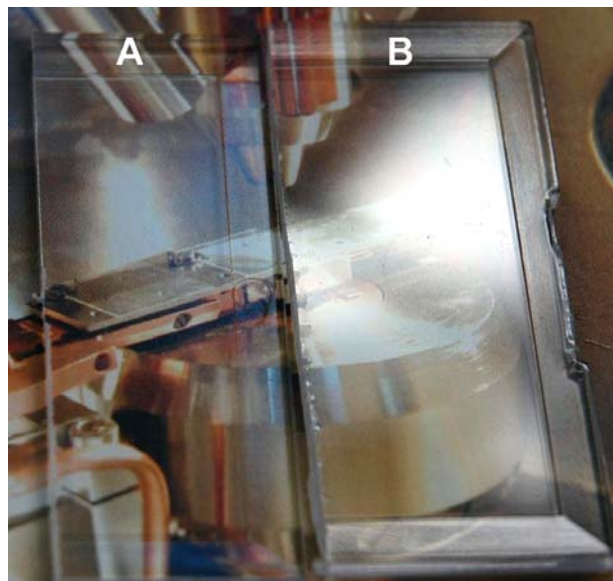


Figure 3.12 Photograph of PC substrates (A) with and (B) without AR coatings.

3.4 Experimental

3.4.1 Chemical and Materials

3-Amino(propyltrimethoxysilane) (APTS), nitric acid (HNO₃), ethanol (anhydrous, 98%), poly(allyaminehydrochloride), colloidal silica 30 wt.% suspension in water, and tetraethylorthosilicate (TEOS, 98%) were purchased from Sigma-Aldrich (St. Louise, MO). The chromatographic spray bottles were purchased from Fisher Scientific (Pittsburgh, PA). Deionized (DI) water (18 MΩ) was obtained using a Milli-Q water system.

3.4.2 Polycarbonate surface functionalization with APTS

Polycarbonate substrates were immersed in a 5% (by weight) solution of 3-amino(propyltrimethoxysilane) (APTS) in isopropanol for 2 hours. The sample was then rinsed with isopropanol, followed by DI water.

3.4.3 Sol-gel preparation

A sol-gel stock solution was prepared by mixing 40 mL of tetraethylorthosilicate (TEOS) with 38.7 mL of ethanol and 4 mL of DI water. 3 mL of 0.1 M HNO₃ was added slowly to the solution. The solution was then magnetically stirred for 1 hour and was left to age for 24 hours. The hydrolysis of TEOS leads to the formation of tetrahydroxyl silane.

3.4.4 Spin coating of the sol-gel solution

The sol-gel solution was spin-coated on the substrates using a spin coater purchased from Laurel Technology Cooperation. Different spin rates (1000, 2500, and 2750 rpm) were used to control the film thickness.

3.4.5 Layer-by-layer (spraying) deposition

Ultrathin poly(allylaminehydrochloride) (PAH)/silica nanoparticles nanoporous films were fabricated by an alternating deposition of PAH and silica nanoparticles by using a unique spraying technique. A 0.01 M solution of PAH with an adjusted pH of 6.8 and 0.1% (by weight) solution of silica nanoparticles with an adjusted pH of 6.8 were used to create the multilayer films. A constant flow of 120 psi (827.37 kPa) of nitrogen gas was used to spray the solutions with the chromatography spray bottles with a nozzle diameter of 1 mm. A layer of PAH was deposited on to the surface by spraying the PAH solution with two cycles of 3-sec spray/5-sec delay followed by another 3-sec spray and 10-sec delay. The substrate was then rinsed with DI water consisting of 2 cycles of 10-sec spray/5-sec delay. The silica nanoparticles were then applied following the same procedures as the PAH, and was then followed by another rinsing cycle. Such a procedure would generate a bi-layer of the AR coatings on the polycarbonate substrate.

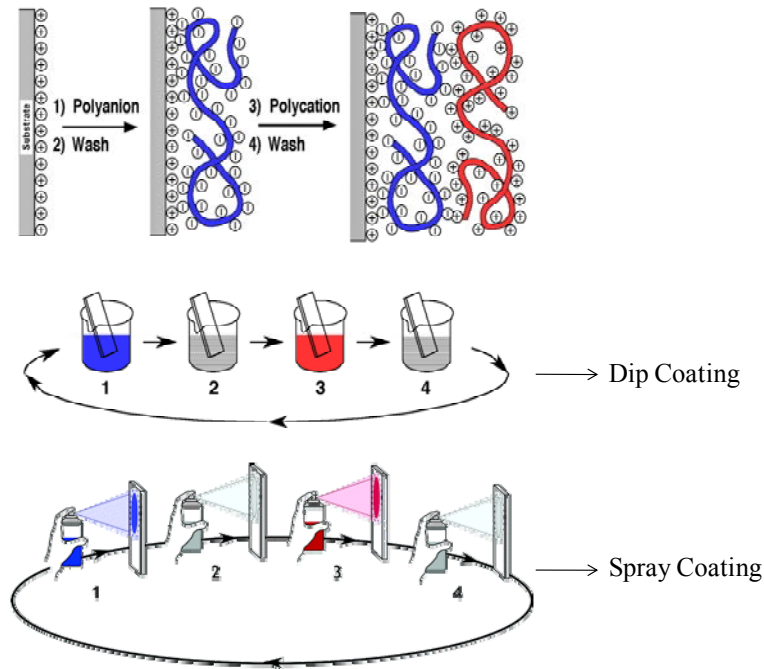


Figure 3.12 Layer by Layer self assembly of multilayer film by different methods.

3.4.6 Layer-by-layer (dipping) deposition

AR coatings were also fabricated via a dipping deposition to compare the AR properties with the AR properties of those fabricated *via* the spraying deposition. The polycarbonate substrate was first dipped into a cationic solution for 15 minutes followed, by one 2 minutes and two 1 minute rinsing steps using deionized water. Then, the substrate was dipped into an anionic solution for 15 minutes, followed by the same rinsing steps.

3.4.7 Characterization

The coating thickness and refractive index was obtained using a J. A. Woollam Visible Variable-Angle Spectroscopic Ellipsometer (V-VASE) (0.2–1.1 μm). The transmittance of the samples was measured using a Varian 300 UV-Visible Spectrometer. The absorbance of the polycarbonate substrate was measured to be about 0.05% from 400 to 700 nm using a Varian 300 UV-Visible Spectrometer. The reflectance of the samples is calculated by substrate transmittance and absorbance from 100. The water contact angle of the samples was measured using a Rame' Hart, Inc., Imaging System. The atomic-force microscope (AFM) images were obtained using a Dimension 3100.

3.5 Conclusion

In summary, abrasion-resistant AR coatings on polycarbonate substrate were fabricated using spraying layer-by-layer deposition of PAH/silica nanoparticles. The mechanical properties of the coatings were improved by the Functionalization of PC surface and sol-gel treatments. The resultant abrasion-resistant AR coatings are able to reduce the reflection from 5 to 0.3%. The reported technique provides a cost effective and versatile approach to fabricate conformal AR coatings on plastics with the potential of mass production.

CHAPTER 4 FABRICATION OF ULTRATHIN POLYELECTROLYTE FIBERS AND THEIR CONTROLLED RELEASE PROPERTIES

4.1 Abstract

Ultrathin fibers comprising 2 weak polyelectrolytes, poly(acrylic acid) (PAA) and poly(allylaminehydrochloride) (PAH) were fabricated using the electrospinning technique. Methylene blue (MB) was used as a model drug to evaluate the potential application of the fibers for drug delivery. The release of MB was controlled in a nonbuffered medium by changing the pH of the solution. The sustained release of MB in a phosphate buffered saline (PBS) solution was achieved by constructing perfluorosilane networks on the fiber surfaces as capping layers. Temperature controlled release of MB was obtained by depositing temperature sensitive PAA/poly(*N*-isopropylacrylamide) (PNIPAAm) multilayers onto the fiber surfaces. The controlled release of drugs from electrospun fibers has potential applications as drug carriers in biomedical science.

4.2 Introduction

Compared to traditional oral and needle delivery methods, sustained and controlled release drug delivery systems offer higher effectiveness due to the balanced mode of delivery, lower toxicity and improved patient convenience.¹⁹⁴ Various delivery systems including micelles of biodegradable block copolymers,¹⁹⁵⁻¹⁹⁷ hydrogels,¹⁹⁸⁻²⁰⁴ and nanoparticles²⁰⁵⁻²¹⁰ have been extensively investigated. Over the past decade, electrospun polymeric nanofibers have been used in the controlled release of proteins²¹¹⁻²¹⁴ and drugs,²¹⁵⁻²¹⁷ and healingwounds^{218, 219} due to their non-toxicity and high surface area to volume ratio. Electrospun polymeric fibers are fabricated by applying a high electrostatic field to a polymer solution held in a syringe with a needle. A jet is emitted from the cone-like meniscus (Taylor Cone) formed on the needle when the field

strength exceeds the critical value necessary to overcome the polymer solution surface tension. As the jet moves toward the collecting electrode, its diameter decreases due to lateral excursions, and the solvent evaporates, leading to a non-woven fabric mat on the collecting electrode.^{2, 220, 221} Charged polymers (polyelectrolytes) have been extensively investigated in fabricating electrospun fibers,²²²⁻²²⁵ and have great potential for controlled drug release. Due to the small size of electrospun fibers, conformal coatings responsive to external stimuli on the fiber surfaces can realize the controlled drug release.²²⁶ Among various film fabrication methods, the layer-by-layer (LBL) molecular-level adsorption of polymers is a well-established methodology for creating conformal thin film coatings with precisely tuned physical, biochemical and chemical properties.^{38, 157, 158, 160, 188} This technique involves the sequential adsorption of materials that are bound through intermolecular forces including electrostatic interactions,³⁸ hydrogen bonding,^{157, 158} and acid-base pairing.^{160, 188} The LBL technique provides a versatile platform for the assembly of materials and nanostructures of interest in the context of drug delivery. In fact, polyelectrolyte multilayer films have already demonstrated the capability of controlled drug release.^{58, 227, 228 229, 230} Polyelectrolyte multilayer films have also been extensively investigated for applications such as membranes to control the permeation of various ions,²³¹⁻²³³ and as capsules to control the release of drugs.²³⁴⁻²³⁸ It is obvious that the combination of the unique properties of polyelectrolyte electrospun fibers and polyelectrolyte multilayer films will lead to versatile controlled release systems.

Here, we present our research on fabricating fibers containing poly(acrylic acid) (PAA) and poly(allylaminehydrochloride) (PAH) using the electrospinning technique. The controlled release of low molecular weight cationic molecules is studied by using methylene blue (MB) as a model drug. The advantage of such weak polyelectrolyte fiber systems is that the drug release

can be controlled by the pH of the medium. Additionally, various functional coatings including perfluorosilane hydrophobic coatings and PAA/poly(*N*-isopropylacrylamide) (PNIPAAm) multilayer films can be deposited onto the fiber surfaces to achieve a controlled release.

4.3 Results and Discussion

4.3.1 Fiber fabrication

In order to electrospin fibers containing PAA and PAH, a homogenous mixture of these two oppositely charged polyelectrolytes is required. It is well known that mixing polyelectrolytes with opposite charges and similar molecular weight results in complexes that are not soluble in water due to the electrostatic interactions.²³⁹ Therefore, in order to make homogeneous mixtures of PAA and PAH, PAA has to be completely protonated to inhibit the electrostatic interaction between PAA and PAH. In our studies, a homogeneous PAA/PAH mixture was obtained by dissolving PAH into a 25% PAA aqueous solution with 2:1 molar ratio (by repeating unit) of PAA and PAH while keeping the pH of the mixture around pH 2.1. PAA and PAH are weak polyelectrolytes with pK_a values of 6.4 and 8.7 in aqueous solutions, respectively.²⁴⁰ At pH 2.1, although PAH is fully positively charged, PAA is almost completely protonated and neutral. Therefore, very little electrostatic interaction is present between PAA and PAH, resulting in a homogeneous PAA/PAH mixture. In contrast, when the pH of these mixtures were increased to pH 2.5, insoluble precipitates formed due to the ionization of PAA which resulted in electrostatic interaction between PAA and PAH.²⁴¹

PAA/PAH fibers were obtained by electrospinning homogenous PAA/PAH mixtures with various molar ratios of PAA and PAH. Our attempt to spin fibers from a 1:1 PAA/PAH mixture was not successful due to high conductivity of the solution, while electrospinning PAA/PAH

mixtures with PAA/PAH ratios of 2, 4 and 8 led to uniform fibers. Figure 4.1 shows a scanning electron microscopy (SEM) image of electrospun fibers from a 2:1 PAA/PAH mixture. The resultant fibers showed uniform cylindrical structures with an average diameter of approximately 300 nm. The solubility of uncrosslinked PAA/PAH fibers was studied by examining the fiber structure after immersion in DI water overnight. The fibers spun from the 2:1 and 4:1 PAA/PAH mixtures did not show any structural change. We believe that although the PAA/PAH fibers were spun from mixtures with $\text{pH} \sim 2.1$ at which very few electrostatic interactions were present, some of the acid groups in PAA were ionized when the fibers were exposed to the higher pH of DI water ($\text{pH} \sim 5.5$). The resultant carboxylate groups form electrostatic bonds with fully charged PAH, leading to insoluble fibers. On the other hand, the fibers obtained from the 8:1 PAA/PAH mixture was partially soluble possibly due to the excess PAA presented in the fibers. We also found that all uncrosslinked fibers were completely soluble in a phosphate buffered saline (PBS) solution due to the charge shielding caused by the ions in the buffer. Hence, all fibers were thermally crosslinked at 140°C overnight to make them insoluble in PBS solutions.²⁴²

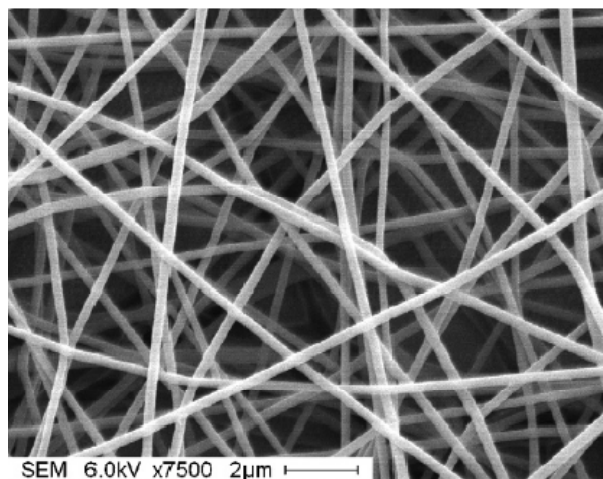


Figure 4.1 SEM image of PAA/PAH fibers electrospun from a 2:1 PAA/PAH (molar ratio) mixture.

4.3.2 Loading methylene blue

The rationale for PAA/PAH fibers holding positively charged drugs is that the negatively charged carboxylate groups in the fibers are able to bind with the positively charged drugs, and release them under controlled conditions. PAA is a weak polyelectrolyte with $pK_a \sim 6.4$, and its degree of ionization depends on the pH of the solution.^{241 240} Therefore, it is possible to control the release of positively charged drugs from the fibers by tuning the solution pH. In order to load positively charged drugs into PAA/PAH fibers, carboxylate groups are required. However, we mentioned previously that the PAA/PAH fibers were electrospun from the mixture at $pH \sim 2.1$, a pH at which PAA was completely protonated, and very few carboxylate groups were present in the fibers. In our studies, the carboxylate groups were generated by treating the fibers with a 0.05M NaOH aqueous solution. Figure 4.2 shows the FTIR spectra of the uncrosslinked (A), the crosslinked (B) and NaOH treated crosslinked fibers (C). It is obvious that the absorption peak at 1700 cm^{-1} , assigned to the C=O stretching of the carboxylic acid (COOH) groups in the uncrosslinked fibers, decreases after the fiber was crosslinked. It suggests the formation of the amide bond between acid groups in PAA and ammonium groups in PAH. It is further proved by the appearance of the peak at 1691 cm^{-1} attributed to the C=O stretching of the amide (CONH) group. After the fibers are treated with a 0.05M NaOH aqueous solution, a peak at 1542 cm^{-1} appears, indicating the asymmetric stretching band of the ionized carboxylate (COO⁻) group. At the same time, the peak at 1700 cm^{-1} disappears completely, suggesting that all acid groups are ionized, providing an abundance of carboxylate groups (negatively charged) to bind with methylene blue (positively charged) through electrostatic interactions.

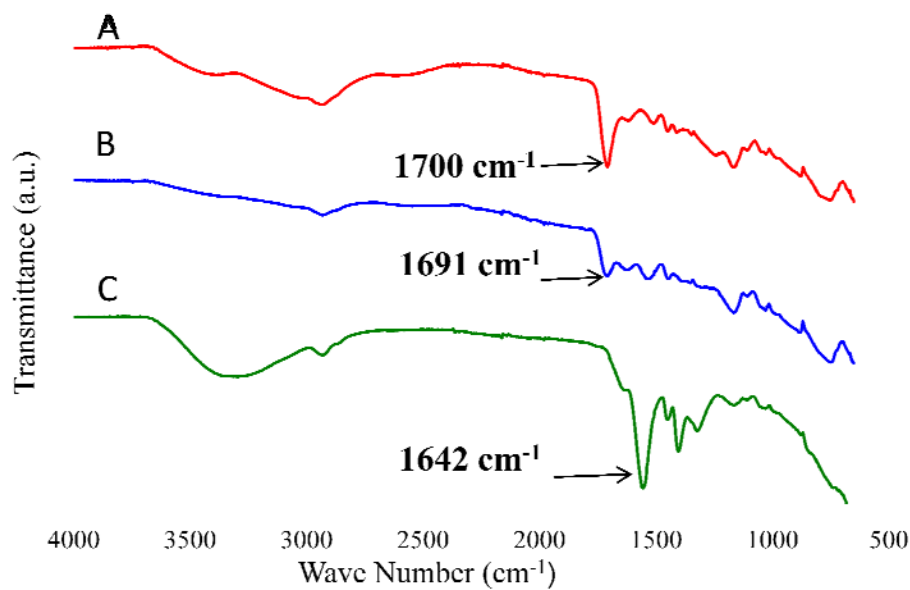


Figure 4.2 FTIR spectra of uncrosslinked (A), the crosslinked (B) and NaOH treated crosslinked PAA/PAH fibers (C). The absorption peaks at 1700 cm^{-1} , 1691 cm^{-1} , and 1542 cm^{-1} are assigned to the C O stretching of carboxylic acid (COOH) group, the amide (CONH) group and the ionized carboxylate (COO⁻) group, respectively.

4.3.3 Release of MB under nonbuffered conditions

The release profile of MB was examined using nonbuffered aqueous solutions with various pH. As mentioned earlier, MB was loaded in the PAA/PAH fibers with PAA been mostly ionized. We anticipated that, by immersing the MB loaded fibers into a solution with lower pH, the carboxylate groups would be protonated, and the MB bound with these carboxylate groups would be replaced by protons, and release into the medium. Additionally, since PAA is a weak polyelectrolyte and its degree of ionization depends on the pH of the solution, the release of MB from PAA/PAH could be controlled by changing the solution pH. The release profile of MB loaded fiber in deionized water (pH~ 5.5) was first investigated (Figure 4.4). The release was monitored by tracking MB's absorbance peak at about 664 nm.^{243, 244} It is obvious that, as some the carboxylate groups of PAA were protonated at pH~ 5.5, MB detached from the PAA and

diffused out of the fibers into the solution medium. The MB release characteristic was investigated using the monolithic model where MB is dispersed uniformly throughout the fibers.²⁴⁵ The release profile consisted of two sequential diffusion stages. The first release stage ($t < 40$ min) follows the Fickian mechanism as shown in equation 4.1:

$$\left(\frac{M_t}{M_\infty}\right) = 4 \sqrt{\frac{Dt}{\pi r^2}} \text{ -----} \quad \text{Equation 4.1}$$

Where, M_t and M_∞ are the accumulative and maximal amounts of drug released, respectively, t is the release time. D is the diffusion coefficient of the drug in the fibers and r is the radius of the fibers.²⁴⁵ The diffusion coefficient found for MB diffusing through PAA/PAH fibers (about 10–15 cm²/s) is similar to the values reported for the MB release from PAA/PAH multilayer films.²²⁷ In the second stage ($t > 40$ min), MB diffuses with a reduced rate probably due to the lower concentration of MB in fibers, and the elevated MB concentration in the solution. The pH controlled release of MB in nonbuffered aqueous solution was investigated by monitoring the MB absorbance with the change of the solution pH (pH = 10, 9, 8, 7, 6.5, 6, 5, 4, 3 and 2). The pH of the solution was tuned by adding a 0.02M HCl solution to the original pH 10 NaOH aqueous solution. According to previous reports,^{240, 246-248} PAA in the solution is around 95% ionized at pH 10, and the concentration of carboxylate groups decreases with decreasing solution pH. In our studies, MB was loaded in fibers at pH 10. Therefore, MB was expected to detach from carboxylate groups as solution pH dropped. It is interesting to note that no MB absorbance peak was observed in the pH range from 10 to 6.5, indicating no release of MB from the fibers. Such observation suggests that the dissociation behavior of PAA in PAA/PAH fibers is different from that in solutions. In the PAA/PAH fibers, PAA is mixed with PAH, which is similar to the composition of PAA/PAH multilayer films. Therefore, the pKa of PAA shifts to a lower value

due to the presence of PAH.²⁴⁷ When the MB loaded fibers were immersed in solutions with pH values ranging from 10 to 7, PAA is fully charged, and the negatively charged carboxylate groups remain bound with the positively charged MB molecules to prevent MB from releasing. However, as solution pH decreases to 6, protons in solution combine with carboxylate groups to replace the bound MB, resulting in the release of MB. As shown in Figure 4.5, the fibers start releasing MB at pH 6 and continue releasing for 10 hours until it reaches equilibrium. After reaching the plateau at pH 6, the fibers were still quite blue, suggesting that some MB was still bound with remaining carboxylate groups. When the pH of the solution was lowered further to pH~5, MB started to release, and continued until it reached another equilibrium value. At pH 2, most of the carboxylate groups were protonated and released most of the pre-bound MB. Such pH controlled release will be important for the discussion below where polyelectrolyte multilayers had to be deposited while keeping MB inside the fibers. The release rate of MB in different pH solutions was examined by immersing five identical MB loaded fiber mats into solutions with pH of 6, 5, 4, 3, and 2. The absorbance of MB in each solution was monitored with time. Figure 4.5 shows the MB release profile with time at different pH. It is obvious that the fibers have higher initial release rate in solutions with lower pH, and take shorter time to reach the equilibrium. In the solution with low pH, more protons are available to replace the MB bound with the carboxylate groups in fibers, leading to a faster release of MB. This result is consistent with the study on loading and releasing low molecular weight cationic molecules in polyelectrolyte multilayer films where the rate of release of the dye from the multilayer increased with decreasing pH.²²⁷ It is worth to note that the equilibrium MB concentration for identical MB loaded PAA/PAH mats are different at different pH, suggesting that the fibers release different amount of MB at different pH. The loaded MB is released completely only in the solution with

pH~ 2 whereas certain amount of MB remains in the fibers in solutions with higher pH. This result further indicates that the releasing of MB can be controlled by pH in nonbuffered solutions.

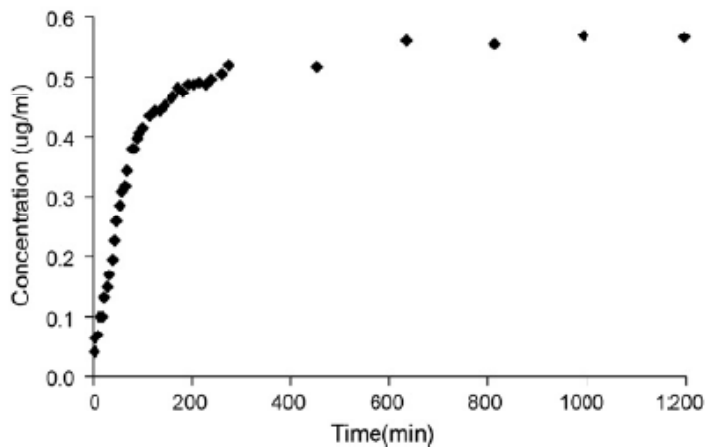


Figure 4.3 Release of MB from crosslinked PAA/PAH fibers in water (pH~5.5).

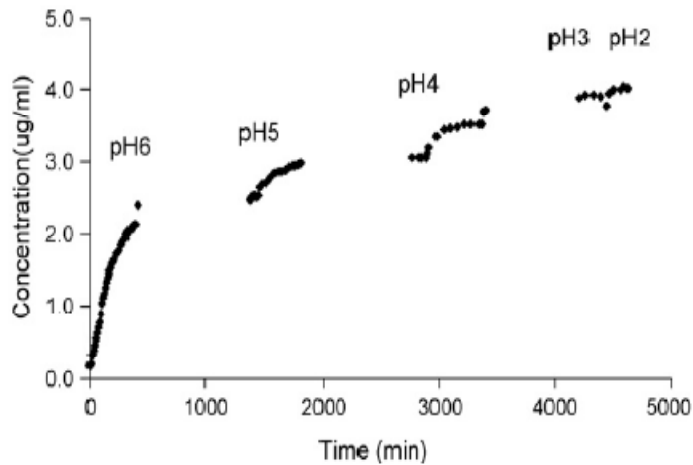


Figure 4.4 Release profile of MB in aqueous solutions with different pH (The release is controlled by changing the solution pH).

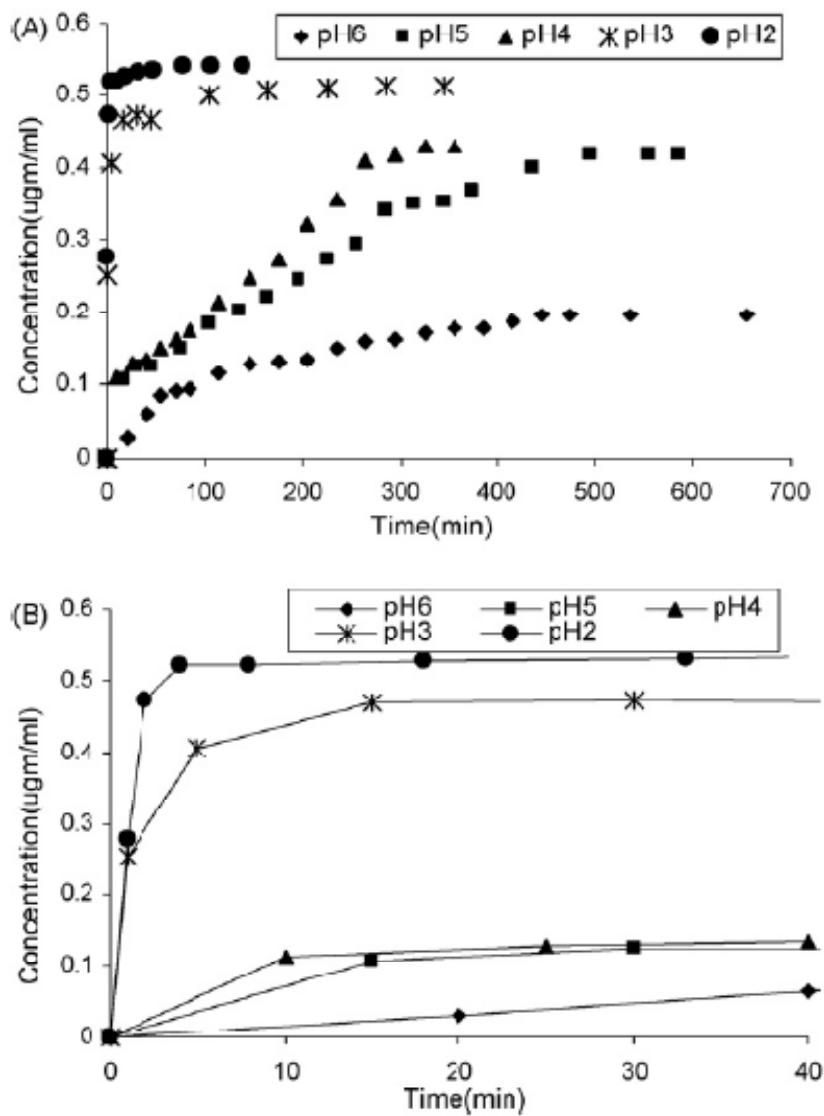


Figure 4.5 Release profile of MB in nonbuffered aqueous solutions of different pH (A); (B) the releasing profile of MB in first 40 min.

4.3.4 Sustained MB release in a PBS solution

Our study in the controlled release of MB from PAA/PAH fibers in phosphate buffered saline (PBS) solutions is focused on sustaining the release of MB by manipulating the fiber surfaces. It was reported that the release of MB from PAA/PAH multilayer films was fast due to the charge shielding and swelling of the film which accelerated the releasing.²²⁷ Although PAA/PAH

capping layers were deposited on the film, they were not able to slow down the diffusion of MB due to the swelling caused by PBS.²²⁷ We observed the similar fast releasing of MB from PAA/PAH fibers in PBS. As shown in Figure 4.6A, all loaded MB was released into the PBS solution within 10 minutes. Based on the aforementioned reasons for the fast release of MB in PBS, we assume that the diffusion of MB from the fibers can be hindered by covering the fiber surfaces with a network structure that will not swell in the PBS solution. A hydrophobic perfluorosilane network²⁴⁹ is a good candidate for such an application. A perfluorosilane network was coated on MB loaded fibers via chemical vapor deposition of trichloro (1H, 1H, 2H, 2H-perfluorooctyl) silane (perfluorosilane) onto the fiber surfaces. During the subsequent heat treatment, perfluorosilanes form siloxane bonds among themselves, and result in a hydrophobic network¹⁶² which can hinder the diffusion of the MB. As shown in Figure 4.6 B, the MB release characteristics does not follow the Fickian mechanism due to the hydrophobic coatings, and the fluorosilane coatings elongate the MB release time in PBS up to more than 1000 minutes. This result supports our hypothesis that molecular network on the fibers will obstruct the diffusion of MB, and sustain the release.

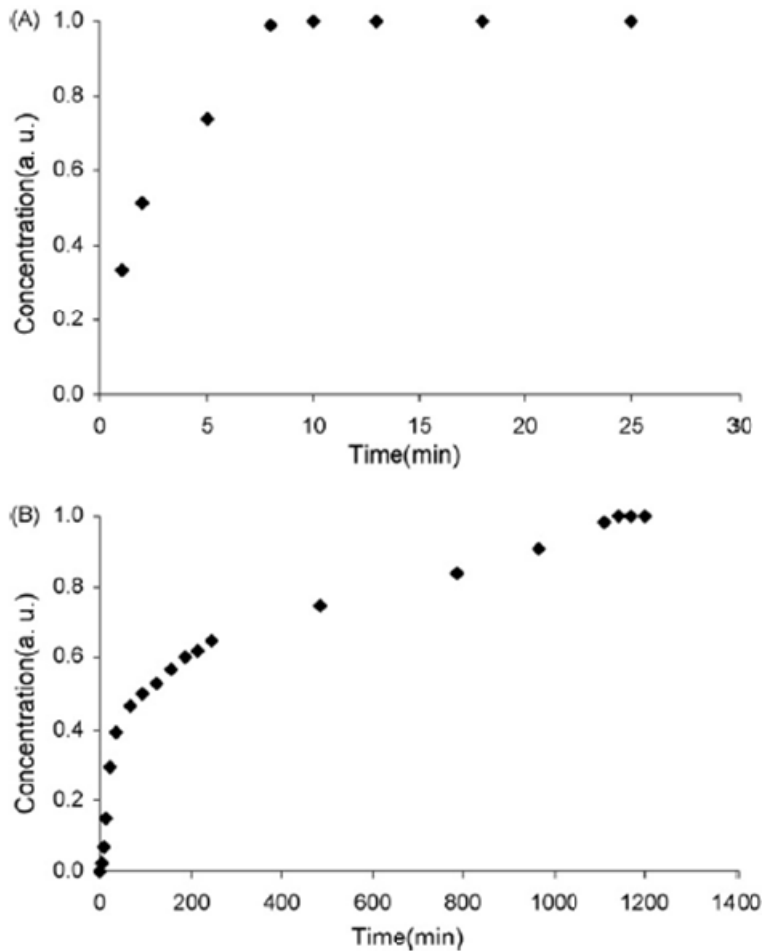


Figure 4.6 Release profile of MB from bare PAA/PAH fibers (A) and perfluorosilane coated PAA/PAH fibers (B) in PBS at pH 7.4. The release time of B is 100 times longer than that of A.

4.3.5 Temperature controlled MB release in a PBS solution

A temperature-controlled release of MB was achieved by coating the PAA/PAH fibers with multilayers of poly(acrylic acid) (PAA) and poly(*N*-isopropylacrylamide) (PNIPAAM) at pH 6.5. PNIPAAM is a thermoresponsive polymer which exhibits its lower critical solution temperature (LCST) in an aqueous solution and shows a sharp phase transition at ~ 32 °C.^{169-171, 250} PNIPAAM is soluble in water below its LCST (~ 32 °C), while at temperatures above its LCST, it forms intramolecular hydrogen bonds and becomes insoluble. Therefore, PAA/PNIPAAM multilayers on the fiber will not only sustain the release of MB, but also allow a

controlled release by changing the temperature. The PAA/PNIPAAm multilayer was assembled on MB loaded fibers at pH 6.5 using the layer-by-layer assembly technique. PAA in an aqueous solution is partially protonated at pH~6.5, and forms intermolecular hydrogen bond with PNIPAAm. In contrast, PAA in the PAA/PAH fibers are fully charged at pH 6.5 due to the lower p*K*_a value of PAA in fibers. Therefore, MB in the fibers is not released during the multilayer deposition. When the MB loaded fibers were immersed in the pH 6.5 PNIPAAm solution, their amide groups form hydrogen bonds with PNIPAAm. A hydrogen bonding multilayer will form with subsequent deposition of PAA and PNIPAAm. Such hydrogen bonding multilayer films form a knit structure covering the surface of the MB loaded fibers to hinder the diffusion of MB.

The release of MB in PBS solutions from the PAA/PAH fibers coated with PAA/PNIPAAm multilayers was studied at room temperature (~25 °C) and elevated temperature (40 °C) (Figure 4.7). At room temperature (~ 25 °C), it takes much longer for the PAA/PNIPAAm multilayer coated fibers to release all loaded MB than bare fibers (Figure 4.7A). The sustained releasing is due to the hydrogen bonded network on the coated fibers which delays the diffusion of MB. On the other hand, the coated fibers release MB much faster at the temperature above PNIPAAm's LCST. As shown in Figure 4.7 B, the release of MB takes 50 min. We believe that PNIPAAm forms intramolecular hydrogen bond above LCST, which disrupts the PAA/PNIPAAm hydrogen bond network, leading to an accelerated diffusion of MB. The effect of coating thickness on release rate was also investigated by comparing MB releasing rate of fibers coated with 11, 21 and 31 layers of PAA/PNIPAAm. It is apparent that fibers with thicker PAA/PNIPAAm coatings release MB slower at both room temperature and elevated temperature (Figure 4.7). This is due to the longer diffusion path associated with thicker coatings. For example, at 25 °C,

the MB diffusion coefficient of the fibers coated with 11 layers of PAA/PNIPAAM is 10 times larger than that of the fibers coated with 31 layers of PAA/PNIPAAM.

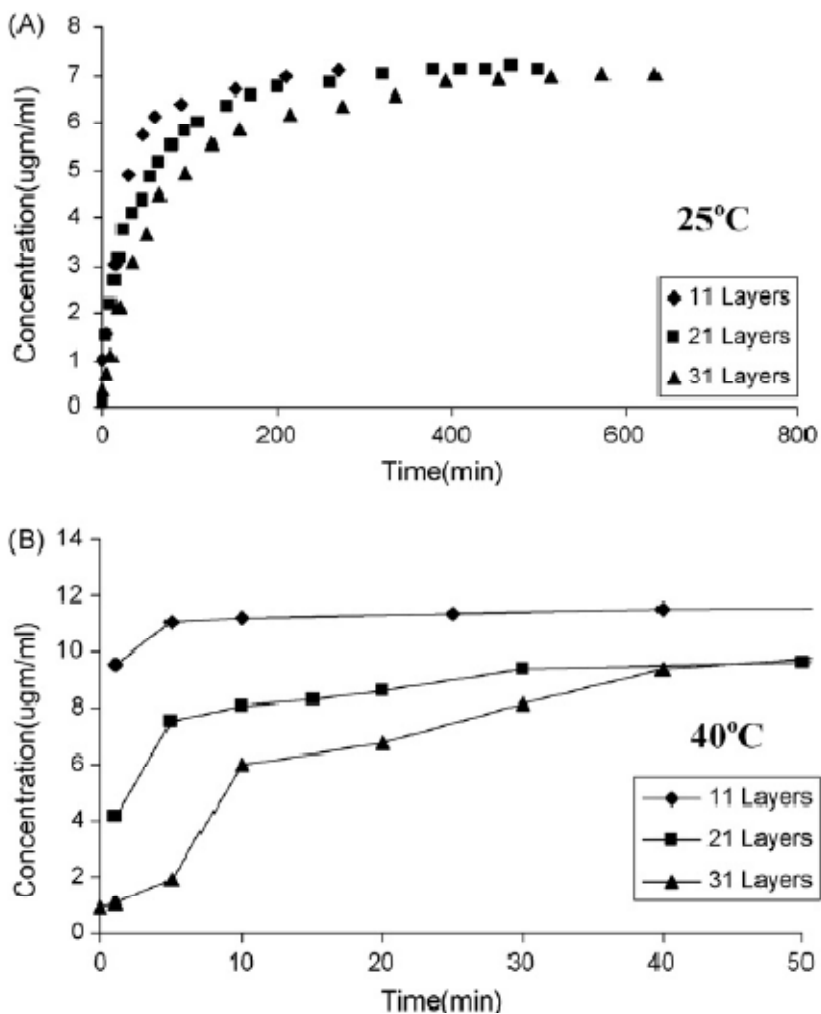


Figure 4.7 The releasing profile of MB from fibers coated with 11, 21 and 31 layers of PAA/PNIPAAM multilayers at room temperature $\sim 25^{\circ}\text{C}$ (A) and 40°C (B) in PBS.

4.4 Experimental

4.4.1 Materials and chemicals

Polyallylamine hydrochloride (PAH, $MW \sim 70000$), poly(*N*-isopropylacrylamide) (PNIPAAM), trichloro(1H, 1H, 2H, 2H-perfluorooctyl) silane, indium tin oxide coated polyethylene sheet and

methylene blue (MB) were purchased from Sigma Aldrich, Inc. (St. Louis, MO). Poly(acrylic acid) (PAA, $MW \sim 90000$) was obtained from Polysciences, Inc. (Warrington, PA). All chemicals were used as received. The aqueous solutions were prepared with purified water with the resistivity of $18.2M\Omega\text{cm}$ (Millipore Milli-Q plus water purification system, Billerica, MA). The chemical structures of the polyelectrolytes, PNIPAAm and MB are shown in Figure 4.8.

4.4.2 Fabrication of fibers

Polymeric thin fibers were fabricated from a homogenous mixture of poly(acrylic acid) (PAA) (25% solution in water) and poly(allylaminehydrochloride) (PAH) (solid) using the electrospinning technique. The molar ratios between PAA and PAH was 2. The polymer solution was fed in a syringe attached with a syringe pump and a potential supply (Glassman High voltage, Inc.). Fibers were spun using a potential supply of 10 kV with 20 cm distance from the syringe to the collecting electrode (an indium tin oxide coated polyethylene sheet).

4.4.3 Loading methylene blue in fibers

Methylene blue (MB) (a cationic molecule) was used as the model drug for drug loading and releasing studies. In order to load MB into the fibers, the fibers were crosslinked at $140\text{ }^{\circ}\text{C}$ overnight and immersed into a 0.05M NaOH solution for 15 min. The fiber mesh was dried and immersed in a nonbuffered (pH 10) 1% MB solution for 1 hour. Loosely bound MB was removed by rinsing the fibers with a pH 10 NaOH aqueous solution. The MB loaded crosslinked fibers were dried with nitrogen.

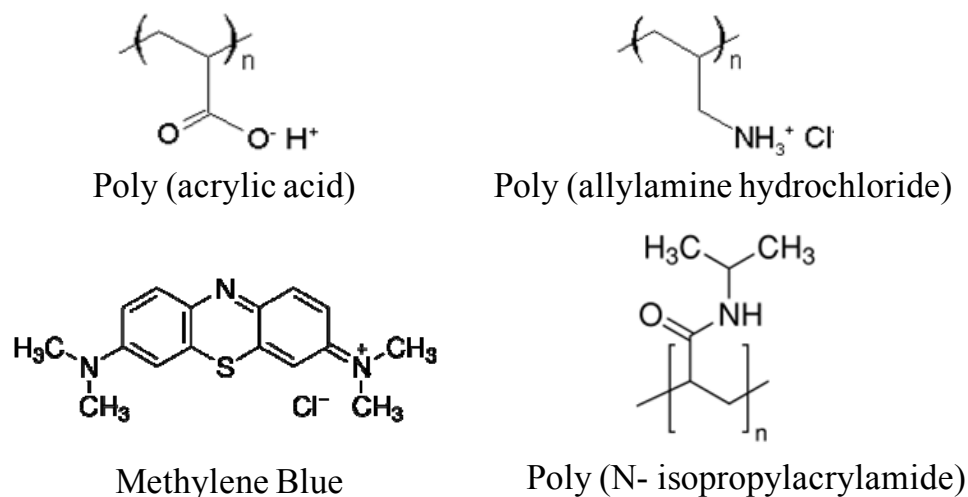


Figure 4.8 Structures of the chemicals used in the study.

4.4.4 Assembly of poly(acrylic acid)/poly(N-isopropylacrylamide) (PAA/PNIPAAm) multilayers on PAA/PAH fibers

Multilayer films were prepared by alternating deposition of PAA and PNIPAAm onto the MB loaded fibers. The concentration of both polymers was 0.01 M, and the pH was adjusted to 6.5 using a 0.1M NaOH aqueous solution. The fibers were first immersed into the PNIPAAm solution for 15 min, followed by rinsing in three separate baths of pH 6.5 water for 2, 1, and 1 min. The fibers were then immersed into the PAA solution for 15 min followed by the same rinse cycle. The process was repeated to obtain 11, 21 and 31 layer films with PNIPAAm on the top.

4.4.5 Measurement method

The morphology of the electrospun fibers was studied using a JEOL scanning electron microscope (SEM). The release of MB was investigated by monitoring the absorption of MB in solutions using a Cary 300 Bio UV-Vis spectrophotometer. The chemical composition of polyelectrolyte fibers was examined using a Perkin-Elmer Spectrum 100 FTIR Spectrometer.

4.5 Conclusion

Ultrathin fibers comprising two oppositely charged weak polyelectrolytes PAA/PAH were fabricated using electrospinning. These fibers are capable of controlling MB releasing through pH changes. The releasing properties of PAA/PAH fibers was tuned by depositing different coatings onto fiber surfaces. A sustained and a temperature controlled MB releasing in PBS solutions was achieved by depositing perfluorosilane coatings and PAA/PNIPAAm multilayers onto the fiber surfaces, respectively. These polyelectrolyte fibers, due to their simple fabrication and the controlled release property, can be used for drug delivery devices and in other potential application fields.

CHAPTER 5 EFFECT OF SURFACTANT ON SUSTAINED RELEASE OF DRUG FROM SUPERHYDROPHOBIC NANOFIBER

5.1 Abstract

Wetting of hydrophobic and superhydrophobic solid surfaces with water and different other solutions have always been a subject of interest from the practical and theoretical aspects. Wetting with water solely depends on the interfacial energy of the interfaces involved in the phenomenon, but for surfactant solutions, the wetting is caused by the transfer of surfactant molecules on the solid surface in front of the liquid droplet on the three phase contact line. In the current research, drug loaded superhydrophobic nanofiber mat was immersed under water, phosphate buffer saline and surfactant solutions to monitor the rate of release of drugs from the fiber surface as a result of wetting. The effect of surfactant type and concentration on wetting was studied and analyzed by contact angle measurement. Time dependent wetting of the superhydrophobic surface with different concentrations of surfactant solutions provided important information about the retention time of drug in the fibers.

5.2 Introduction

Considerable effort has been put to design and manipulate superhydrophobic surfaces since they offer attractive properties like easy drop transport and self cleaning in various fields²⁵¹⁻²⁵³ such as microfluidics, satellite dishes, windshield of automobiles, eye glasses, roofing etc. In applications where reduced wettability and adhesion is desired, superhydrophobic surfaces play an important role as they provide very small contact area between the liquid and the solid surface. The fabrication and function of such surfaces are based on surface energy, surface roughness and homogeneity which control the wetting of the solid. Surfaces with high roughness and low surface energy has been found to show maximum water repellency or

superhydrophobicity.²⁵⁴ In the present research, drug embedded nanofibers were spun from the mixture of two polyelectrolytes and drug solution by electrospinning. Then the fiber surface was made superhydrophobic, where the roughness was created by silica nanoparticle and low surface energy was achieved by chemical vapor deposition of trichloro (1H, 1H, 2H, 2H-perfluorooctyl) silane (perfluorosilane) - a low surface energy compound. The fiber surface was immersed in water, PBS buffer and different solutions of surfactants to check the underwater superhydrophobicity. The surface was checked for its wetting after certain intervals to study the time dependent wettability of the superhydrophobic surface with various solutions. Simultaneously, the release of drug from the surface was also monitored as the initial release phenomena were dependent on the wetting of the surface. The effect of surfactant on the wetting and consequently on the release of drug was studied with increased surfactant concentration solutions. The release of drug was found to be sustained due to the superhydrophobic coating on the fiber surface. The effect of surfactant on the sustained release of drug from superhydrophobic fibers has not been reported to the best of our knowledge. The system may have potential application in controlled release devices.

Controlled release of model drug methylene blue (MB) from PAA/PAH fibers in deionized (DI) water was achieved by adjusting pH of the medium whereas the same in PBS buffer was accomplished by capping the fiber surface with hydrophobic material or temperature sensitive multilayer films as reported in the previous chapter.¹²⁵ Otherwise, the release of the drug from the fiber was very fast in PBS buffer compared to that of in non buffered deionized water.¹²⁵ All loaded MB was released into the PBS solution within 10 minutes whereas the release took several hours in DI water under normal condition. It was reported that the release of MB from PAA/PAH multilayer films was fast due to the charge shielding and swelling of the film which

accelerated the releasing.²²⁷ Therefore a perfluorosilane network was coated on MB loaded fibers via chemical vapor deposition of trichloro (1H, 1H, 2H, 2H perfluorooctyl) silane (perfluorosilane) onto the fiber surfaces. During the subsequent heat treatment, perfluorosilanes formed siloxane bonds among themselves, and result in a hydrophobic network¹⁶² which hindered the diffusion of the MB. The fluorosilane coatings elongated the MB release time in PBS buffer up to more than 1000 minutes. However, the surface of the fluorosilane coated fiber was only hydrophobic and the cationic model drug methylene blue was prone to be replaced with the several cations present in PBS buffer, which left reasons to assume that if the surface could be made superhydrophobic and drug be neutral in nature, the release time of the drug would have been much longer. The presented research on sustained release of a neutral drug was based on its release from superhydrophobic fiber in PBS buffer and in aqueous solution of surfactants to study the effect of surfactant on the release profile.^{255, 256}

Surfaces with low surface energy and high roughness shows water contact angle of larger than 150° and are called superhydrophobic. On such surfaces water droplet sits like a ball with minimum contact with the solid surface. Therefore, when drug loaded superhydrophobic fiber is immersed in water or in PBS buffer, the surface of the fiber does not get wet readily and the release time of drug is elongated due to dewetting of the surface. Nevertheless, PBS buffer due to its high ionic concentration, tend to swell the network by charge shielding and shows faster release profile as compared to water. Additionally, the experiment conducted with aqueous solution of an anionic surfactant sodium dodecyl sulphate (SDS) of various concentrations, showed that the release of drug was faster as compared to the surfactant free medium. Also, with the increased percentage of the surfactant in the medium, the retention time of the drug in the fiber decreased. Retention time of the drug in the fiber is defined by the time up to which there is

no drug released in the medium after the fiber is immersed. It is important to note that for this particular study, a real life neutral drug (2, 3-tert butyl-4-methoxyphenol) was selected instead of cationic model drug methylene blue. The loading of methylene blue in PAA/PAH fiber was completely dominated by electrostatic interactions and therefore the loading and release of the drug was dependent on the ionic concentration of the medium as discussed in the previous chapter. In the reported studies, MB was replaced with a neutral drug to rule out the possibility of any kind of cation-anion interaction that might influence the rate of release of the drug from the superhydrophobic fiber. A time dependent study was carried out to check the release profile of the hydrophobic neutral drug embedded in the fiber in DI water, in PBS buffer and in aqueous solution of surfactants of different concentrations.

5.3 Results and Discussion:

Silica nanoparticle decorated fiber surface acquired adequate micro and nano scale roughness and could entrap large volume of air in the pores of the rough surface. The microscale roughness originated from the irregularly coiled fibers with diameter in nanoscale and length in microscale, whereas the nanoscale roughness was due to the 7 nm sized silica nanoparticles deposited on the fiber surface as shown in the SEM picture. The fibers finally became superhydrophobic after being coated with the fluorinated polymer with low surface energy ($-\text{CF}_3$ group with surface energy of 6.7mJ/m^2), i.e. demonstrated de-wetting in pure DI water.

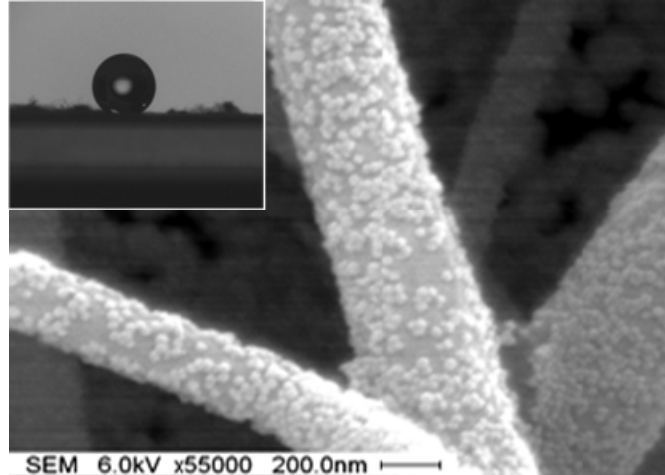


Figure 5.1 SEM image of the silica nanoparticle loaded superhydrophobic fiber. Inset is the contact angle of water droplet on the superhydrophobic fiber.

However, the scenario was different for PBS buffer which had high ionic concentration and different surface tension compared to DI water. The superhydrophobic fiber did not get wet after being immersed in water for a long time, but was found to get wet slowly in PBS buffer after a certain period of time. The drug loaded superhydrophobic fiber was immersed in PBS buffer to check the release profile of the drug. It was interesting to note that the release of drug was much slower from the superhydrophobic fiber surface than that of the normal crosslinked fiber at the beginning. Once the fiber surfaces got wet completely, there was a little difference in rate of release of drug between the superhydrophobic and the normal crosslinked fiber. Also, the rate of release of the neutral drug was small as compared to MB from normal crosslinked fiber in PBS buffer. PBS buffer had high concentration of cations which could replace MB and therefore influenced the rate of release, whereas, for the neutral drug the cation exchange effect was absent and so the release was slow.

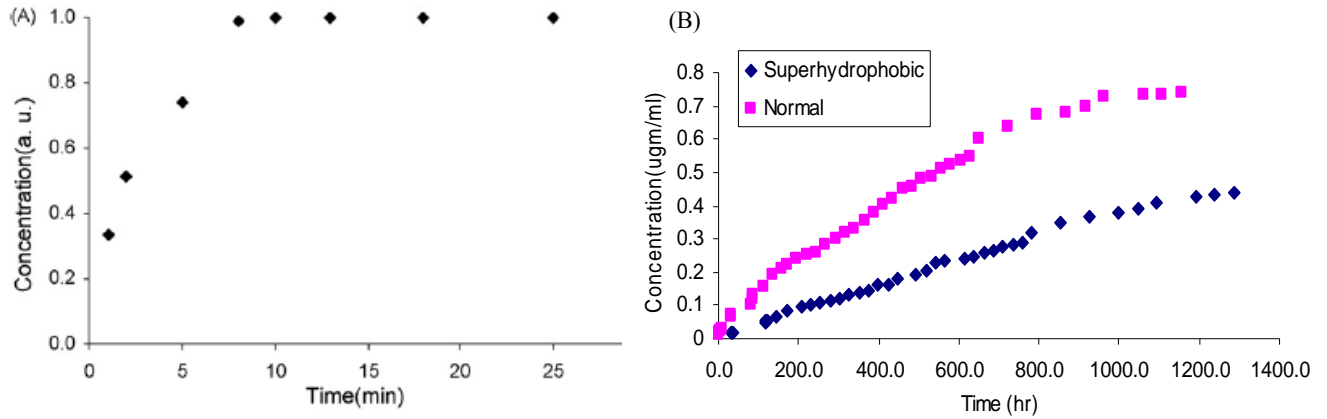
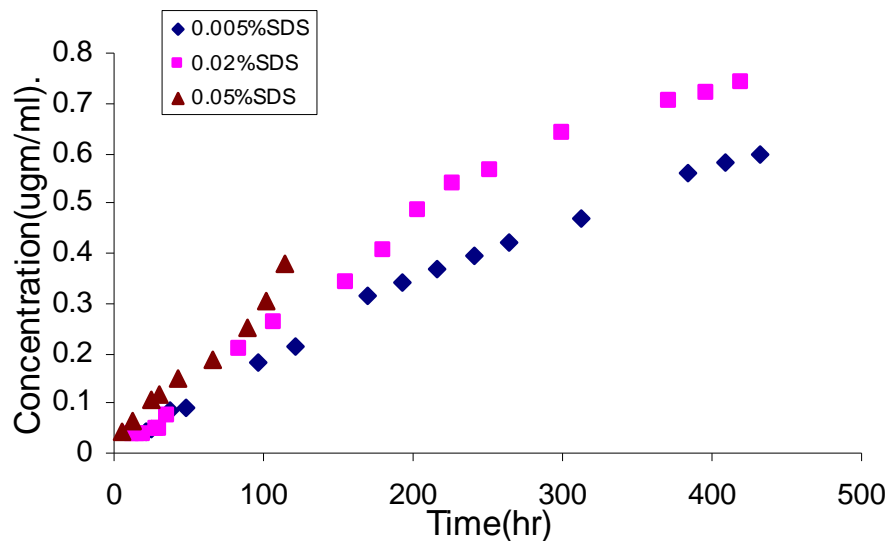


Figure 5.2 (A) Release profile of MB from normal crosslinked fiber in PBS buffer (B) release profile of neutral drug from superhydrophobic fiber and normal crosslinked fiber in PBS buffer solution.

The releasing of drug from superhydrophobic surface under the influence of surfactant was carried out in the surfactant solutions in DI water and not in their solution in PBS buffer. The reason was that the whole objective of the experiment was to study the effect of the surfactants on wetting of the surface and consequently diffusion of drug. PBS buffer contained lots of cations and anions and so could interfere with the experimental conditions. Figure 5.3 showed the release profile of the drug from superhydrophobic fibers in different surfactant solutions. The release was fast with high surfactant concentration in the medium. Nevertheless, retention time of the drug in the fibers became less with the increased concentration of surfactant in the medium. The release time was more than 1500 hours in 0.05%, 1000 hours in 0.02% and only 115 hours in 0.05% SDS solution. Figure 5.3 shows only the initial hours of study which clearly indicated that the rate of release was much faster in 0.05% SDS solution as compared to others. Once the fiber surface got wet completely, the rate of release became insensitive to surfactant concentrations.



Concentration of SDS in DI water(M)	Retention Time (hr)
0.00	33.00
1.73×10^{-4}	20.75
6.96×10^{-4}	12.50
1.73×10^{-3}	6.08

Figure 5.3 Release of neutral drug from superhydrophobic fiber in aqueous solution of SDS with different concentrations and the retention time of the drug in the fiber when immersed in different surfactant solutions (below).

5.3.1 Under water superhydrophobicity

In general, a liquid drop can spread over a solid and completely wet the surface. On the other hand, it may form a finite contact angle on the solid surface. If the contact angle is from 0° to 90°, the liquid partially wets the surface and if more than 150°, de-wetting or water repellency occurs and the surface is called superhydrophobic. When a liquid droplet sits on such surfaces,

always a layer of air exists in between the solid surface and the liquid. Therefore, the combination of a large fraction of air and a small fraction of fiber surface made the system superhydrophobic for pure DI water in this case. The effect of surfactant on the wetting behavior of superhydrophobic fiber surface was investigated because the release of the drug from the fiber depended on the wettability of the surface by the liquid medium in which the fiber was immersed. And wettability depended on the percentage of the solid in contact with the liquid on the composite surface, which was explained by the famous Cassie Baxter¹⁶⁸ model in equation 5.1 for superhydrophobic surfaces.

$$\cos \theta' = f_1 \cos \theta - f_2 \text{ -----} \quad \text{Equation 5.1}$$

In the above equation, f_1 was the fraction of liquid area in contact with the solid surface and f_2 , the fraction of liquid in contact with the trapped air. θ' and θ are the contact angle of liquid on smooth and rough surfaces respectively. In an ideal case, when a water droplet was placed on the superhydrophobic surface, a stable equilibrium state prevailed and the liquid-air surface existed on the tops of the roughness asperities.²⁵⁷ The curvature of the liquid-air interface inside the grooves was determined by the difference between the atmospheric pressure of the trapped air in the grooves and the pressure in the liquid drop. Since, the gravity of the liquid was neglected for a drop of water, the liquid-air interface was considered as flat for simplicity in this case and consequently, no liquid was assumed to penetrate the grooves on the rough surface. In our experiment, the fiber piece was immersed under water and was subjected to the force, $F = \rho hg$, where, ρ was the density of the water, h was height of the water pillar and g gravity. The force accounted for the hydrostatic pressure difference across the meniscus inside each roughness grooves and equaled to the order of magnitude of $2\sigma_l/R$, where σ_l was the air- liquid interfacial

tension and R was the mean radius of the curvature of meniscus. So, R could be calculated from the equation for a particular liquid pillar.²⁵⁷

For pure water, $R \approx 2\sigma_l/\rho hg \approx 10^{-5}/h$ m

For the case reported in my research, the height of the water pillar was about 2.0 cm for which R was $\sim 500\mu\text{m}$, which was much higher than that of the surface roughness of the superhydrophobic fiber. So, the surface did not get wet with water as well as with the surfactant solutions for a particular period of time and then slowly started get wetting. The wetting was due to the defects on surface through which water penetrated with elongated immersion time. The defect sites can be observed from the SEM image (Figure 5.1) where the silica nanoparticles did not cover the fiber surface completely and left empty spaces. In this case the situation deviated from ideality and the superhydrophobic surface was found to get wet with liquid after a period of time depending on the liquid surface tension. Therefore, f_1 approached to 1 according to the equation 5.1, which meant complete penetration of liquid through the roughness grooves, i.e. switching from Cassie¹⁶⁸ to Wenzel¹⁶⁶ model.

Surface wetting with water and surfactant solutions were measured in terms of the contact angle values on the fiber surface with different concentration of surfactant solutions (Figure 5.5). Results showed that the contact angle decreased on the fiber surface, when the concentration of surfactant in water increased. Our focus was only on the values of advancing contact angle. Surface wetting was different in case of pure DI water as compared to that of surfactant solution because the surfactant molecules tend to adsorb in the liquid-air and solid –liquid interface and change the interfacial tension and the wetting behavior. Surfactant adsorption altered the solid

surface energy and reduced surface tension which influenced the change in contact angle. The phenomena can be explained by the following equation 5.2²⁵⁸:

$$\sigma = \gamma S + PV + \pi R^2(\gamma_{s-l} - \gamma_{s-g}) \text{-----} \quad \text{Equation 5.2}$$

γ is air-liquid interfacial energy, S is the area of air-liquid interface, P is the excess pressure inside the liquid, R is the droplet base radius. According to the above equation, the excess free energy decreases if (a) the air-liquid interfacial tension decreases; (b) the solid-liquid interfacial tension decreases; and (c) the solid-air interfacial tension increases. In case of Cassie Baxter model, the air-liquid interface dominated because the liquid droplet sits on the trapped air in the roughness grooves. The surfactants start diffusing through the air-liquid interface and change the interfacial energy and results in wetting. However, the wetting of the superhydrophobic surface with surfactant depended on the architecture of the surfactant and its concentration.

5.3.2 Effect of the surfactant structure on wetting phenomena

Present research employed the anionic surfactant, SDS with a linear hydrophobic tail containing alkyl chain with sulphonic acid head group. The structure of the surfactant tail was important because the wettability of a particular surfactant depended on the architecture of its tail and also on its critical micelle concentration (CMC).²⁵⁵ As the surfactant concentration increased, contact angle dropped in the beginning, but even for the high concentration of 2xCMC, the contact angle was still more than 90° showing hydrophobic behavior. Figure 5.5 showed the change in contact angle with SDS concentration. CMC of SDS was 8x10⁻³ M and the red point indicated C_s > 2CMC . At concentration more than CMC, the interfacial tension of liquid-air (γ_{l-g}) was found to be insensitive to surfactant concentration. Additionally, increasing surfactant concentration caused transition from Cassie Baxter to Wenzel¹⁶⁶ regime for superhydrophobic surface.

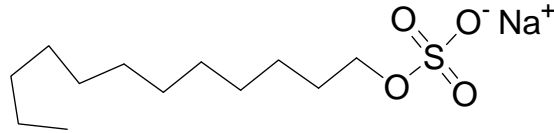


Figure 5.4 Structure of SDS.

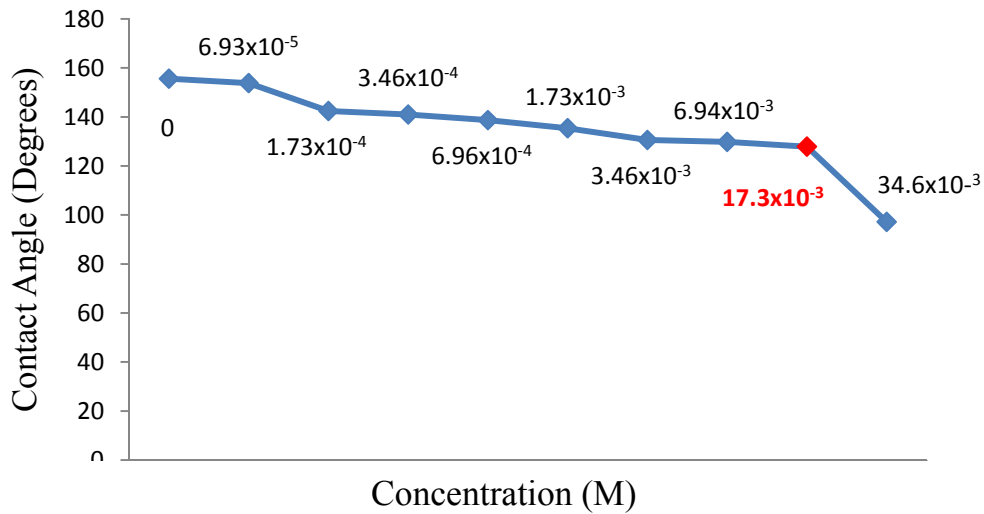


Figure 5.5 Change in contact angle with concentration of SDS. The red point indicates $C_s > 2CMC$.

The correlation between the surfactant concentration and the interfacial tension for some surfactants specially with linear tail structure could be explained by Gibbs adsorption equation (equation 5.3) which related surface excess concentration (Γ_s) to the interfacial tension(γ).

$$\Gamma_s = - \left(\frac{1}{k_B T} \right) \left(\frac{d\gamma}{d \ln C_s} \right) \text{-----} \quad \text{Equation 5.3}$$

Since, both γ_{l-g} and γ_{l-s} were unchanged, the surfactant monolayer was saturated in those interfaces, when $C_s \geq CMC$. Moreover, γ_{l-s} was saturated much before γ_{l-g} and so γ_{l-s} could not be reduced further to satisfy $\gamma_{l-s} < \gamma_{s-g}$ at saturation. Therefore, the surface remained

hydrophobic and the contact angle reduction was solely dominated by γ_{l-g} for surfactants like SDS.

5.3.3 *The time dependent wetting and the retention time*

However, exposure of the superhydrophobic surface to water or surfactant solution for a long time was found to cause partial wetting of the surface and release of the embedded drug from the fiber. The time dependent wetting of the surface was found as the function of surfactant concentration. The phenomena could be explained through time dependent diffusion and adsorption process of the surfactant molecules at the involved interfaces. The surfactant molecules diffused out of their aqueous solution and transferred on the hydrophobic surface in front of the moving liquid on the three phase contact line (TPC) line with time. The diffusion was assumed to take place through the air-liquid interface and was dependent on the concentration of the surfactant in the liquid droplet. Higher the concentration, more surfactant was supposed to move towards the interface to give maximum surface coverage and diffuse to get adsorbed to the surface. Maximum surface coverage was found to be achieved at CMC of the surfactant solution. The phenomenon was explained by a theoretical model suggested by Starve et al.²⁵⁸ According to that model the change in contact angle with the diffusion time scale²⁵⁹ was given as

$$\cos \theta_t = \cos \theta_0 + (\cos \theta_\infty - \cos \theta_0) \left[1 - \exp\left(-\frac{t}{\tau}\right) \right] \text{-----} \quad \text{Equation 5.4}$$

Where, $\cos \theta_\infty$ and $\cos \theta_0$ were the final and initial contact angles respectively and τ was the time scale of the transfer of surfactant molecules to the surface. According to this mechanism, when $C_s \leq \text{CMC}$, time scale for surfactant molecule transfer decreased with increased

concentration, which leveled off at CMC.²⁵⁹ This explained the decrease of retention time of drug in the hydrophobic fibers with increase in surfactant concentration (Figure 5.3).

5.4 Experimental:

5.4.1 Fabrication of drug loaded superhydrophobic fiber

A homogeneous mixture of PAA and PAH in the molar ratio of 2:1 was prepared and 500 μ l of 20% drug solution in DMF was mixed with the polymer. The polymer solution containing drug was electrospun to form nanofibers with embedded drug in it on an ITO coated polyethylene sheet. The fiber was then crosslinked with brief heating at 90 °C and was covered with silica nanoparticles by dipping in 0.01M PAH solution at pH 7.5 for 5 minutes and then in a 0.03% solution of silica nanoparticle (SM 30 Colloidal silica solution from Aldrich) for 15 minutes. The silica nanoparticle decorated fiber was then subjected to CVD with trichloro (1H, 1H, 2H, 2H-perfluorooctyl) silane and cured at 100 °C for an hr to render the surface superhydrophobic.

5.4.2 Measurement

The change in the wettabilities of superhydrophobic surfaces by surfactant solutions of different concentrations had been studied. The shapes of sessile drops on the superhydrophobic fiber surface were recorded at an elapsed time of 90 s and analyzed at room temperature on Goniometer. Reported values of contact angles were the average of five measurements under similar conditions. The release profile of the drug was studied with time using UV-Vis spectrophotometer. Small piece of fiber samples of equal size were immersed in 20 mL of DI water, 20 mL of PBS buffer and in 0.005%, 0.02% and 0.05% surfactant solutions in separate glass beakers. 3 mL of aliquot was taken each time to measure the absorption of the drug

molecules in the instrument after certain interval of time to check the release of drug. The opening of the beakers was tightly sealed with paraffin during storage so that the solution did not evaporate with time.

5.5 Conclusion

Sustained release of neutral drug from the superhydrophobic nanofibers in PBS buffer was explored. The results reported in the previous chapter about the release of MB from hydrophobic fiber in PBS buffer were compared to the release of neutral drug from the superhydrophobic fiber in the same buffer system. Release of drug from the superhydrophobic fiber was studied in water as a case of ‘under water superhydrophobicity’. Effect of surfactant on the wetting of superhydrophobic surface and resultantly on the release profile of drug was investigated. Advancing contact angle results showed when the concentration of the surfactant in water increased, contact angle decreased indicating surface wetting. The time dependent release and retention time of drug in the fiber was reported as a function of structure and concentration of surfactant. The advancing contact angle of solutions on the fiber surface decreases from 156° to 110° depending on the architecture and concentration of the surfactants in the solution.

CHAPTER 6 POLY(3-HEXYLTHIOPHENE) SUPRAMOLECULAR STRUCTURE ON REDUCED GRAPHENE OXIDE NANOSHEETS

6.1 Abstract

Poly(3-hexylthiophene) (P3HT) supramolecular structures are fabricated on P3HT-dispersed reduced graphene oxide (RGO) monolayers. P3HT is able to disperse RGO in hot anisole/N,N-dimethylformamide solvents, and forms nanowires on RGO surfaces through a RGO induced crystallization process. The TEM and AFM investigation of the resultant P3HT/RGO composites shows that P3HT nanowires grow from RGO, and connect individual RGO monolayers. Raman spectroscopy confirms the interaction between P3HT and RGO, which allows the manipulation of the RGO electrical properties. Such a bottom-up approach provides interesting graphene-based composites for nanometer-scale electronics.

6.2 Introduction

Reduced graphene oxide (RGO) nanosheets have emerged as inexpensive substitutes for graphene, which is difficult to obtain at the nanometer-scale in large quantities.^{32, 260} Chemically derived single-layered RGO sheets are produced by the chemical reduction of graphene oxide (GO) generated from the oxidation of pristine graphite using the Hummers' method.⁹⁷ The chemical reduction significantly increases the electrical conductivity of the insulating GO. Nevertheless, the practical application of RGO in electronics and composites is still limited by its poor dispersibility¹⁰² in solutions, especially organic solvents, and deficient electronic properties.²⁶¹ The poor dispersibility of RGO is a result of the removal of the hydrophilic groups during the chemical reduction of GO.^{103, 262} The dispersibility of RGO in aqueous suspension was improved by adjusting the pH of the aqueous suspension to increase the density of carboxylate groups on the RGO surface.¹⁰² To improve the RGO dispersibility in organic

solvents, GO functionalized with covalently bonded small organic molecules or stabilized with polymeric surfactants (non-covalent functionalization) are employed to produce RGO.^{103, 262, 263}

Although RGO nanosheets have a similar structure to graphene, the oxidation of graphite introduces point defects in the two-dimensional (2D) carbon framework after the reduction. The studies on chemically derived RGO indicate that an individual GO sheet comprises ordered pristine graphitic domains with a size of several nanometers surrounded by areas of oxidized carbon atoms or point defects.^{95, 264} After the chemical reduction, the oxygenated groups are partially reduced to re-establish the conjugated graphite network, and the vacant lattice sites formed by the carbon atom removal in the form of CO or CO₂ during oxidation remain unchanged. The graphitic domains are separated by insulating disordered domains in RGO, which leads to deteriorated electronic properties.^{95, 264} Electronic transport studies of single and multilayer RGO sheets suggest a partial regaining of the electrical conductivity, compared with the pristine graphene. In order to enhance the electrical properties of RGO, approaches that include optimizing reductive conditions,^{91, 102, 261, 265-267} molecular doping by various gases,²⁶⁸ electrochemical doping by gate voltage,²⁶⁹ and high temperature annealing²⁷⁰ have been investigated. Recent work on the interaction between large aromatic molecules and RGO suggests that large aromatic molecules can bind with RGO through π - π interactions.^{270, 271} Such noninvasive interactions not only allow the dispersion of RGO but also promise novel graphene composites with tunable electronic properties.²⁷⁰

Poly(3-hexylthiophene) (P3HT) is a conductive polymer widely used in electronic devices including field-effect transistors (FETs) and organic photovoltaics (OPVs) owing to its high charge mobility.²⁷²⁻²⁷⁴ It has been used to disperse carbon nanotubes (CNTs), conceptualized as a seamless cylinder by wrapping a layer of graphene, through π - π interactions.^{275, 276} Our previous

study also shows that ordered P3HT nanowires can form on CNT surfaces through a CNT induced crystallization of P3HT.²⁷⁷ Since the graphitic domains on RGO have similar structures to CNTs, it is expected that P3HT can interact with these graphitic domains and manipulate the dispersibility and electronic properties of RGO. The resultant P3HT/RGO composites are interesting materials for application in nanometer-scale electronics. In this communication, we report the fabrication of P3HT/RGO supramolecular composites and demonstrate the improvement of RGO dispersibility in organic solvents. The hierarchical 2D supramolecular structures with ordered P3HT nanowires on RGO surfaces are characterized and the RGO-induced P3HT crystallization process is investigated.

6.3 Results and Discussion

Graphite oxide (GO) is hydrophilic and readily dispersed in water and DMF as monolayers, because of the large amount of hydroxyl, carboxylic, carbonyl, and epoxies functional groups on its surface generated by oxidation (Figure 6.5).¹⁰⁰ However, because of the removal of the surface functional groups, the reduction of GO results in RGO agglomeration and precipitation in DMF. Based on our previous research on dispersing CNTs using P3HT, we anticipated that P3HT would interact with isolated graphitic domains on RGO and improve the dispersibility. To test the hypothesis, GO monolayer dispersion in DMF was mixed with a hot P3HT anisole solution followed by the addition of a hydrazine DMF solution to reduce the GO. In comparison, hydrazine was also added to a GO monolayer dispersion in DMF/ anisole without P3HT. In both cases, the DMF/anisole mixture dissolved both the GO and P3HT, and the solution temperature was kept at 90 °C. As was expected, the RGO in DMF/anisole is well dispersed by P3HT (Figure 6.1 B) while the RGO forms precipitates without P3HT. The hot RGO/P3HT suspension was spin deposited on a mica substrate and examined by AFM. The AFM image clearly shows that

most RGO/P3HT composites exist as monolayers with an average thickness of about 1.3 nm (Figure 6.1). The thickness of the RGO/P3HT monolayer is about 0.4 nm more than that of the surfactant free RGO monolayer (0.9 nm), which suggests the deposition of a thin layer of P3HT on the RGO surfaces. It is interesting to note that, at a concentration of 0.1 mg mL^{-1} in solution, no P3HT nanowires are observed in the AFM image.

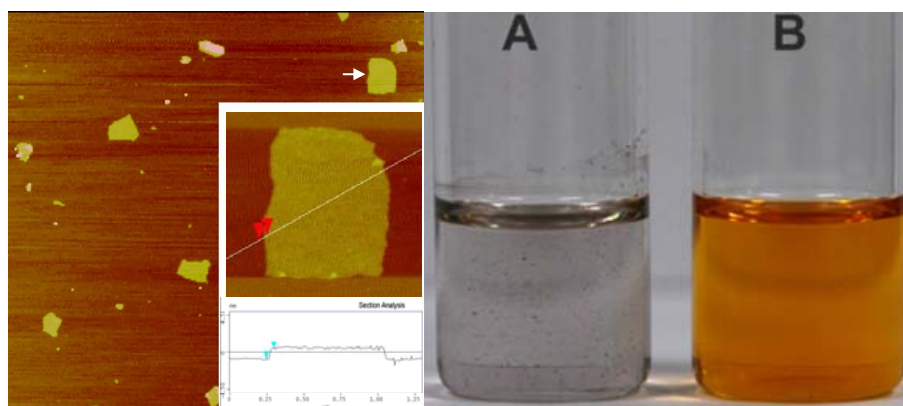


Figure 6.1 (Left) An AFM height image of monolayers of RGO/P3HT composites on a mica substrate (image size $15 \mu\text{m}$). The inset is a higher resolution image (image size $=1 \mu\text{m}$) of a RGO/P3HT monolayer with height analysis showing a thickness of about 1.2 nm. (Right) Reduced graphene oxide (RGO) suspension in anisole without P3HT (A) and with P3HT (B)

While in our previous studies, P3HT can form nanowires at a concentration of 0.05 mg mL^{-1} in anisole. Such observations result from the spin deposition of the hot RGO/P3HT suspension, where most free P3HT in the solution is removed before forming nanowires. It is not surprising to find that RGO/P3HT forms a purple suspension when the solution is cooled with the formation of P3HT nanowires. The TEM image of the suspension shows the presence of short P3HT nanowires on RGO surfaces (Figure 6.2 A). To fabricate longer P3HT nanowires on RGO surfaces in solution, P3HT-dispersed RGO was added to a hot P3HT anisole solution. The solution was then quickly cooled to room temperature and kept overnight for P3HT crystallization. Because of the low solubility of P3HT in anisole at room temperature, P3HT

molecules precipitated from the supersaturated solution, and formed supramolecular structures (nanowires) on the RGO surfaces. The obtained supramolecular structures were examined by TEM and AFM. The TEM image in Figure 6.2 B shows that P3HT nanowires grow from the RGO surfaces, to generate 2D supramolecular structures. The width of the nanowires is about 14 nm, which is the same as that of the free P3HT nanowires prepared without RGO. The selected area electron diffraction (SAED) pattern (Figure 6.2 B, inset) of the P3HT nanowires clearly shows the (010) phase reflection, which suggests the presence of P3HT crystalline structures.²⁷⁸

279

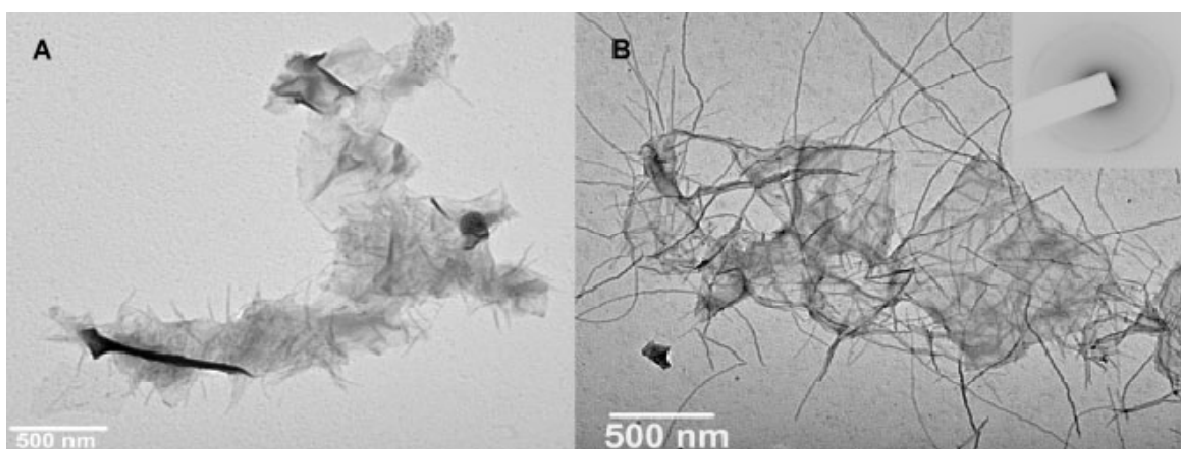


Figure 6.2 TEM images of A) RGO/P3HT composites showing RGO with short P3HT nanowires and B) P3HT supramolecular structures on RGO formed in solution. The inset is the SAED pattern of the P3HT nanowires. The width of the nanowires is about 14 nm.

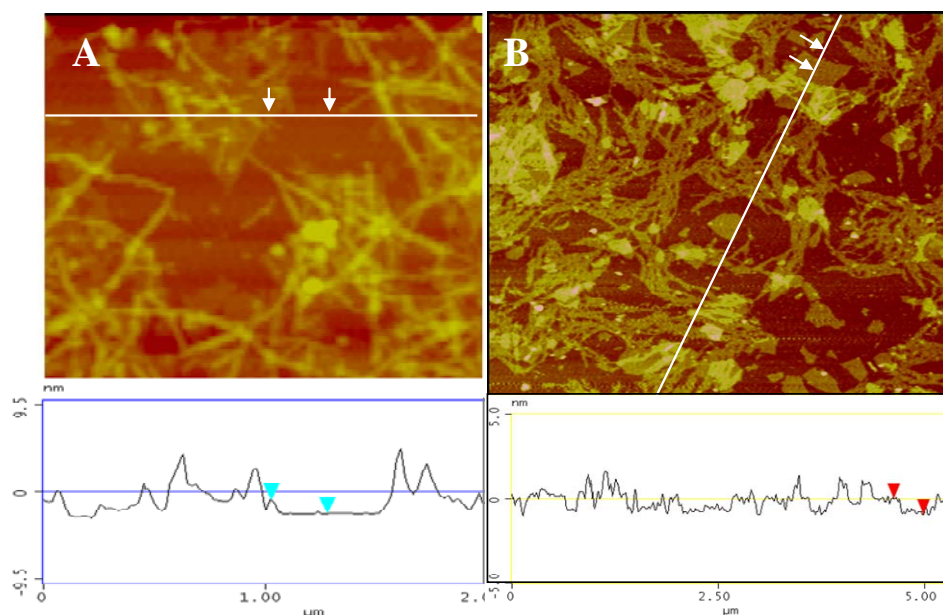


Figure 6.3 AFM images of A) P3HT nanowires on RGO monolayers formed in solution on a mica substrate by drop casting (image size = 2 μm) and B) P3HT nanowires formed on surfactant free RGO monolayers on a mica substrate by drop casting followed by removal of the solution by spinning (image size = 5 μm).

It is important to note that, although excess P3HT molecules are present in the solution, most of the P3HT molecules formed nanowires on RGO with some free nanowires remaining in the solution. This observation suggests that RGO may function as seeds for the formation of P3HT supramolecular structures. The AFM height image (Figure 6.3 A) shows the same P3HT supramolecular structures on RGO surfaces as those observed by TEM. The individual RGO monolayers are clearly visible from the height contrast. From the AFM height analysis in 6.3A, the height of the RGO is around 1.3 nm and the height of P3HT ranges from 4 to 5 nm, which is approximately 2 or 3 times the lattice dimension of the P3HT unit cell (1.68 nm).²⁸⁰⁻²⁸³ It is interesting to note that P3HT nanowires connect individual RGO nanosheets, which suggests potential applications in nanometer-scale graphene-based electronics. The P3HT supramolecular structures were also fabricated on surfactant-free RGO monolayers on mica substrates. The RGO monolayer was produced by a hydrazine reduction of GO dispersed in basic aqueous solutions.¹⁰²

In our studies, a drop of hot P3HT anisole solution (0.1 mg mL^{-1}) was placed on the mica substrate covered with RGO monolayers. After 20 s, excess solution was spun off the substrate, and the sample was examined by AFM. In the AFM height image (Figure 6.3 B), the brighter areas indicate P3HT nanowires formed on the RGO surfaces. The height analysis of the sample suggests that the thickness of RGO is about 1.3 nm while the height of the P3HT nanowires is about 1.7 nm. Compared with the height of the P3HT nanowires (4–5 nm) in Figure 6.3 A, the P3HT nanowires formed through this process are monolayer P3HT unit cells. We believe that such a result is attributable to the fast spin-removal of P3HT solutions that hinders the self-assembly of multiple P3HT unit cells. The formation of the 2D P3HT supramolecular structures is triggered by the RGO enhanced crystallization of P3HT, where the dispersed RGO monolayers function as the nucleation seeds to grow P3HT nanowires. The P3HT (0.05 mg mL^{-1}) isothermal crystallization processes in anisole with GO and RGO were studied by in-situ UV-Vis spectroscopy. The crystallization process was investigated by plotting the change of the UV-Vis absorbance at 600 nm versus time (Figure 6.6 D). The in-situ UV-Vis spectroscopy studies suggest that RGO can greatly accelerate the crystallization of P3HT. The interaction between P3HT and RGO was investigated by examining GO, RGO, P3HT nanowires, and P3HT nanowires on RGO using Raman spectroscopy (Figure 6.4). Raman spectroscopy is a widely used tool to study the structure of conjugated carbon bonds because of their high Raman intensities. In contrast to the Raman spectrum of highly ordered graphite, which shows a sharp Raman band of the graphite lattice at 1580 cm^{-1} (G band)²⁸⁴ and a weak disorder band caused by the graphite edges (D band), a strong D band appears at 1355 cm^{-1} in the Raman spectrum of GO, which is attributed to the sp^3 amorphous carbons generated by the oxidation.²⁸⁵ In addition, the G band becomes broader and blue shifts to 1599 cm^{-1} , which is in good agreement with

reported data.²⁸⁶ The Raman spectrum of the RGO showed two peaks at 1604 cm^{-1} (in plane vibrational G band), and 1345 cm^{-1} (disordered vibrational D band). The G band of RGO shifts to a higher frequency in comparison with pristine graphite, which is attributed to the less ordered carbon and defects of the RGO sheets. In the Raman spectrum of the P3HT nanowires, two dominant peaks observed at 1378 and 1443 cm^{-1} are assigned to C-C skeletal stretching and C=C ring stretching, respectively.²⁸⁷ It is expected that the interaction between the RGO and electron-donating P3HT will lead to a shift of G and D band frequencies. Su et al. reported that the G band of RGO in the Raman spectra was low frequency shifted by electron donors and high frequency shifted by electron acceptors.²⁷¹ In Figure 6.4 D, the G band of the RGO/ P3HT nanowires composite was shifted by 15 cm^{-1} from 1604 (RGO) to 1589 cm^{-1} , which suggests the interaction between RGO and P3HT. The peak at 1447 cm^{-1} signifies that P3HT nanowires remain unaltered and the new peak at 1359 cm^{-1} is a result of the shifting and over lapping of the D band of P3HT and RGO. Therefore, the Raman shift of the G band suggests the interaction between P3HT nanowires and RGO sheets.

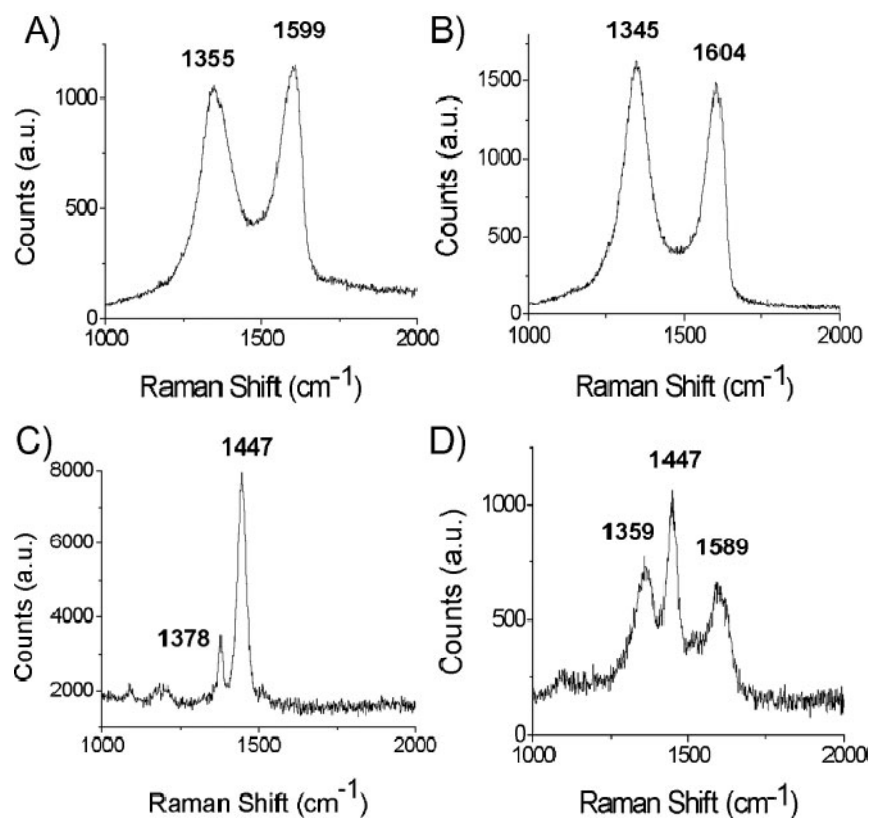


Figure 6.4 Raman spectra of GO (A), RGO (B), P3HT nanowires (C), and RGO with P3HT nanowires (D).

The electrical conductivity of the films deposited from the suspension of surfactant-free RGO, P3HT dispersed RGO, and a P3HT solution was measured using a four-probe method. The conductivity of the P3HT-dispersed RGO films is $6.0 \times 10^{-3} \text{ S m}^{-1}$ while the conductivity of RGO and P3HT films are 103 and $1.2 \times 10^{-4} \text{ S m}^{-1}$, respectively. The lower conductivity of the P3HT-dispersed RGO film compared to that of the RGO film is attributed to the separation of RGO layers by semiconductive P3HT, which is less conductive than RGO. The RGO in the P3HT-dispersed RGO films leads to a higher conductivity than pure P3HT films. The electrical properties of the P3HT/RGO composite films and monolayers are currently under investigation.

6.4 Experimental

6.4.1 Materials

Regioregular P3HT was synthesized by a Grignard metathesis (GRIM) method.²⁸⁸ The degree of polymerization and regioregularity (>96%) was estimated by end-group analysis using ¹H NMR spectroscopy. Graphite flakes were purchased from Dixon (Microfyne). Anisole and N,N-dimethylformamide (DMF) were purchased from Acros organics (New Jersey, USA) and used as received. Hydrazine hydrate was purchased from Sigma–Aldrich (St. Louis, MO).

6.4.2 GO Dispersion

In a typical method GO (1.5 mg) was mixed with 15 mL of DMF in a vial and subjected to 6 hours continuous ultrasonication in a cold water bath. The sonication was performed using a Cup Horn Ultrasonic Converter, to yield a clear homogeneous yellow brown dispersion. The GO dispersion (0.1 mg mL⁻¹ in DMF) was deposited on mica for AFM imaging.

6.4.3 Characterization

Graphite oxide (GO) was prepared from natural purified graphite by Hummers' method. Samples for atomic force microscopy (AFM) imaging were prepared by depositing samples on freshly cleaved mica substrates (Ted Pella Inc., Redding CA). AFM images were taken on a Dimension 3100 Scanning Probe Microscope (Veeco Instruments Inc). Images were obtained using tapping mode with a Si cantilever. All images were collected under ambient conditions at 60% relative humidity and at 25 °C with a scanning rate of 0.5 Hz. Transmission electron microscopy (TEM) images were obtained on a JEOL 1011 electron microscope at 100 kV. UV-Vis absorption was measured using a Cary 300 UV-visible spectrophotometer. Raman spectroscopy was performed

using a Renishaw InVia Raman microscope comprised of a laser (532nm line of solid Si laser), a single spectrograph fitted with holographic notch filters, and an optical microscope (a Leica microscope with a motorized XYZ stage) rigidly mounted and optically coupled to the spectrograph. The spectrometer was calibrated with a Si standard using a Si band position at 520.3 cm^{-1} . The conductivity of RGO/P3HT and RGO thin films was measured using a four-probe method and a Keithley 2400 instrument.

6.4.4 X-ray photoelectron spectroscopy (XPS) characterization of GO and RGO

The chemical composition of GO and RGO were examined using XPS (Kratos Axis 165 Manchester, UK). The XPS spectrum of GO indicated considerable degree of oxidation with four components that corresponded to carbon atoms in different functional groups: non oxygenated ring carbon C (284.5 eV), C in C-O bond (286.6 eV), carbonyl C (287.6 eV) and carboxylate carbon (O-C=O, 289.1 eV) (Figure 6.5). The same peaks were depicted in the spectrum of RGO but with much smaller intensity of the carbon-oxygen bond and a dominant peak of non oxygenated ring carbon. In addition there was another peak at 285.9 eV which indicated C bound to nitrogen corresponding to the reduction with hydrazine hydrate (Figure 6.5 B). The results were consistent with the literature¹⁰⁰ and indicated considerable deoxygenation by the reduction process.

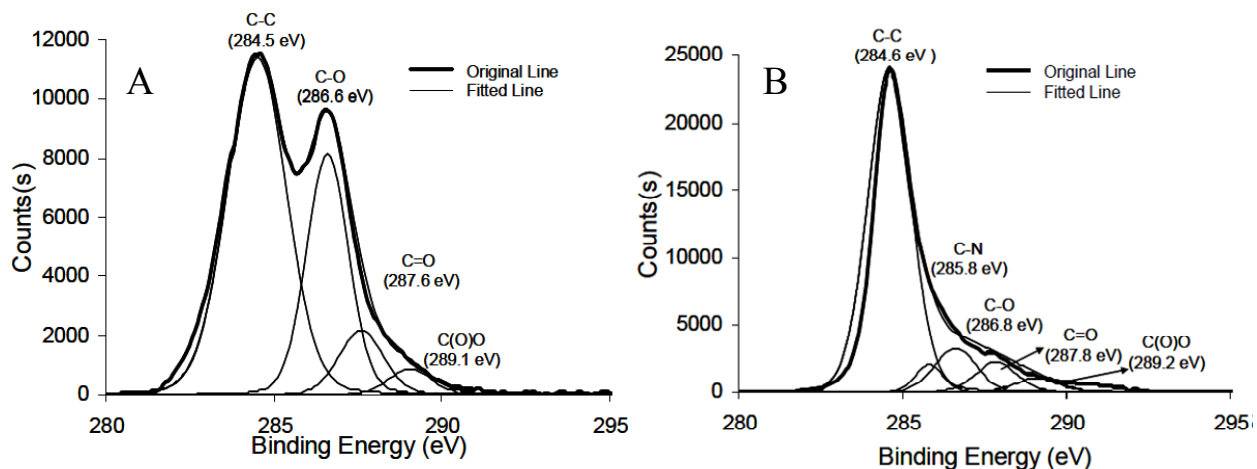


Figure 6.5 XPS Spectrum of (A) GO and (B) RGO.

6.4.5 P3HT Synthesis and In-Situ UV-Vis Spectroscopic Studies of RGO induced P3HT crystallization Process

P3HT was synthesized in our lab using the Grignard metathesis (GRIM) method.²⁸⁸ ¹H NMR spectra were recorded on a Varian Gemini-500 spectrometer at 500MHz using CDCl₃ as the solvent. The average molecular weight (M_n) and polydispersity index (PDI) were determined by gel permeation chromatography (GPC, JASCO LC 2000) with a diode-array UV-Vis detector, and a refractive-index detector, using polystyrene as standards and tetrahydrofuran (THF) as an eluent. The M_n of P3HT is 14,800 with a PDI of 1.2, which is in agreement with that calculated from ¹HNMR spectra by taking into account an over estimation factor of 2.0, when referenced to polystyrene standards.

1.8 mL of hot P3HT solution in anisole (0.1 mg mL⁻¹) was mixed with 200 μ L of GO dispersion in DMF (0.1 mg mL⁻¹). The mixture was heated at 80 °C for 10 minutes and kept at room temperature overnight. Red precipitate was formed due to the crystallization of P3HT in presence of GO. The precipitate was centrifuged and redispersed in 3 mL of hot P3HT solution in anisole by sonication. Hot solution containing GO and P3HT in anisole was used for UV-Vis study. For

RGO, mixture of P3HT solution in anisole (1.8 mL, 0.1 mg mL⁻¹) and GO dispersion in DMF (200 μL, 1 mg mL⁻¹) was heated at 100 °C for 1 hour with hydrazine hydrate (15 μL, 35% in DMF) and kept at room temperature overnight. Red precipitate was formed due to the crystallization of P3HT in presence of RGO. The precipitate was centrifuged and redispersed in 3 mL of hot P3HT solution in anisole by sonication. Hot solution containing RGO and P3HT in anisole was used for UV-Vis study. The crystallization process was monitored by in-situ UV-Vis spectroscopy after the hot P3HT anisole solution was cooled to room temperature by a water bath. Figure 6.6 shows the UV-Vis absorption spectra of P3HT homopolymers during the crystallization process. The absorption band at 600 nm was assigned to the solid state P3HT, which indicated the formation of nanowires.²⁸⁹ It was clear that the crystallization process started with very low absorption intensity at 600 nm. Such a low intensity suggests that a trivial amount of P3HT crystallizes during the quenching process. The evolution of UV-Vis absorption of P3HT with GO, and P3HT with RGO during the crystallization process in anisole are presented in Figure 6.6 (B) and (C) respectively. The intensity of the absorption at 455 nm attributed to the fact that individual or isolated P3HT chain in solution decreases, while the low-energy absorption bands at 510, 550, and 600 nm increased. These low energy peaks were explained as a combination of a π - π^* electronic transition and a strong lattice vibration in P3HT crystalline domains.²⁸⁹ The presence of an obvious isosbestic point at 481 nm in the UV-Vis spectra suggests a direct transformation from dissolved individual polymer chains to ordered nanowires without any intermediate state.²⁷² The absorbance in these fine structural peaks can be employed as a quantitative method to evaluate the amount of the crystallized P3HT in the dispersion. Therefore, the crystallization process could be investigated by plotting the change of the UV-Vis absorbance at 600 nm versus time. It is obvious that RGO can greatly accelerate the

crystallization of P3HT. The crystallization of P3HT completes in less than 3 hours with the presence of RGO (squares), while it takes more than 24 hours for free P3HT to finish the crystallization (circles).

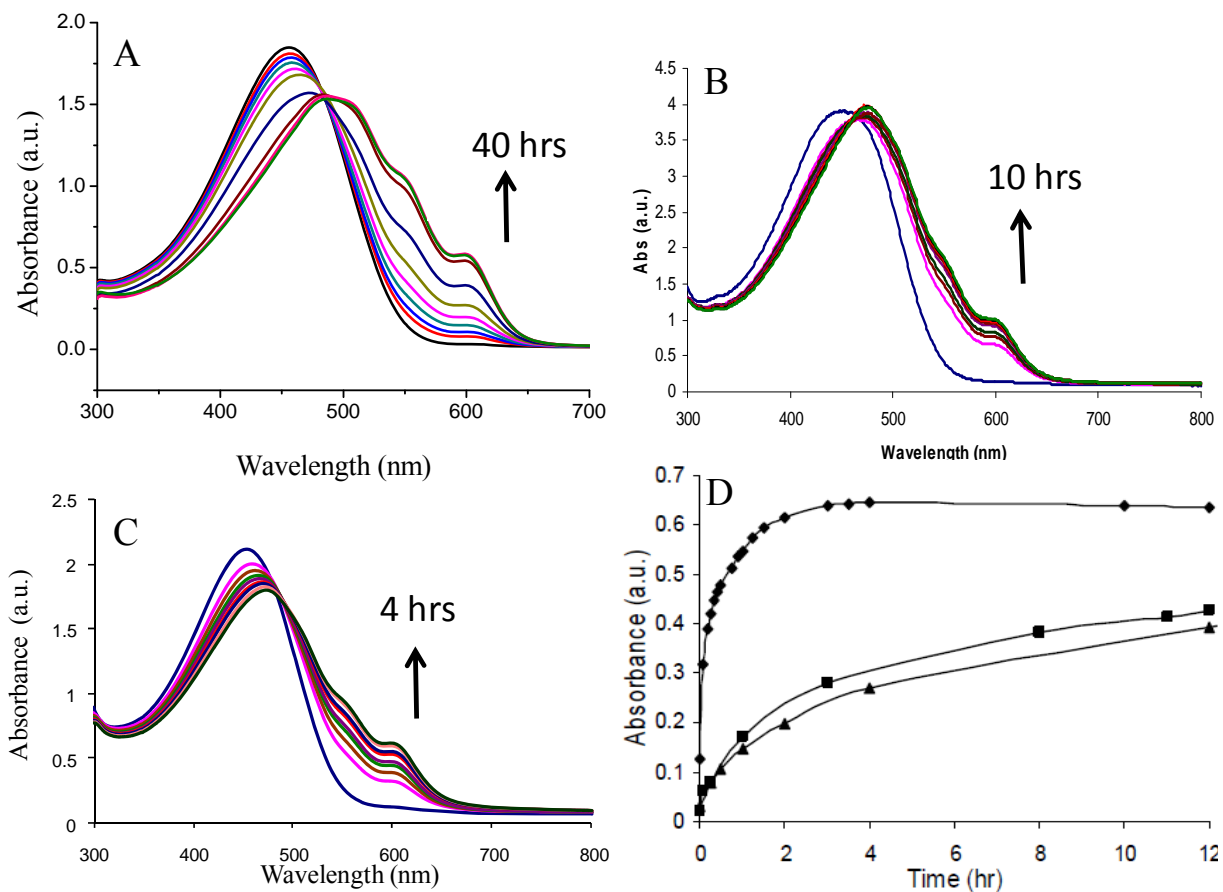


Figure 6.6 A. P3HT nanowires in anisole; B. P3HT with graphene oxide (GO); C. P3HT with reduced graphene oxide (RGO); D. P3HT nanowires in anisole. D. UV-Vis absorbance change at 600 nm of the pure P3HT (triangles), P3HT with GO (squares), and P3HT with RGO (diamonds) suspension during the crystallization process.

6.4.6 Dispersing RGO Using P3HT and Fabricating P3HT Supramolecular Structures on RGO Nanosheets

A hot P3HT solution in anisole (1.8 mL, 0.1 mg mL⁻¹) was mixed with 200 mL of a GO dispersion in DMF (0.1 mg mL⁻¹). A hydrazine solution (35 μL of 35% solution in DMF) was added to the mixture. The mixture was heated at 95–100 °C for 1 hour and cooled to room temperature. After 10 hour, the resultant purple suspension in the mixture was separated by centrifugation. The precipitate was redispersed in 1 mL of hot anisole and yielded a clear yellow solution. One millilitre of the solution was mixed with 5 mL of a hot P3HT solution in anisole (0.1 mg mL⁻¹). The solution was heated at 70 °C for 10 minutes and cooled slowly overnight to form P3HT nanowires on the surface of the RGO nanosheets.

6.5 Conclusion

In summary, we demonstrate a bottom-up approach to fabricate 2D P3HT supramolecular structures on dispersed RGO monolayers. The quasi-isothermal crystallization process monitored by in-situ UV-Vis spectroscopy indicates RGO-induced P3HT nanowire formation. Raman studies suggest the interaction between P3HT nanowires and RGO, which provides an approach to manipulate the electrical properties of RGO. We believe that it is a general approach to build functional supramolecular structures that will lead to numerous applications in nanometer-scale electronics.

CHAPTER 7 GRAPHENE-COPPER PHTHALOCYANINE COMPOSITE THIN FILM WITH OPTOELECTRONIC PROPERTIES

7.1 Abstract

Reduced graphene oxide (RGO) composites, containing tetrasulfonate salt of copper phthalocyanine (TSCuPc) are fabricated through the reduction of graphene oxide in the presence of water soluble TSCuPc. The interaction between RGO monolayer and TSCuPc is investigated using UV-Vis spectroscopy, X-ray photoelectron spectroscopy and Raman spectroscopy. The composites of electron donor (TSCuPc) and acceptor (RGO) are successfully incorporated in devices and their optoelectronic properties are studied. Compared with RGO films, the RGO/TSCuPc composite films have lower conductivity (dark current) but much higher photoconductivity and photoresponsivity because of the presence of donor/acceptor materials and large donor/acceptor (D/A) interfaces for charge generation. The optoelectrical properties of the composite film can be improved by thermal annealing and optimizing the TSCuPc content. The RGO/TSCuPc composite films fabricated by the solution processing method could be used as large-area optoelectronics devices.

7.2 Introduction

Reduced graphene oxide (RGO) has been extensively investigated as the substitute for graphene, a single layer of sp^2 -hybridized carbon atoms, since it is difficult to produce graphene in large scale. Chemically derived single layered RGO sheets can be obtained by a chemical reduction of graphene oxide (GO) generated from the oxidation of pristine graphite via Hummers' method.⁹⁷ The resulted RGO shares many of graphene's intriguing electrical and mechanical properties and its composites offer various applications in sensors,²⁹⁰⁻²⁹³ nanoelectronics,²⁹⁴⁻²⁹⁶ catalysis,²⁹⁷ and energy storage^{298, 299} and conversion devices.³⁰⁰⁻³⁰⁴ For example, graphene-polymer

composite containing RGO nanosheets^{305, 306} and various polymers such as polystyrene (PS),^{294, 307} poly(methylmethacrylate) (PMMA)^{92, 308-312} and sulfonated polystyrene (PSS)¹⁰³ have demonstrated high conductivity and a low percolation threshold attributed to conductive RGO nanosheets. Conductive polymers such as poly(3-hexylthiophene) (P3HT) have been used to stabilize RGO nanosheets and produce hybrid composite materials³¹³ for organic photovoltaic.³⁰⁴ RGO/polyaniline composites have been investigated as supercapacitor electrodes and demonstrated large capacitance, good cycling stability and high flexibility.^{297, 298} While polymers have been extensively utilized to fabricate RGO composites, molecular semiconductors³¹⁴ such as phthalocyanines³¹⁵, porphyrines, perylenes with well defined electronic structures^{270, 316} are also interesting candidates for RGO composites. These organic semiconductors are known as “intrinsic wide band gap semiconductor” (band gap above 1.4 eV) with negligible number of intrinsic charge carriers at room temperature in dark. However, extrinsic charge carriers are created when these materials are doped chemically, electrochemically or photochemically.³¹⁷ For example, metal salt solutions of phthalocyanines (Pc), one of the interesting p-type semiconductors, were blended with MWCNT to produce phthalocyanine sensitized MWCNT films with potential application in solar cell.³¹⁸ Copper phthalocyanine (CuPc) has been used in organic field-effect-transistors (OFETs)^{319, 320} and thin film organic solar cells^{321, 322} as donor materials blended with fullerene³²²⁻³²⁶ and 3,4,9,10-perylenetetracarboxylic bis-benzimidazole as acceptor.³²⁷⁻³³¹ Composites containing RGO and CuPc are expected to have high conductivity and unique optoelectrical properties, making them interesting materials for sensing and energy conversion applications.

In this paper, we report the fabrication of RGO monolayer suspension stabilized by water soluble semiconductive tetrasulfonate salt of copper phthalocyanine (TSCuPc) through the reduction of

graphite oxide monolayers with the presence of TSCuPc. The interaction between RGO and TSCuPc was investigated using UV-Vis spectroscopy, X-ray photoelectron spectroscopy and Raman spectroscopy. The donor (TSCuPc) – acceptor (RGO) composites were successfully incorporated in devices and the optoelectronic properties were studied. Compared with RGO films, the RGO/TSCuPc composite films have lower conductivity (dark current) but much higher photoconductivity and photoresponsivity. The optoelectrical properties of the composite film can be improved by thermal annealing and optimizing the TSCuPc content.

7.3 Results and Discussion

7.3.1 Characterization of the composite ink

Graphene oxide was synthesized by Hummers' method⁹⁷ and reduced with hydrazine hydrate in the presence of TSCuPc to create a stable suspension of RGO monolayers stabilized by TSCuPc. In this system, RGO nanosheets are stabilized via $\pi - \pi$ interaction between TSCuPc molecules and RGO nanosheets. TSCuPc has large aromatic plane and can anchor onto the RGO surface without disturbing its electronic conjugation. Moreover, the sulfonate groups on TSCuPc introduce negative charges on RGO sheets and stabilize the RGO dispersion, providing single sheets of TSCuPc functionalized RGO for device fabrication. In contrast, irreversible aggregation and precipitation of graphitic sheets occurred upon the reduction of GO without TSCuPc (Figure 7.1 inset). Atomic force microscopy (AFM) study (Figure 7.1) of RGO/TSCuPc composites provides detailed information about the individual layer of the RGO/TSCuPc composite sheets. The sample was prepared by spin coating the composite suspension on a freshly cleaved mica substrate. The cross section analysis in the AFM height image indicates the thickness of the TSCuPc attached RGO sheet to be ~ 1.9 nm whereas the thickness of a single

layer RGO was found to be approximately 1 nm in our and other's studies.^{92, 313} Therefore, the AFM height image confirmed the non-covalent attachment of the aromatic molecules on the RGO basal plane through π - π interaction. The small dots in the AFM images are aggregates of TSCuPc.

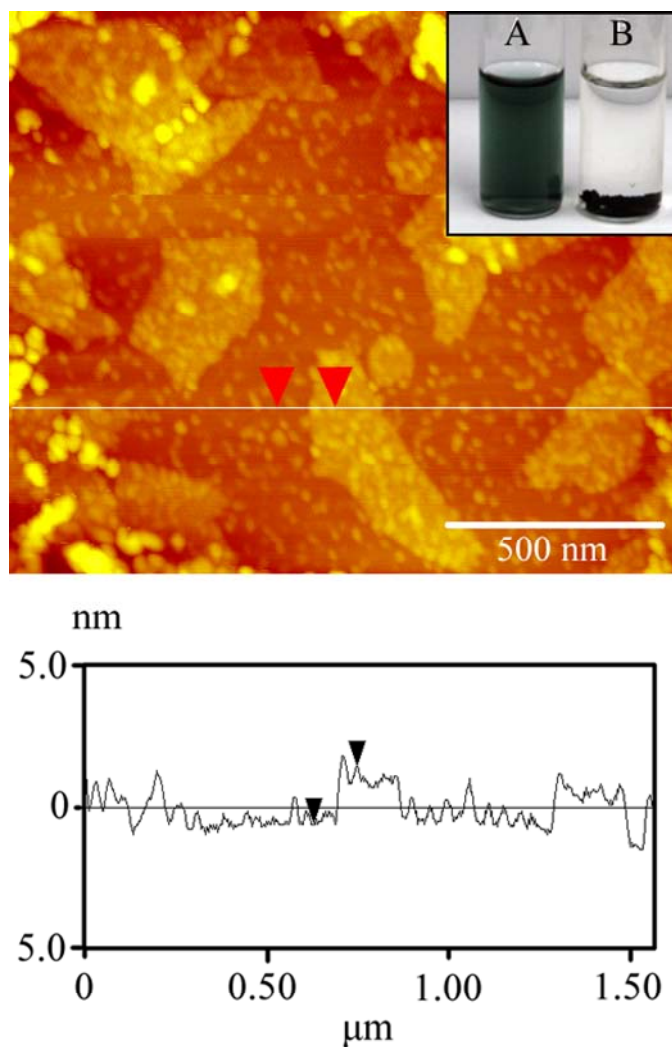


Figure 7.1 Tapping mode AFM image of the RGO-TSCuPc composite on mica. Inset shows (A) Reductuin of GO in presence of TSCuPc to form RGO-TSCuPc composite ink (B) Precipitate formed when GO reduced without TSCuPc.

The attachment of the small TSCuPc molecules to RGO sheets was further supported by the spectroscopic studies using UV-Vis spectroscopy, X-ray photoelectron spectroscopy (XPS) and

Raman spectroscopy. The UV-Vis absorption spectra of TSCuPc, RGO/TSCuPc composite and pure RGO films were compared in Figure 7.2. TSCuPc had broad band absorption from 500 nm to 750 nm with a maximum absorption at 608 nm. Three main peaks at 220 nm, 330 nm and 608 nm in spectrum of TSCuPc films red shifted and became broader in the spectrum of RGO/TSCuPc composite film. The changes in the peak position and the evolution of the exiplex at 720 nm in the composite spectrum were attributed to the charge transfer interaction between the RGO and TSCuPc.^{318, 332}

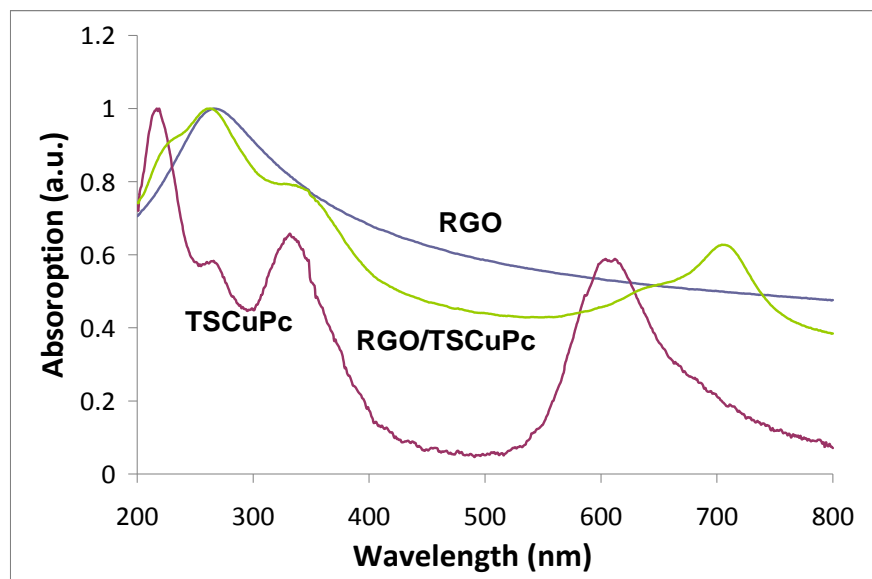


Figure 7.2 UV-Vis absorption spectra of RGO, TSCuPc and the composite film.

The charge transfer interaction between TSCuPc and RGO was further proved by XPS analysis of the composite film. Due to the charge transfer from TSCuPc to RGO, the Fermi level of RGO up-shifted towards conduction band and resulted in an up-shift of C1s XPS peak. Deconvolution of the C1s peak in the XPS spectrum of the composite film revealed binding energy of various bonds, among which binding energy of C-C of sp^2 carbon in the graphene sheet was the most

important since the change in Fermi level of graphene corresponded to the sp^2 peak position.³³³,³³⁴ Figure 7.2 shows that the C-C peak of the RGO/TSCuPc composite (285.9 eV) up-shifts by 1.3 eV compared to that of pure RGO (C-C peak at 284.6 eV).³¹³ The XPS peaks of the other bonds in TSCuPc and RGO/TSCuPc composites also agree with the charge transfer phenomena. The N1s peak of TSCuPc consists of two peaks separated by ~ 1.2 eV, assigned to two groups of four nitrogen atoms in different chemical environments in the molecule. In the spectrum of the composite, the N peak shifts to higher binding energy by 0.3 eV compared to that in pure TSCuPc. Such higher binding energy shift indicates the charge transfer from TSCuPc to RGO in the composite because the binding energy is related to the electron density around the nucleus. The lower the electronic density is, the higher the binding energy. It is evident from the composite XPS spectrum that the difference in electron density between the two groups of dissimilar nitrogen increased from 1.2 eV to 1.6 eV as a result of decreased electron density on phthalocyanine macro cycle. The binding energy of Cu $2p_{3/2}$ peak upshifts in the composite spectra by 0.3 eV as compared to that in TSCuPc, suggesting the charge transfer from TSCuPc to RGO. The S 2p peak in TSCuPc is split into two components separated by 1.6 eV. The peak at 168.4 eV is assigned to S $2p_{3/2}$ in $SO_3^- Na^+$ salt in TSCuPc and the peak near 170 eV corresponds to the amount of sodium present in the film. In the composite spectrum, although S 2p peak has a global shift of 0.3 eV towards higher binding energy, the binding energy of component $2p_{3/2}$ (168.5 eV) is similar to that the binding energy of component $2p_{3/2}$ in TSCuPc (168.4 eV). Such similarity is probably due to the electron withdrawing property of sulfonate groups in TSCuPc. The phthalocyanine macrocycle donates charges to RGO, resulting in the reduction of the electron density in the molecule. However, SO_3^- , an electron withdrawing group, is less affected by the decreased charge density on the phthalocyanine macrocycle. Overall, the higher energy

shift in all the components of TSCuPc is consistent with the reported charge transfer phenomenon.^{270, 333, 334}

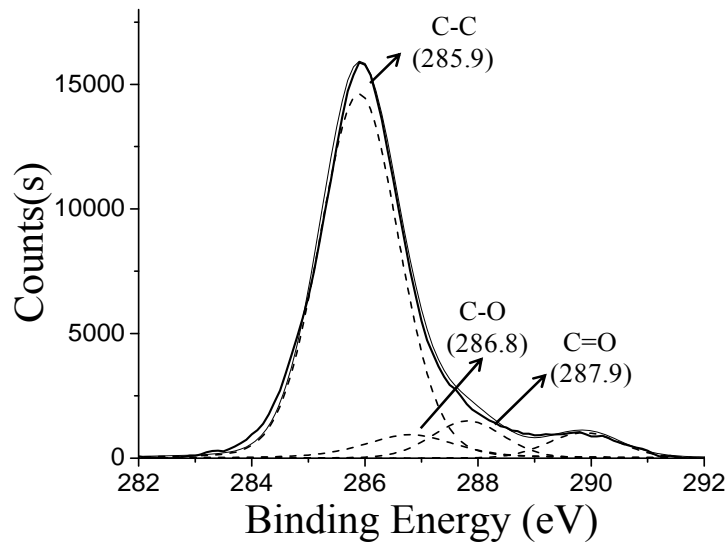
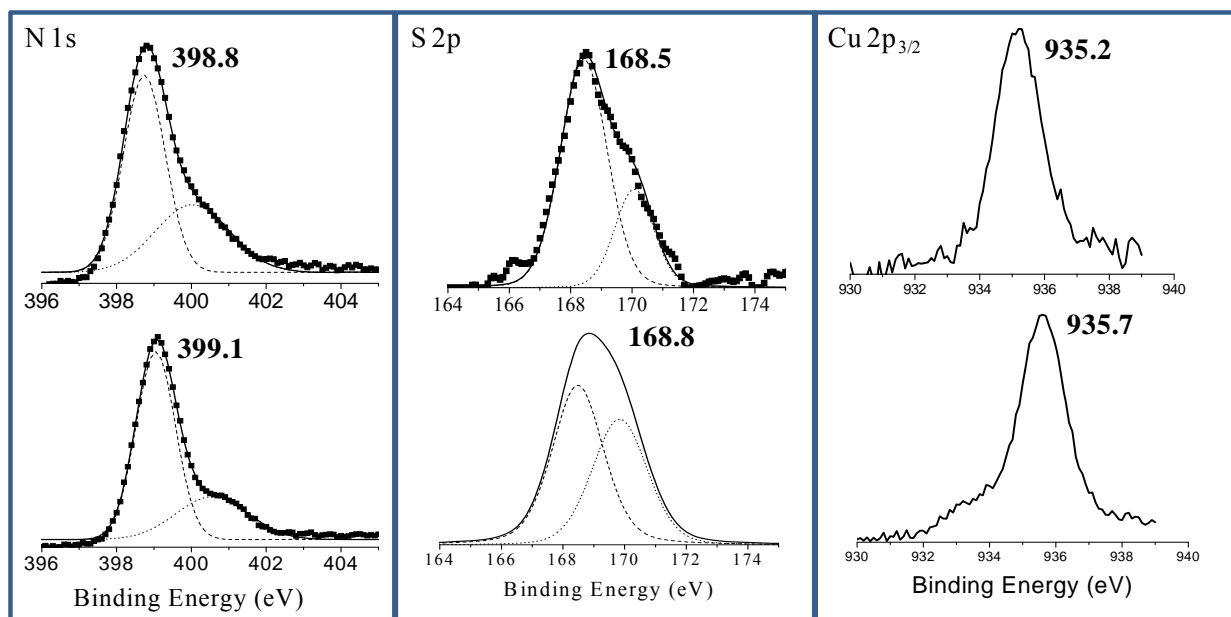


Figure 7.3 C1s XPS peak of RGO-TSCuPc composite.



▪ Original data — Curve fitted data

Figure 7.4 XPS spectra of TSCuPc (upper row) and the composite (bottom row).

The significant π electron interaction between the donor TSCuPc and acceptor RGO basal plane was further confirmed by Raman spectroscopy. TSCuPc molecules have almost 20 vibrations in Raman spectra,³³⁵ among which only the finger print bands are described in this report. The most intense Raman bands are found at 1526, 1340 and 686 cm^{-1} for the TSCuPc film. The Raman spectrum of the RGO shows two peaks at 1604 cm^{-1} (in plane vibration G band), and 1345 cm^{-1} (disordered vibration D band). Specifically, the G band in the composite film was found to shift towards lower frequency by the electron donor TSCuPc. In the composite spectra, the G band appears at 1598 cm^{-1} which is down-shifted by 9 cm^{-1} compared to that of RGO at 1604 cm^{-1} . The fact is well documented by Su and coworkers, where the reported data of Raman spectroscopy showed low frequency peak shift by donor molecules and the reverse by the acceptor molecules in the donor-acceptor composite systems with graphene.³¹⁶ The softening of the G band is due to the increased abundance of charge carriers^{333,335-337} provided by the TSCuPc molecules on the graphene basal plane, which eventually raises the Fermi level.^{334, 338, 339} The peak at 1350 cm^{-1} and new peak at 1533 cm^{-1} is due to the peak shift and peak overlapping between the TSCuPc and RGO in the composite. Therefore, the Raman shift provides important information about the charge transfer between the large aromatic TSCuPc molecules and the RGO sheets and supports the results obtained from the XPS analysis.

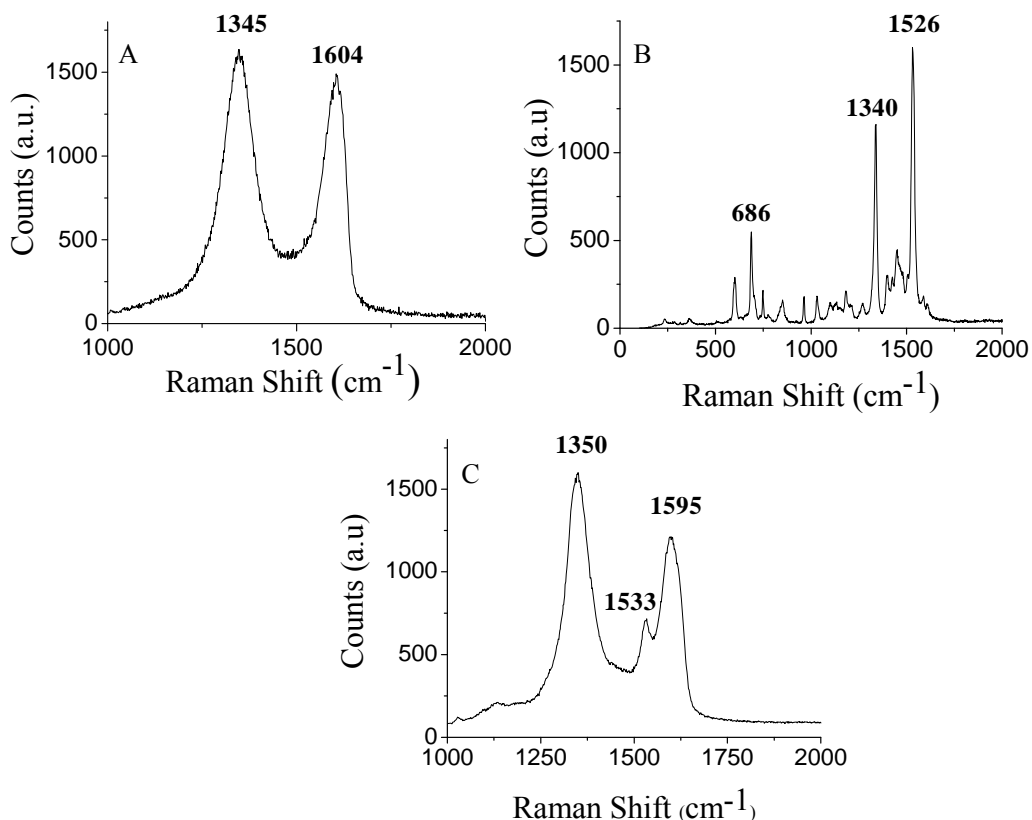


Figure 7.5 Raman spectra of (A) RGO (B) TSCuPc film and (C) RGO–TSCuPc composite film.

7.3.2 Measurement of the optoelectronic property

Devices were fabricated using RGO/TSCuPc dispersion with different loadings of TSCuPc. Figure 7.6 (a) is a schematic illustration of the fabricated device along with the electrical transport measurement setup. Figure 7.6 (b) shows the current-voltage (I-V) characteristics of one of our RGO/TSCuPc (1:2.5 ratio) thin film devices before and after mild thermal annealing. The annealing was performed at 120 °C for an hour under vacuum. Within the bias voltage of -1V to 1V, the conduction is Ohmic. A conductivity of 740 S/m before annealing and 3400 S/m after annealing was obtained from the Ohmic I-V curve, respectively, showing that the conductivity increased by a factor of 4.5 upon thermal annealing. Similar conductivity increase

upon mild annealing has been observed in all of our composite films and can be attributed to the better contact between the films and metal electrode as well as better interfacial contact between individual RGO/TSCuPc sheets. In addition, further partial reduction of RGO can also occur during the vacuum annealing leading to increased conductivity of the RGO/TSCuPc composite films.^{100, 261, 340}

Figure 7.6 (c) shows the I-V curve of the same device under dark and light illumination. At $V=1V$, the current changes from 1.2 mA to 1.6 mA upon light illumination. The photoconductivity (obtained by subtracting dark conductivity from light conductivity) of this device was calculated to be 1000 S/m giving a photosensitivity (ratio of photo conductivity to dark conductivity) of 30%. Similar measurements in dark and light illumination were performed for all four composite films with different RGO/TSCuPc ratio. Table 1 summarizes experimental results of annealed thin films showing dark conductivity, photoconductivity, and photosensitivity for all four films that we studied. It has been found that the dark conductivity decreases with increased loading of TSCuPc. On the other hand, photoconductivity and photosensitivity increases as the TSCuPc loading increases and reaches the maximum value at the RGO:TSCuPc ratio of 1:2.5. Further increase of TSCuPc causes a decrease in photoconductivity and photosensitivity.

We observed that the dark conductivity of the devices decreased with the increase of TSCuPc/RGO ratio. It was expected as TSCuPc was more insulating than RGO and the TSCuPc in RGO sheet acted as a scattering center and hindered the path of flow of charge carriers. Hence high loading of TSCuPc decreased the mobility (μ) of the charge carriers in the composite as compared to pure RGO. In contrast, the photoconductivity initially increased with increasing loading ratio of TSCuPc (up to 2.5) and then decreased with further increase of TSCuPc. This

can be explained as following: The photoconductivity is caused by exciton creation via absorbing photons, dissociating excitons into free charge carriers and transporting these carriers into source and drain electrodes. The photoconductivity can be expressed as $\sigma_{ph} = \Delta n q \mu$, where Δn is the photo generated charge carriers, q is the electronic charge, and μ is the mobility of charge carriers. In Figure 7.6 (d), we show a band diagram of our RGO/TSCuPc devices. The unique 2D- π -conjugated dish-like shape of RGO can effectively facilitate the desired interface with TSCuPc for exciton dissociation and charge transport. After the dissociation of the excitons, the holes are collected at the drain electrode from the HOMO level of TSCuPc (5.38 eV) while the electrons easily transferred from the LUMO level of TSCuPc (3.77 eV) to source electrode through RGO (4.7 eV).³⁴¹ The loading of TSCuPc to RGO, led to the competition between the increased number of photogenerated carriers (Δn) and decrease in carrier mobility (μ). The photoconductivity increased upto the loading of 1:2.5 of the RGO/TSCuPc film compared to that of RGO film. The reason was the constant charge transfer from TSCuPc to RGO which increased the number of charge carriers and exciton dissociation with increased interface between RGO and TSCuPc. Additional loading of TSCuPc to RGO (1:5), considerably decreased the photoconductivity of the composite. In this case, although Δn continuously increased with increasing loading of TSCuPc, mobility (μ) of the carriers significantly dropped. The excess TSCuPc created large amount of scattering centers hindering the mobility of the charge carriers. The decreased mobility triumphed over the number of charge carriers in the competition, causing an overall decrease of the photoconductivity for 1:5 composite.

Table 7.1 Dark conductivity, Photoconductivity, photoresponsivity and photosensitivity for RGO/TSCuPc composite films (average film thickness was 120 nm and optical properties was measured under 100 mW/cm² intensity of light)

Ratio of RGO/TS CuPc (on Solid)	Dark Conductivity (S/m)		Photo Conductivity (S/m)		Photoresponsivity (mA/W)		Photosensitivity (%)	
	Before annealing	After annealing	Before annealing	After annealing	Before annealing	After annealing	Before annealing	After annealing
1:0	-	7730	-	200	-	0.37	-	2.6
1:1	1680	6600	50.66	237	0.38	0.45	3	3.5
1:2.5	740.9	3400	453	999.7	0.84	1.15	61	31
1:5	150	636	6.98	18.17	0.135	2.00	4.6	16

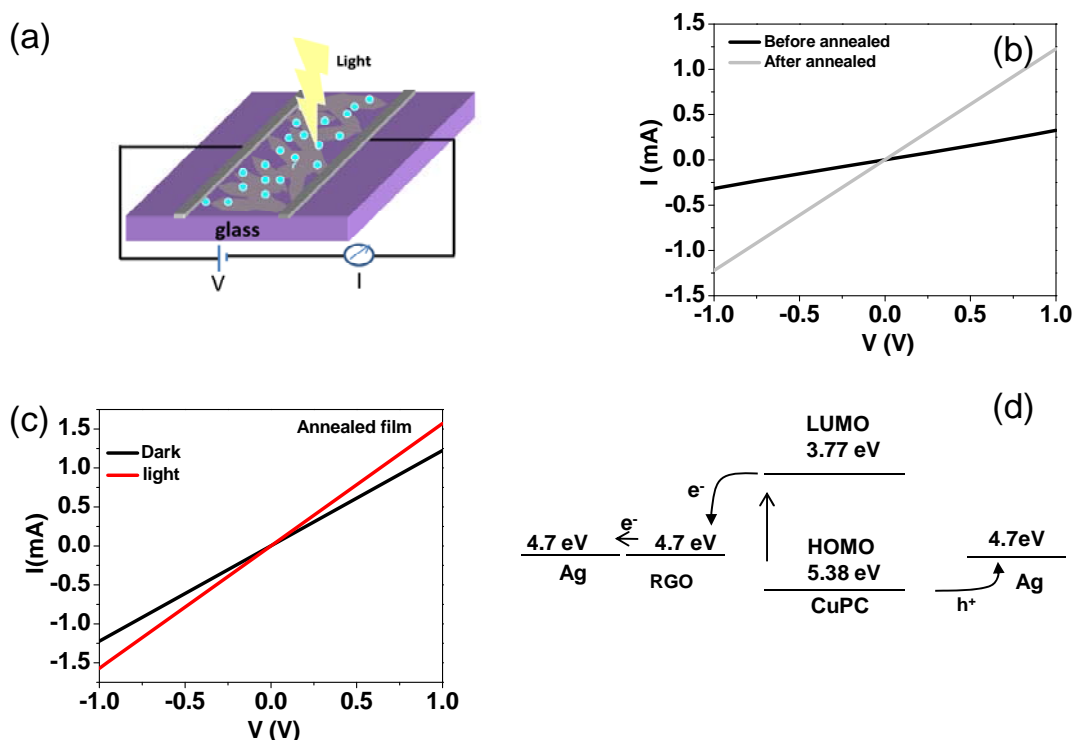


Figure 7.6 (a) Schematic diagram of the device and electron transport measurement setup. (b) Current-voltage characteristics of the RGO-TSCuPc (1:2.5) device (before annealing and after annealing), (c) Current-voltage characteristics of the annealed RGO-TSCuPc (1:2.5) device under dark and light illumination. The inset shows Current-voltage characteristics of the

annealed RGO-only device under dark and light illumination. (d) Energy level diagram of TSCuPc and RGO.

7.4 Experimental Method

7.4.1 Synthesis and characterization of graphene/TSCuPc composite ink

Graphite oxide was prepared by a modified Hummers' method from natural graphite powder purchased from Dixon Graphite (Microfyne).⁹⁷ 10 mg of GO was dispersed in 10 mL of deionized water (DI water) using cup-horn ultrasonication to generate a homogeneous brown solution. The solution was centrifuged for 15 minutes at 5000 rpm to remove negligible amount of aggregates. 10 mL of GO solution (1mg/mL) was mixed with 25 mL of 0.01M TSCuPc aqueous solution in a round bottom flask with a water-cooled condenser. Hydrazine hydrate (Sigma-Aldrich St. Louis, MO) was added and the solution was heated at 90 °C for 1 hour. The color of the solution changed from dark blue to dark green. The resultant solution was stable for more than 3 months and contained reduced graphene oxide monolayer sheets as confirmed by AFM images taken on a Dimension 3100 Scanning Probe Microscope (Veeco Instruments Inc). A dilute composite aqueous solution was spin coated onto a freshly cleaved mica substrate and left overnight to evaporate the water, and was used for AFM measurement. UV-Vis absorption spectra of the thin films of TSCuPc, RGO/TSCuPc composite and pure RGO were recorded on quartz substrates using a Cary 300 UV-Visible spectroscope. The films were deposited from 1 mL aqueous solutions of each sample on quartz slides followed by evaporating solvents at 60 °C on a hot plate. The same film was used for X-ray photoelectron spectroscopy (XPS) analysis (Physical Electronics 5400 ESCA). Raman spectroscopy was performed using a Renishaw InVia Raman microscope comprised of a laser (532 nm line of solid Si laser), a single spectrograph fitted with holographic notch filters, and an optical microscope (a Leica microscope with a

motorized XYZ stage) rigidly mounted and optically coupled to the spectrograph. The spectrometer was calibrated with a Si standard using a Si band position at 520.3 cm^{-1} .

7.4.2 Device fabrication

The thin film devices were fabricated on clean glass substrate by drop-casting aqueous suspensions containing RGO/TSCuPc composite sheets. The solvent was allowed to evaporate in a fume hood for a few hours. Four different films were prepared with TSCuPc/RGO ratios of 0, 1, 2.5, and 5. The average thickness of each film was $\sim 120\text{ nm}$. Conducting silver paint was then used to make pairs of parallel electrode of channel length of 8 mm and channel width of 25 mm.

7.4.3 Measurement of optoelectronic properties

The room temperature dc charge transport measurements of the films were performed using a standard two-probe method using Agilent 4145B semiconductor parameter analyzer connected to a probe station under dark and light illumination condition. A xenon lamp (solar-light simulator, Oriel 96000) was employed as the illumination source. The photo intensity was measured using a calibrated silicon photodiode. Unless mentioned otherwise, the light intensity was 100 mW/cm^2 . The spot size of the beam covered the whole sample. The photocurrent was calculated by subtracting the dark current from the current under light illumination.

7.5 Conclusion

Reduced graphene oxide was dispersed and functionalized non-covalently by large aromatic donor molecule TSCuPc which effectively increased RGO stability and facilitated the extraction of monolayer RGO for device fabrication. The UV-Vis, Raman and XPS spectroscopic studies clearly indicated the charge transfer between TSCuPc and RGO. The optoelectronics studies of

large area RGO/TSCuPc films with different TSCuPc loading ratio. The dark conductivity was found to decrease with the increase of TSCuPc loading ratio where as the photoconductivity increased and finally decreased at higher loading ratio of TSCuPc. The maximum photo conductivity was observed for the device made from RGO/TSCuPc with a ratio of 1:2.5. The photosensitivity of the RGO/TSCuPc (1:2.5) film was improved up to 15 times compared to RGO films. The RGO/TSCuPc composite films fabricated by the solution processing method could be used as large-area optoelectronics devices.

SUMMARY AND OUTLOOK

This dissertation is focused on the synthesis of functional nanomaterials and their multi-directional potential applications. The nanostructured materials were synthesized and assembled through ‘bottom up approach’ to develop organic-inorganic hybrid structures with interesting optical, electrical and surface properties. The structure-property relationship of the nanostructured materials was thoroughly investigated and tuned during processing to achieve optimized performance for various applications. Electrospinning and layer-by-layer (LBL) self assembly were used as techniques to fabricate nanofibers and multilayer films respectively followed by their functionalization to achieve desired applications. Graphene based composites were prepared by simple non-covalent functionalization of graphene surface with different nanomaterials and their potential applications in optoelectronic device were investigated.

Contribution to the field

My current research on nanomaterials and nanotechnology involved several major techniques of nanomaterial synthesis and processing, such as, LBL, electrospinning technique and bottom-up self-assembly approach to fabricate hybrid nanostructures. Although these techniques are well-known and well-established, I synthesized some unique and advanced functional materials using those techniques with desired structures and properties for specific applications. For example, conformal coatings on microfluidic channels were fabricated with LBL self assembly, and these coatings were further functionalized to show temperature dependent switchability in surface wetting. Incorporating such a switchable patch into a microchannel led to an in-depth understanding not only of the property of the materials used, but also of the synthetic scheme and the microfabrication techniques. Finally, a successful testing of the as-prepared device

established the proof of concept. The device was further modified with an integrated microheater to reduce the time lag between the heating and cooling cycle which improved its performance. In addition, understanding of the structure-property relation of the switchable surface led to another very interesting work following my previous research. An analytical model for the wettability switching characteristic of a nanostructured thermoresponsive surface was proposed,¹⁷⁵ which is expected to contribute appreciably in the related field. Three different thermosensitive platforms were fabricated and the contact angle change of a water droplet on the surface with varying surface temperature was analytically modeled to study the transfer characteristics (variation in contact angle versus temperature) of the unique nanostructured thermosensitive surface. The proposed model, analysis, and expressions provided a broad mathematical framework for thermoresponsive surfaces that exhibited a sigmoidal logistic transfer characteristic.

Another interesting research based on the same basic technique of the LBL multilayer film assembly was to fabricate antireflection (AR) coating on plastics. It is interesting to note that a new spray coating technique was introduced to replace conventional dip coating to develop assembled layers. We demonstrated that the spray coating technique was more efficient than the dip coating, as the newly developed process required less number of layers compared to the conventional one to show same performance. The newly-reported spray coating technique also provided a cost effective and versatile approach to fabricate conformal AR coatings on plastics with the potential of mass production. The mechanical properties of the coatings were improved by the functionalization of the plastic surface with APTS and sol-gel and the coating was made abrasion resistant by sol-gel treatment on the AR coating. The resultant abrasion-resistant AR coating was able to reduce the reflection from 5 to 0.3% on plastic.

Second approach for the development of assembled nanostructures was electrospinning technique. Novel polyelectrolyte (PAA/PAH) based nanofibers were fabricated using this technique. The fibers were unique in their solubility as the uncrosslinked fibers were insoluble in water. However, these fibers were thermally crosslinked to conduct the experiments in PBS buffer, a simulated body fluid because the buffer had high ionic strength and could dissolve the uncrosslinked fibers. The pH dependent behavior of the polyelectrolytes was interesting and important in the field of polyelectrolyte based materials like films, fibers, hydrogels, etc. This property of the polyelectrolytes was further investigated by studying the pH dependent loading and release of a model drug methylene blue (MB) from the PAA/PAH nanofibers. These fibers were capable of controlling MB release with the change of pH. A high rate of release at low pH and slower release rates at high pH were observed. Further, the release property of PAA/PAH fibers was tuned by depositing different coatings onto fiber surfaces. A temperature controlled MB release in PBS solution was achieved by depositing PAA/PNIPAAm multilayers onto the fiber surfaces and a sustained release was obtained by converting the fiber surface superhydrophobic. Release of drug from the superhydrophobic fiber was studied in water as a case of 'under water superhydrophobicity'. Effect of surfactant on the wetting of superhydrophobic surface and resultantly on the release profile of drug was also investigated.

The third approach was based on graphene based composite preparation with a semiconducting polymer –poly(3-hexylthiophene) (P3HT) and an organic large molecule semiconductor-tetrasulphonate salt of copper phthalocyanine (TSCuPc). The focus of the research was to introduce reduced graphene oxide (RGO) as an emerging material in the field of energy research. A bottom-up approach was demonstrated to fabricate 2D P3HT supramolecular structures on P3HT-dispersed RGO monolayers. The quasi-isothermal crystallization process monitored by in-

situ UV-Vis spectroscopy indicated RGO-induced P3HT nanowire formation. The Raman study indicated the charge transfer interaction between the materials and the high charge mobility of the P3HT nanowires (reported elsewhere) made the composite promising for optoelectronic device fabrication. We believe that it is a general approach to build functional supramolecular structures that would lead to numerous applications in nanometer-scale electronics. On the other hand, RGO was dispersed and functionalized non-covalently with large aromatic donor molecule TSCuPc which effectively increased RGO stability and facilitated the extraction of monolayer RGO for device fabrication. The Raman, XPS and UV-Vis study indicated the interaction between RGO and TSCuPc. The well-dispersed and percolated RGO in TSCuPc matrix showed high photosensitivity. The value was found to be 15 times higher than that of the pure RGO. Therefore the RGO based composites can be a potential candidate for the fabrication of large-area optoelectronic devices by the solution processing method.

Major accomplishments and their applications

Two simple techniques were used to fabricate novel materials with unique properties and applications. The major accomplishments were

- ✓ Expertise in synthesizing functional nanomaterials with advanced properties using different techniques
- ✓ Tuning structure-properties-processing-performance of functional materials and thin films
- ✓ Basic understanding of the wetting behavior of the superhydrophobic and superhydrophilic surfaces which led routes to prepare and functionalize surfaces to change their wetting property for desired applications

- ✓ In depth knowledge in polyelectrolyte chemistry and tune their functional groups to show unique properties
- ✓ Understanding graphene based chemistry and expertise in synthesizing monolayer graphene and graphene based composites for energy research

Applications:

- Conformal superhydrophobic/hydrophilic thermal switchable surface was developed by the LBL deposition of multiple organic/inorganic layers followed by the functionalization with a thermo-responsive polymer for flow control in microfluidic channels
- Nanoparticle and polyelectrolyte based thin film antireflective and antifogging coating was fabricated on glass and plastic by various liquid deposition techniques (spray and chemical bath deposition)
- Ultrathin fibers comprising of two weak polyelectrolytes were fabricated by electrospinning technique. Methylene blue was used as a model drug to evaluate the potential application of the fibers for drug delivery
- Poly(3-hexylthiophene) supramolecular structure was fabricated on reduced graphene oxide nanosheets with improved compatibility and property
- Graphene and TSCuPc based nanocomposite was prepared in a facile one step method as a promising optoelectronic material
- High quality chemically reduced graphene oxide sheets were synthesized for fabrication of high yield field effect transistors by dielectrophoresis and to study the

space charge limited conduction in dielectrophoretically assembled few layers of graphene

Future work

The future work following the reported research may include research on wetting behavior of superhydrophobic fiber and effect of surfactant on the release of drug from the same. Different type of charged surfactants and charged drug molecules and studying their interaction will definitely contribute more to the field as it is expected to affect the rate of release of drug from the fibers. Other biocompatible polyelectrolytes such as chitosan should be included in the study for controlled release of drug from polyelectrolyte based biodegradable nanofibers. Additionally, the fibers can be functionalized to render them glucose sensitive and the release of drug can be studied under the influence of glucose in the medium. The research is in progress with some interesting preliminary data. Also, there are ample scopes of research in the graphene chemistry. The optoelectronic property of the graphene-P3HT composite has to be investigated. The graphene monolayers can be functionalized with positively and negatively charged species so as to fabricate all-graphene multilayer films by LBL self assembly technique which may perform as conducting membranes. I believe that those were the few possible research extensions that I discussed so far. There are definitely many remaining that I overlooked. Thorough understanding of the reported work will create more opportunities to carry forward the research in synthesis and functionalization of nanostructured materials.

REFERENCES

1. Kuchibhatla, S.; Karakoti, A. S.; Bera, D.; Seal, S., One dimensional nanostructured materials. *Progress in Materials Science* **2007**, 52, (5), 699-913.
2. Reneker, D. H.; Chun, I., Nanometre diameter fibres of polymer, produced by electrospinning. *Nanotechnology* **1996**, 7, (3), 216-223.
3. Sun, Z.; Zussman, E.; Yarin, A. L.; Wendorff, J. H.; Greiner, A., Compound core-shell polymer nanofibers by co-electrospinning. *Advanced Materials* **2003**, 15, (22), 1929-1932.
4. Martin, C. R., Membrane-based synthesis of nanomaterials. *Chemistry of Materials* **1996**, 8, (8), 1739-1746.
5. Bognitzki, M.; Hou, H.; Ishaque, M.; Frese, T.; Hellwig, M.; Schwarte, C.; Schaper, A.; Wendorff, J. H.; Greiner, A., Polymer, metal, and hybrid nano- and mesotubes by coating degradable polymer template fibers (TUFT process). *Advanced Materials* **2000**, 12, (9), 637-640.
6. Joo, J.; Park, K. T.; Kim, B. H.; Kim, M. S.; Lee, S. Y.; Jeong, C. K.; Lee, J. K.; Park, D. H.; Yi, W. K.; Lee, S. H., Conducting polymer nanotube and nanowire synthesized by using nanoporous template: synthesis, characteristics, and applications. *Synthetic Metals* **2003**, 135, (136), 7-9.
7. Yang, X.; Zhu, Z.; Dai, T.; Lu, Y., Facile fabrication of functional polypyrrole nanotubes via a reactive self-degraded template. *Macromolecular Rapid Communications* **2005**, 26, (21), 1736-1740.
8. Shen, Y.; Wan, M., Tubular polypyrrole synthesized by in situ doping polymerization in the presence of organic function acids as dopants. *Journal of Polymer Science Part A Polymer Chemistry* **1999**, 37, (10), 1443-1450.
9. Formhals, A., Process and apparatus for preparing artificial threads. In Patent Number 1,975,504: 1934.
10. Vonnegut, B.; Neubauer, R. L., Production of monodisperse liquid particles by electrical atomization. *Journal of Colloid Science* **1952**, 7, (6), 616-622.
11. Simons, H. L., Process and apparatus for producing patterned nonwoven fabrics. *US Patent* **1966**, 3280229.
12. Ishizu, K.; Tsubaki, K.; Mori, A.; Uchida, S., Architecture of nanostructured polymers. *Progress in Polymer Science* **2003**, 28, (1), 27-54.
13. Huang, Z. M.; Zhang, Y. Z.; Kotaki, M.; Ramakrishna, S., A review on polymer nanofibers by electrospinning and their applications in nanocomposites. *Composites Science and Technology* **2003**, 63, (15), 2223-2253.
14. Frenot, A.; Chronakis, I. S., Polymer nanofibers assembled by electrospinning. *Current Opinion in Colloid & Interface Science* **2003**, 8, (1), 64-75.
15. Zhou, Y.; Freitag, M.; Hone, J.; Staii, C.; Johnson Jr, A. T.; Pinto, N. J.; MacDiarmid, A. G., Fabrication and electrical characterization of polyaniline-based nanofibers with diameter below 30 nm. *Applied Physics Letters* **2003**, 83, (18), 3800/3.
16. Aleshin, A. N., Polymer nanofibers and nanotubes: Charge transport and device applications in advanced materials. *Advanced Materials* **2006**, 18, (1), 17-27.
17. Bredas, J. L.; Street, G. B., Polarons, bipolarons, and solitons in conducting polymers. *Accounts of Chemical Research* **1985**, 18, (10), 309-315.

18. McCall, R. P.; Ginder, J. M.; Leng, J. M.; Ye, H. J.; Manohar, S. K.; Masters, J. G.; Asturias, G. E.; MacDiarmid, A. G.; Epstein, A. J., Spectroscopy and defect states in polyaniline. *Physical Review B* **1990**, 41, (8), 5202-5213.
19. Heeger, A. J.; Kivelson, S.; Schrieffer, J. R.; Su, W. P., Solitons in conducting polymers. *Reviews of Modern Physics* **1988**, 60, (3), 781-850.
20. Burroughes, J. H.; Bradley, D. D. C.; Brown, A. R.; Marks, R. N.; Mackay, K.; Friend, R. H.; Burns, P. L.; Holmes, A. B., Light-emitting diodes based on conjugated polymers. *Nature* **1990**, 347, (6293), 539-541.
21. N. S. Sariciftci, L. S., A. J. Heeger, F. Wudi, Photoinduced electron transfer from a conducting polymer to buckminster fullerene. *Science* **1992**, 258, (5087), 1474-1476.
22. McCullough, R. D., The chemistry of conducting polythiophenes. *Advanced Materials* **1998**, 10, (2), 93-116.
23. Heeney, M.; McCulloch, I., *Semiconducting polythiophenes for field-effect transistor devices in flexible electronics: synthesis and structure property relationships*. 2009; Vol. 11.
24. http://www.ict.kth.se/courses/IM2653/Lectures_and_seminars/Lecture_3.pdf.
25. McCullough, R. D.; Lowe, R. D., Enhanced electrical conductivity in regioselectively synthesized poly(3-alkylthiophenes). *Journal of Chemical Society, Chemical Communication* **1992**, 70-72.
26. Loewe, R. S.; Khersonsky, S. M.; McCullough, R. D., A simple method to prepare head-to-tail coupled, regioregular poly (3-alkylthiophenes) using grignard metathesis in Advanced materials. *Advanced Materials* **1999**, 11, (3), 250-253.
27. Loewe, R. S.; Ewbank, P. C.; Liu, J.; Zhai, L.; McCullough, R. D., Regioregular, head-to-tail coupled poly (3-alkylthiophenes) made easy by the GRIM method: Investigation of the reaction and the origin of regioselectivity. *Macromolecules* **2001**, 34, (13), 4324-4333.
28. Bao, Z.; Dodabalapur, A.; Lovinger, A. J., Soluble and processable regioregular poly (3 hexylthiophene) for thin film field effect transistor applications with high mobility. *Applied Physics Letters* **1996**, 69, (26), 4108/3.
29. Liu, J.; Arif, M.; Zou, J.; Khondaker, S. I.; Zhai, L., Controlling poly (3-hexylthiophene) crystal dimension: nanowhiskers and nanoribbons. *Macromolecules* **2009**, 42, (24), 9390-9393.
30. Niyogi, S.; Hamon, M. A.; Hu, H.; Zhao, B.; Bhowmik, P.; Sen, R.; Itkis, M. E.; Haddon, R. C., Chemistry of single-walled carbon nanotubes. *Accounts of Chemical Research* **2002**, 35, (12), 1105-1113.
31. Wallace, P. R., The band theory of graphite. *Physical Review* **1947**, 71, (9), 622-634.
32. Geim, A. K.; Novoselov, K. S., The rise of graphene. *Nature Materials* **2007**, 6, (3), 183-191.
33. Visscher, P. B.; Falicov, L. M., Dielectric screening in a layered electron gas. *Physical Review B* **1971**, 3, (8), 2541-2547.
34. Morozov, S. V.; Novoselov, K. S.; Schedin, F.; Jiang, D.; Firsov, A. A.; Geim, A. K., Two-dimensional electron and hole gases at the surface of graphite. *Physical Review B* **2005**, 72, (20), 201401/4.
35. Banerjee, S.; Sardar, M.; Gayathri, N.; Tyagi, A. K.; Raj, B., Conductivity landscape of highly oriented pyrolytic graphite surfaces containing ribbons and edges. *Physical Review B* **2005**, 72, (7), 075418/7.

36. Blodgett, K., Monomolecular films of fatty acids on glass. *Journal of the American Chemical Society* **1934**, 56, (2), 495.
37. Blodgett, K. B.; Langmuir, I., Built-Up Films of Barium Stearate and Their Optical Properties. *Physical Review* **1937**, 51, (11), 964-982.
38. Decher, G., Fuzzy nanoassemblies: Toward layered polymeric multicomposites. *Science* **1997**, 277, (5330), 1232-1237.
39. Wang, L. Y.; Wang, Z. Q.; Zhang, X.; Shen, J. C.; Chi, L. F.; Fuchs, H., A new approach for the fabrication of an alternating multilayer film of poly(4-vinylpyridine) and poly(acrylic acid) based on hydrogen bonding. *Macromolecule Rapid Communication* **1997**, 18, (6), 509-514.
40. Stockton, W. B.; Rubner, M. F., Molecular-level processing of conjugated polymers. 4. Layer-by-layer manipulation of polyaniline via hydrogen-bonding interactions. *Macromolecules* **1997**, 30, (9), 2717-2725.
41. Wang, F.; Ma, N.; Chen, Q.; Wang, W.; Wang, L., Halogen bonding as a new driving force for layer-by-layer assembly. *Langmuir* **2007**, 23, (19), 9540-9542.
42. Lee, H.; Kepley, L. J.; Hong, H. G.; Mallouk, T. E., Inorganic analogs of Langmuir-Blodgett films: adsorption of ordered zirconium 1,10-decanebisphosphonate multilayers on silicon surfaces. *Journal of the American Chemical Society* **1988**, 110, (2), 618-620.
43. Xiong, H. M.; Cheng, M. H.; Zhou, Z.; Zhang, X.; Shen, J. C., A New Approach to the Fabrication of a Self-Organizing Film of Heterostructured Polymer/Cu₂S Nanoparticles. *Advanced Materials* **1998**, 10, (7), 529-532.
44. Shimazaki, Y.; Mitsuishi, M.; Ito, S.; Yamamoto, M., Preparation of the layer-by-layer deposited ultrathin film based on the charge-transfer interaction. *Langmuir* **1997**, 13, (6), 1385-1387.
45. Anzai, J.; Kobayashi, Y.; Nakamura, N.; Nishimura, M.; Hoshi, T., Layer-by-layer construction of multilayer thin films composed of avidin and biotin-labeled poly (amine) s. *Langmuir* **1999**, 15, (1), 221-226.
46. Anzai, J.; Hoshi, T.; Nakamura, N., Construction of multilayer thin films containing avidin by a layer-by-layer deposition of avidin and poly (anion) s. *Langmuir* **2000**, 16, (15), 6306-6311.
47. Anzai, J.; Kobayashi, Y., Construction of multilayer thin films of enzymes by means of sugar-lectin interactions. *Langmuir* **2000**, 16, (6), 2851-2856.
48. Suzuki, I.; Egawa, Y.; Mizukawa, Y.; Hoshi, T.; Anzai, J., Construction of positively-charged layered assemblies assisted by cyclodextrin complexation. *Chemical Communications* **2002**, 2002, (2), 164-165.
49. Crespo-Biel, O.; Dordi, B.; Reinhoudt, D. N.; Huskens, J., Supramolecular layer-by-layer assembly: alternating adsorptions of guest-and host-functionalized molecules and particles using multivalent supramolecular interactions. *Journal of the American Chemical Society* **2005**, 127, (20), 7594-7600.
50. Ogawa, Y.; Arikawa, Y.; Kida, T.; Akashi, M., Fabrication of novel layer-by-layer assembly films composed of poly (lactic acid) and polylysine through cation- dipole interactions. *Langmuir* **2008**, 24, (16), 8606-8609.
51. Decher, G.; Hong, J. D.; Bunsen-Ges, B., Buildup of Ultrathin Multilayer Films by a Self-Assembly Process: II. Consecutive Adsorption of Anionic and Cationic Bipolar Amphiphiles and Polyelectrolytes on Charged Surfaces. *Physical Chemistry* **1991**, 95, (11), 1430-1434.

52. Cheng, J.; Fou, A. F.; Ferreira, A. C.; Rubner, M. F., *Polymer Preprint* **1993**, 34, 757.
53. Cheng, J. H.; Fou, A. F.; Rubner, M. F., Molecular self-assembly of conducting polymers. *Thin Solid films* **1994**, 244, (1-2), 985-989.
54. Ferreira, M.; Cheung, J. H.; Rubner, M. F., Molecular self-assembly of conjugated polyions: a new process for fabricating multilayer thin film heterostructures. *Thin Solid films* **1994**, 244, (1), 806-809.
55. Mendelsohn, J. D.; Barrett, C. J.; Chan, V. V.; Pal, A. J.; Mayes, A. M.; Rubner, M. F., Fabrication of microporous thin films from polyelectrolyte multilayers. *Langmuir* **2000**, 16, (11), 5017-5023.
56. Hiller, J.; Mendelsohn, J. D.; Rubner, M. F., Reversibly erasable nanoporous anti-reflection coatings from polyelectrolyte multilayers. *Nature Materials* **2002**, 1, (1), 59-63.
57. Zhai, L.; Nolte, A. J.; Cohen, R. E.; Rubner, M. F., pH-gated porosity transitions of polyelectrolyte multilayers in confined geometries and their application as tunable Bragg reflectors. *Macromolecules* **2004**, 37, (16), 6113-6123.
58. Berg, M. C.; Zhai, L.; Cohen, R. E.; Rubner, M. F., Controlled drug release from porous polyelectrolyte multilayers. *Biomacromolecules* **2006**, 7, (1), 357-364.
59. Lee, D.; Rubner, M. F.; Cohen, R. E., All-nanoparticle thin-film coatings. *Nano Letters* **2006**, 6, (10), 2305-2312.
60. Sandler, J. K. W.; Kirk, J. E.; Kinloch, I. A.; Shaffer, M. S. P.; Windle, A. H., Ultra-low electrical percolation threshold in carbon-nanotube-epoxy composites. *Polymer* **2003**, 44, (19), 5893-5899.
61. Sandler, J.; Shaffer, M. S. P.; Prasse, T.; Bauhofer, W.; Schulte, K.; Windle, A. H., Development of a dispersion process for carbon nanotubes in an epoxy matrix and the resulting electrical properties. *Polymer* **1999**, 40, (21), 5967-5971.
62. Osorio, A. G.; Silveira, I. C. L.; Bueno, V. L.; Bergmann, C. P., H₂SO₄/HNO₃/HCl—Functionalization and its effect on dispersion of carbon nanotubes in aqueous media. *Applied Surface Science* **2008**, 255, (5P1), 2485-2489.
63. Kim, M.; Hong, C. K.; Choe, S.; Shim, S. E., Synthesis of polystyrene brush on multiwalled carbon nanotubes treated with KMnO₄ in the presence of a phase-transfer catalyst. *Journal of Polymer Science, Part A, Polymer Chemistry* **2007**, 45, (19), 4413-4420.
64. Monthieux, M.; Smith, B. W.; Burteaux, B.; Claye, A.; Fischer, J. E.; Luzzi, D. E., Sensitivity of single-wall carbon nanotubes to chemical processing: an electron microscopy investigation. *Carbon* **2001**, 39, (8), 1251-1272.
65. Hamon, M. A.; Hui, H.; Bhowmik, P.; Itkis, H. M. E.; Haddon, R. C., Ester-functionalized soluble single-walled carbon nanotubes. *Applied Physics A: Materials Science & Processing* **2002**, 74, (3), 333/5.
66. Sun, Y. P.; Huang, W.; Lin, Y.; Fu, K.; Kitaygorodskiy, A.; Riddle, L. A.; Yu, Y. J.; Carroll, D. L., Soluble dendron-functionalized carbon nanotubes: preparation, characterization, and properties. *Chemistry of Materials* **2001**, 13, (9), 2864-2869.
67. Barraza, H. J.; Pompeo, F.; Edgar, A. O.; Resasco, D. E., SWNT-filled thermoplastic and elastomeric composites prepared by miniemulsion polymerization. *Nano Letters* **2002**, 2, (8), 797-802.

68. Islam, M. F.; Rojas, E.; Bergey, D. M.; Johnson, A. T.; Yodh, A. G., High weight fraction surfactant solubilization of single-wall carbon nanotubes in water. *Nano Letters* **2003**, 3, (2), 269-273.
69. Bandyopadhyaya, R.; Nativ-Roth, E.; Regev, O.; Yerushalmi-Rozen, R., Stabilization of individual carbon nanotubes in aqueous solutions. *Nano Letters* **2002**, 2, (1), 25-28.
70. Grunlan, J. C.; Liu, L.; Kim, Y. S., Tunable single-walled carbon nanotube microstructure in the liquid and solid states using poly (acrylic acid). *Nano Lett* **2006**, 6, (5), 911-915.
71. Nepal, D.; Geckeler, K. E., Proteins and carbon nanotubes: close encounter in water. *Small* **2007**, 3, (7), 1259.
72. Zheng, M.; Jagota, A.; Semke, E. D.; Diner, B. A.; Mclean, R. S.; Lustig, S. R.; Richardson, R. E.; Tassi, N. G., DNA-assisted dispersion and separation of carbon. *Nature Materials* **2003**, 2, (5), 338-342.
73. Baibarac, M.; Gomez-Romero, P., Nanocomposites based on conducting polymer and carbon nanotubes: From fancy materials to functional applications. *Journal of Nanoscience and Nanotechnology* **2006**, 6, (2), 289-302.
74. Kuila, B. K.; Malik, S.; Batabyal, S. K.; Nandi, A. K., In-situ syntheses of soluble poly(3-hexylthiophene)/multiwalled carbon nanotubes composite: Morphology, structure, and conductivity. *Macromolecules* **2007**, 40, (2), 278-287.
75. Peng, C.; Snook, G. A.; Fray, D. J.; Shaffer, M. S. P.; Chen, G. Z., Carbon nanotube stabilised emulsions for electrochemical synthesis of porous nanocomposite coatings of poly[3,4-ethylene-dioxythiophene]. *Chemical Communication* **2006**, 44, 4629-4631.
76. Star, A., Stoddart, J. F.; Steuerman, D.; Diehl, M.; Boukai, A.; Wong, E. W.; Yang, X.; Chung, S. W.; Choi, H.; Heath, J. R. , Preparation and properties of polymer-wrapped single-walled carbon nanotubes. *Angewandte Chemie International Edition* **2001**, 113, (9), 1771-1775.
77. Zengin, H.; Zhou, W.; Jin, J.; Czerw, R.; Smith, D. W.; Echegoyen, L.; Carroll, D. L.; Foulger, S. H.; Ballato, J., Carbon nanotubes doped polyaniline. *Advanced Materials* **2002**, 14, (20), 1480-1483.
78. Cheng, F.; Imin, P.; Maunders, C.; Botton, G.; Adronov, A., Soluble, discrete supramolecular complexes of single-walled carbon nanotubes with fluorine-based conjugated polymers. *Macromolecules* **2008**, 41, (7), 2304-2308.
79. Nativ-Roth, E.; Shvartzman-Cohen, R.; Bounioux, C.; Florent, M.; Zhang, D.; Szleifer, I.; Yerushalmi-Rozen, R., Physical adsorption of block copolymers to SWNT and MWNT: a nonwrapping mechanism. *Macromolecules* **2007**, 40, (10), 3676-3685.
80. Park, I.; Lee, W.; Kim, J.; Park, M.; Lee, H., Selective sequestering of multi-walled carbon nanotubes in self-assembled block copolymer. *Sensors and Actuators B: Chemical* **2007**, 126, (1), 301-305.
81. Mountrichas, G.; Tagmatarchis, N.; Pispas, S., Synthesis and solution behavior of carbon nanotubes decorated with amphiphilic block polyelectrolytes. *Journal of Physical Chemistry B* **2007**, 111, (29), 8369-8372.
82. Sinani, V. A.; Gheith, M. K.; Yaroslavov, A. A.; Rakhnyanskaya, A. A.; Sun, K.; Mamedov, A. A.; Wicksted, J. P.; Kotov, N. A., Aqueous dispersions of single-wall and multiwall carbon nanotubes with designed amphiphilic polycations. *Journal of the American Chemical Society* **2005**, 127, (10), 3463-3472.

83. Fukushima, H.; Drzal, L. T., A carbon nanotube alternative: Graphite nanoplatelets as reinforcements for polymers. *Annual Technical Conference of Society of Plastic Engineers* **2003**, 61, 2230-2234.
84. Kelly, B. T., Physics of Graphite. *Applied Science, London* **1981**, 475.
85. Kotov, N. A., Materials science: Carbon sheet solutions. *Nature* **2006**, 442, (7100), 254-255.
86. Kang, F. L., Y; Zhang, TY, Influences of H₂O₂ on synthesis of H₂SO₄ -GICs. *Journal of Physics and Chemistry of Solids* **1996**, 57, 889-892.
87. Kang, F.; Zhang, T. Y.; Leng, Y., Electrochemical behavior of graphite in electrolyte of sulfuric and acetic acid. *Carbon* **1997**, 35, (8), 1167-1173.
88. Pan, Y. X.; Yu, Z. Z.; Ou, Y. C.; Hu, G. H., A new process of fabricating electrically conducting nylon 6/graphite nanocomposites via intercalation polymerization. *Journal of Polymer Science Part B-Polymer Physics* **2000**, 38, (12), 1626-1633.
89. Li, J.; Li, M., Preparation of expandable graphite with ultrasound irradiation. *Materials Letters* **2007**, 61, (28), 5070-5073.
90. Li, X.; Zhang, G.; Bai, X.; Sun, X.; Wang, X.; Wang, E.; Dai, H., Highly conducting graphene sheets and Langmuir–Blodgett films. *Nature Nanotechnology* **2008**, 3, (9), 538-542.
91. Gilje, S.; Han, S.; Wang, M.; Wang, K. L.; Kaner, R. B., A chemical route to graphene for device applications. *Nano Letters* **2007**, 7, (11), 3394-3398.
92. Stankovich, S.; Dikin, D. A.; Dommett, G. H. B.; Kohlhaas, K. M.; Zimney, E. J.; Stach, E. A.; Piner, R. D.; Nguyen, S. T.; Ruoff, R. S., Graphene-based composite materials. *Nature* **2006**, 442, (7100), 282-286.
93. Verdejo, R.; Barroso-Bujans, F.; Rodriguez-Perez, M. A.; de Saja, J. A.; Lopez-Manchado, M. A., Functionalized graphene sheet filled silicone foam nanocomposites. *Journal of Materials Chemistry* **2008**, 18, (19), 2221-2226.
94. Schniepp, H. C.; Li, J. L.; McAllister, M. J.; Sai, H.; Herrera-Alonso, M.; Adamson, D. H.; Prud'homme, R. K.; Car, R.; Saville, D. A.; Aksay, I. A., Functionalized single graphene sheets derived from splitting graphite oxide. *Journal of Physical Chemistry B* **2006**, 110, (17), 8535-8539.
95. Gomez-Navarro, C.; Weitz, R. T.; Bittner, A. M.; Scolari, M.; Mews, A.; Burghard, M.; Kern, K., Electronic transport properties of individual chemically reduced graphene oxide sheets. *Nano Letters* **2007**, 7, (11), 3499-3503.
96. Staudenmaier, L., Verfahren zur darstellung der graphitsaure. *Ber Dtsch Chem Ges* **1898**, 31, 1481-1499.
97. Hummers W, O. R., Preparation of graphite oxide. *Journal of the American Chemical Society* **1958**, 80, (6), 1339.
98. Becerril, H. A.; Mao, J.; Liu, Z.; Stoltenberg, R. M.; Bao, Z.; Chen, Y., Evaluation of solution-processed reduced graphene oxide films as transparent conductors. *ACS Nano* **2008**, 2, (3), 463-470.
99. Xu, Y.; Bai, H.; Lu, G.; Li, C.; Shi, G., Flexible graphene films via the filtration of water soluble noncovalent functionalized graphene sheets. *Journal of the American Chemical Society* **2008**, 130, (18), 5856-5857.
100. Stankovich, S.; Dikin, D. A.; Piner, R. D.; Kohlhaas, K. A.; Kleinhammes, A.; Jia, Y.; Wu, Y.; Nguyen, S. T.; Ruoff, R. S., Synthesis of graphene-based nanosheets via chemical reduction of exfoliated graphite oxide. *Carbon* **2007**, 45, (7), 1558-1565.

101. Paredes, J. I.; Villar-Rodil, S.; Martinez-Alonso, A.; Tascon, J. M. D., Graphene oxide dispersion in organic solvents. *Langmuir* **2008**, *24*, (19), 10560–10564.
102. Li, D.; Muller, M. B.; Gilje, S.; Kaner, R. B.; Wallace, G. G., Processable aqueous dispersions of graphene nanosheets. *Nature Nanotechnology* **2008**, *3*, 101-105.
103. Stankovich, S.; Piner, R. D.; Chen, X. Q.; Wu, N. Q.; Nguyen, S. T.; Ruoff, R. S., Stable aqueous dispersions of graphitic nanoplatelets via the reduction of exfoliated graphite oxide in the presence of poly(sodium 4-styrenesulfonate). *Journal of Materials Chemistry* **2006**, *16*, (2), 155-158.
104. Athanasios B. Bourlinos, D. G., Dimitrios Petridis, Tamas Szabo, Anna Szeri, and Imre Dekany,, Graphite Oxide: Chemical Reduction to Graphite and Surface Modification with Aliphatic Amines and Amino Acids. *Langmuir* **2003**, *19*, 6050-6055.
105. Zalan, Z.; Lazar, I.; Fuleop, F., Chemistry of Hydrazinoalcohols and their Heterocyclic Derivatives. Part 1. Synthesis of Hydrazinoalcohols. *Current Organic Chemistry* **2005**, *9*, (4), 657-376.
106. Stankovich, S.; Piner, R. D.; Nguyen, S. B. T.; Ruoff, R. S., Synthesis and exfoliation of isocyanate-treated graphene oxide nanoplatelets. *Carbon* **2006**, *44*, (15), 3342-3347.
107. Dekany, I.; Kruger-Grasser, R.; Weiss, A., Selective liquid sorption properties of hydrophobized graphite oxide nanostructures *Colloids & Polymer Science* **1998**, *276*, (7), 570-576.
108. Kovtyukhova, N. I.; Karpenco, G. A.; Chuiko, A. A., Complexation of transition metal ion in aqueous suspensions of oxide-graphite. *Journal of Inorganic Chemistry* **1992**, *37*, (5), 1124-1129.
109. Liu, P.; Gong, K.; Xiao, P.; Xiao, M., Preparation and characterization of poly(vinylacetate)-intercalated graphite oxide nanocomposite. *Journal of Materials Chemistry* **2000**, *10*, 933-935.
110. Dubas, S. T.; Schlenoff, J. B., Factors controlling the growth of polyelectrolyte multilayers. *Macromolecules* **1999**, *32*, (24), 8153-8160.
111. Yoo, D.; Shiratori, S. S.; Rubner, M. F., Controlling bilayer composition and surface wettability of sequentially adsorbed multilayers of weak polyelectrolytes. *Macromolecules* **1998**, *31*, (13), 4309-4318.
112. Cho, J.; Caruso, F., Polymeric multilayer films comprising deconstructible hydrogen-bonded stacks confined between electrostatically assembled layers. *Macromolecules* **2003**, *36*, (8), 2845-2851.
113. Iwata, H.; Oodate, M.; Uyama, Y.; Amemiya, H.; Ikada, Y., Preparation of temperature-sensitive membranes by graft polymerization onto a porous membrane. *Journal of Membrane Science* **1991**, *55*, (1-2), 119-130.
114. Atencia, J.; Beebe, D. J., Controlled microfluidic interfaces. *Nature* **2004**, *437*, (7059), 648-655.
115. Senaratne, W.; Andruzzi, L.; Ober, C. K., Self-assembled monolayers and polymer brushes in biotechnology: current applications and future perspectives. *Biomacromolecules* **2005**, *6*, (5), 2427-2448.
116. Krupenkin, T. N.; Taylor, J. A.; Schneider, T. M.; Yang, S., From rolling ball to complete wetting: the dynamic tuning of liquids on nanostructured surfaces. *Langmuir* **2004**, *20*, (10), 3824-3827.

117. Sun, T.; Wang, G.; Feng, L.; Liu, B.; Ma, Y.; Jiang, L.; Zhu, D., Reversible switching between superhydrophilicity and superhydrophobicity. *Angewandte Chemie International Edition* **2004**, 43, (3), 357-360.
118. Chunder, A.; Etcheverry, K.; Londe, G.; Cho, H. J.; Zhai, L., Conformal switchable superhydrophobic/hydrophilic surfaces for microscale flow control. *Colloids and Surfaces A: Physicochemical and Engineering Aspects* **2008**, 333, (1-5), 187-193.
119. Ichimura, K.; Oh, S. K.; Nakagawa, M., Light-driven motion of liquids on a photoresponsive surface. *Science* **2000**, 288, (5471), 1624.
120. Lahann, J.; Mitragotri, S.; Tran, T. N.; Kaido, H.; Sundaram, J.; Choi, I. S.; Hoffer, S.; Somorjai, G. A.; Langer, R., A reversibly switching surface. *Science* **2003**, 299, (5605), 371.
121. Julthongpiput, D.; Lin, Y. H.; Teng, J.; Zubarev, E. R.; Tsukruk, V. V., Y-shaped polymer brushes: Nanoscale switchable surfaces. *Langmuir* **2003**, 19, (19), 7832-7836.
122. Heskins, M.; Guillet, J. E., Solution properties of poly (N-isopropylacrylamide). *Journal of Macromolecular Science, Part A* **1968**, 2, (8), 1441-1455.
123. Schild, H. G.; Tirrell, D. A., Microcalorimetric detection of lower critical solution temperatures in aqueous polymer solutions. *Journal of Physical Chemistry* **1990**, 94, (10), 4352-4356.
124. Quinn, J. F.; Caruso, F., Facile tailoring of film morphology and release properties using layer-by-layer assembly of thermoresponsive materials. *Langmuir* **2004**, 20, (1), 20-22.
125. Chunder, A.; Sarkar, S.; Yu, Y.; Zhai, L., Fabrication of ultrathin polyelectrolyte fibers and their controlled release properties. *Colloids and Surfaces B: Biointerfaces* **2007**, 58, (2), 172-179.
126. Glinel, K.; Dejugnat, C.; Prevot, M.; Scholer, B.; Schonhoff, M.; Klitzing, R. V., Responsive polyelectrolyte multilayers. *Colloids and Surfaces a-Physicochemical and Engineering Aspects* **2007**, 303, (1-2), 3-13.
127. Cebeci, F. C.; Wu, Z.; Zhai, L.; Cohen, R. E.; Rubner, M. F., Nanoporosity-driven superhydrophilicity: A means to create multifunctional antifogging coatings. *Langmuir* **2006**, 22, (6), 2856-2862.
128. Dittrich, P. S.; Manz, A., Lab-on-a-chip: microfluidics in drug discovery *Nature Reviews Drug Discovery* **2006**, 5, 210-218.
129. Martin, R. S.; Root, P. D.; Spence, D. M., Microfluidic technologies as platforms for performing quantitative cellular analyses in an in vitro environment. *Analyst* **2006**, 131, 1197-1206.
130. El-Ali, J.; Sorger, P. K.; Jensen, K. F., Cells on chips. *NATURE-LONDON-* **2006**, 442, (7101), 403.
131. Gatimu, E. N.; Sweedler, J. V.; Bohn, P. W., Nanofluidics and the role of nanocapillary array membranes in mass-limited chemical analysis. *The Analyst* **2006**, 131, (6), 705-709.
132. Song, H.; Chen, D. L.; Ismagilov, R. F., Reactions in droplets in microfluidic channels. *Angewandte Chemie (International ed. in English)* **2006**, 45, (44), 7336.
133. Oh, K. W.; Ahn, C. H., A review of microvalves. *Journal of Micromechanics and Microengineering* **2006**, 16, (5), 13.
134. Andersson, H.; van der Wijngaart, W.; Griss, P.; Niklaus, F.; Stemme, G., Hydrophobic valves of plasma deposited octafluorocyclobutane in DRIE channels. *Sensors & Actuators: B. Chemical* **2001**, 75, (1-2), 136-141.

135. Qing, Y.; Bauer, J. M.; Moore, J. S.; Beebe, D. J., Fabrication and characterization of a biomimetic hydrogel check valve. *IEEE-EMBS Special Topic Conference on Microtechnologies in Medicine & Biology* **2000**, 336-339.
136. Kim, D.; Beebe, D. J., A bi-polymer micro one-way valve. *Sensors & Actuators: A. Physical* **2007**, 136, (1), 426-433.
137. Craighead, H. G., Nanoelectromechanical systems. *Science* **2000**, 290, (5496), 1532.
138. Buchholz, B. A.; Doherty, E. A. S.; Albarghouthi, M. N.; Bogdan, F. M.; Zahn, J. M.; Barron, A. E., Microchannel DNA sequencing matrices with a thermally controlled "viscosity switch". *Analytical Chemistry* **2001**, 73, (2), 157-164.
139. Jacobs, H. O.; Tao, A. R.; Schwartz, A.; Gracias, D. H.; Whitesides, G. M., Fabrication of a cylindrical display by patterned assembly. *Science* **2002**, 296, (5566), 323.
140. Tsukruk, V. V., Assembly of supramolecular polymers in ultrathin films. *Progress in Polymer Science* **1997**, 22, (2), 247-311.
141. Jones, D. M.; Smith, J. R.; Huck, W. T. S.; Alexander, C., Variable adhesion of micropatterned thermoresponsive polymer brushes: AFM investigations of poly (N-isopropylacrylamide) brushes prepared by surface-initiated polymerizations. *Advanced Materials* **2002**, 14, (16), 1130.
142. Ista, L. K.; Perez-Luna, V. H.; Lopez, G. P., Surface-grafted, environmentally sensitive polymers for biofilm release. *Applied and Environmental Microbiology* **1999**, 65, (4), 1603.
143. Nath, N.; Chilkoti, A., Creating "Smart" Surfaces Using Stimuli Responsive Polymers. *Advanced Materials* **2002**, 14, (17), 1243-1247.
144. Russell, T. P., Surface-responsive materials. *Science* **2002**, 297, (5583), 964.
145. De Crevoisier, G.; Fabre, P.; Corpart, J. M.; Leibler, L., Switchable tackiness and wettability of a liquid crystalline polymer. *Science (New York, NY)* **1999**, 285, (5431), 1246.
146. Matthews, J. R.; Tuncel, D.; Jacobs, R. M. J.; Bain, C. D.; Anderson, H. L., Surfaces designed for charge reversal. *Journal of the American Chemical Society* **2003**, 125, (21), 6428-6433.
147. Kim, K.; Jeon, W. S.; Kang, J. K.; Lee, J. W.; Jon, S. Y.; Kim, T.; Kim, K., A pseudorotaxane on gold: formation of self-assembled monolayers, reversible dethreading and rethreading of the ring, and ion-gating behavior. *Angewandte Chemie International Edition* **2003**, 115, (20), 2395-2398.
148. Prins, M. W. J.; Welters, W. J. J.; Weekamp, J. W., Fluid control in multichannel structures by electrocapillary pressure. *Science* **2001**, 291, (5502), 277.
149. Byloos, M.; Al-Maznai, H.; Morin, M., Phase transitions of alkanethiol self-assembled monolayers at an electrified gold surface. *Journal of Physical Chemistry A* **2001**, 105, (25), 5900-5905.
150. Abbott, N. L.; Gorman, C. B.; Whitesides, G. M., Active control of wetting using applied electrical potentials and self-assembled monolayers. *Langmuir* **1995**, 11, (1), 16-18.
151. Lim, H.; Kwak, D. J. M.; Cho, K., Photoreversibly switchable superhydrophobic surface with erasable and rewritable pattern. *Journal of the American Chemical Society* **2006**, 128, (45), 14458-14459.
152. Chia, S.; Cao, J.; Stoddart, J. F.; Zink, J. I., Working Supramolecular Machines Trapped in Glass and Mounted on a Film Surface We thank the National Science Foundation and

- the Sandia National Laboratories for supporting this research. *Angewandte Chemie (International ed. in English)* **2001**, 40, (13), 2447.
153. Pertsin, A. J.; Grunze, M.; Kreuzer, H. J.; Wang, R. L. C., The effect of electrostatic fields on an oligo (ethylene glycol) terminated alkanethiol self-assembled monolayer. *Physical Chemistry Chemical Physics* **2000**, 2, (8), 1729-1733.
 154. Ballardini, R.; Balzani, V.; Credi, A.; Gandolfi, M. T.; Venturis, M., Artificial molecular-level machines: which energy to make them work? *Accounts of Chemical Research* **2001**, 34, (6), 445-455.
 155. Balzani, V.; Credi, A.; Raymo, F. M.; Stoddart, J. F., Artificial molecular machines. *Angewandte Chemie International Edition* **2000**, 39, (19), 3349–3391.
 156. Decher, G., Fuzzy nanoassemblies: toward layered polymeric multicomposites. *Science* **1997**, 277, (5330), 1232.
 157. Yang, S. Y.; Rubner, M. F., Micropatterning of polymer thin films with pH-sensitive and cross-linkable hydrogen-bonded polyelectrolyte multilayers. *Journal of the American Chemical Society* **2002**, 124, (10), 2100-2101.
 158. Sukhishvili, S. A.; Granick, S., Layered, erasable polymer multilayers formed by hydrogen-bonded sequential self-assembly. *Macromolecules* **2002**, 35, (1), 301-310.
 159. Yam, C. M.; Kakkar, A. K., Molecular Self-Assembly of Dihydroxy-Terminated Molecules via Acid-Base Hydrolytic Chemistry on Silica Surfaces: Step-by-Step Multilayered Thin Film Construction. *Langmuir* **1999**, 15, (11), 3807-3815.
 160. Li, D.; Jiang, Y.; Li, C.; Wu, Z.; Chen, X.; Li, Y., Self-assembly of polyaniline/polyacrylic acid films via acid-base reaction induced deposition. *Polymer* **1999**, 40, (25), 7065-70.
 161. Zhai, L.; Berg, M. C.; Cebeci, F. C.; Kim, Y.; Milwid, J. M.; Rubner, M. F.; Cohen, R. E., Patterned superhydrophobic surfaces: Toward a synthetic mimic of the Namib Desert beetle. *Nano Letters* **2006**, 6, (6), 1213-1217.
 162. Zhai, L.; Cebeci, F. C.; Cohen, R. E.; Rubner, M. F., Stable superhydrophobic coatings from polyelectrolyte multilayers. *Nano Letters* **2004**, 4, (7), 1349-1353.
 163. Jisr, R. M.; Rmaile, H. H.; Schlenoff, J. B., Hydrophobic and ultrahydrophobic multilayer thin films from perfluorinated polyelectrolytes. *Angewandte Chemie International Edition* **2005**, 44, (5), 782-785.
 164. Good, R. J.; Koo, M. N., The effect of drop size on contact angle. *Journal of Colloid and Interface Science* **1979**, 71, (2), 283-292.
 165. Murr, L. E.; Myers, M. S., *Interfacial phenomena in metals and alloys*. Addison Wesley Publishing Company Reading, MA: 1976.
 166. Wenzel, R. N., Surface roughness and contact angle. *Journal of Physics Colloidal Chemistry* **1949**, 53, 1466–1467.
 167. Wenzel, R. N., Resistance of solid surfaces to wetting by water. *Industrial & Engineering Chemistry* **1936**, 28, (8), 988-994.
 168. Cassie, A. B. D.; Baxter, S., Wettability of porous surfaces. *Transactions of the Faraday Society* **1944**, 40, 546-551.
 169. Schild, H. G., Poly(N-isopropylacrylamide): experiment, theory and application. *Progress in Polymer Science* **1992**, 17, (2), 163-249.
 170. Li, G.; Shi, L.; An, Y.; Zhang, W.; Ma, R., Double-responsive core–shell–corona micelles from self-assembly of diblock copolymer of poly (t-butyl acrylate-co-acrylic acid)-b-poly (N-isopropylacrylamide). *Polymer* **2006**, 47, (13), 4581-4587.

171. Kuckling, D.; Adler, H. J. P.; Arndt, K. F.; Ling, L.; Habicher, W. D., Temperature and pH dependent solubility of novel poly (N-isopropylacrylamide) copolymers. *Macromolecular Chemistry and Physics* **2000**, 201, (2), 273-280.
172. Huang, J.; Wu, X. Y., Effects of pH, salt, surfactant and composition on phase transition of poly (NIPAm/MAA) nanoparticles. *Journal of Polymer Science Part A Polymer Chemistry* **1999**, 37, (14), 2667-2676.
173. Bravo, J.; Zhai, L.; Wu, Z.; Cohen, R. E.; Rubner, M. F., Transparent superhydrophobic films based on silica nanoparticles. *Langmuir* **2007**, 23, (13), 7293-7298.
174. Ista, L. K.; Mendez, S.; Perez-Luna, V. H.; Lopez, G. P., Synthesis of poly (N-isopropylacrylamide) on initiator-modified self-assembled monolayers. *Langmuir* **2001**, 17, (9), 2552-2555.
175. Londe, G.; Chunder, A.; Zhai, L.; Cho, H. J., An analytical model for the wettability switching characteristic of a nanostructured thermoresponsive surface. *Applied Physics Letters* **2009**, 94, (16), 164104/3.
176. Londe, G.; Chunder, A.; Wesser, A.; Zhai, L.; Cho, H. J., Microfluidic valves based on superhydrophobic nanostructures and switchable thermosensitive surface for lab-on-a-chip (LOC) systems. *Sensors & Actuators: B. Chemical* **2008**, 132, (2), 431-438.
177. G. Londe, A. C., A. Wesser, L. Zhai, H. J. Cho, A Nanostructured thermosensitive smart surface with integrated microheater for wettability control. *Proceedings of IMECE2008 ASME International Mechanical Engineering Congress and Exposition* **2008**.
178. Hecht, E., *Optics Addison-Wesley, London* **1987**.
179. Jacobsson, R., Inhomogeneous and coevaporated homogeneous films for optical applications. *Physics Thin Film* **1975**, 8, 51-98.
180. Dobrowolski, J. A.; Panchhi, P.; High, M., AR coatings designed for two different infrared substrates. *Applied Optics* **1996**, 35, 102-105.
181. Dobrowolski, J. A.; Tikhonravov, A. V.; Trubetskov, M. K.; Sullivan, B. T.; Verly, P. G., Optimal single-band normal-incidence antireflection coatings. *Applied Optics* **1996**, 35, (4), 644-658.
182. Clapham, P. B.; Hutley, M. C., Reduction of lens reflection by moth eye principle. *Nature* **1973**, 244, (5414), 281-282.
183. Mohan, S.; Krishna, M. G., A Review of ion-beam-assisted deposition of optical thin films. *Vacuum* **1995**, 46, (7), 645-659.
184. Green, J. E., Low energy ion bombardment during film deposition from the vapor phase: effects on microstructure and microchemistry. *Solid State Technology* **1987**, 14, 115-122.
185. Pongratz, S.; Zoller, A., Plasma assisted deposition-A promising technique for optical coatings. *Journal of Vacuum Science & Technology a-Vacuum Surfaces and Films* **1992**, 10, (4), 1897-1904.
186. Xu, Y.; Fan, W. H.; Wu, D.; Sun, Y. H., Sol-gel broadband antireflective single-layer silica films with high laser damage threshold. *Thin Solid films* **2003**, 440, (1-2), 180-183.
187. Uhlmann, D. R.; Suratwala, T.; Davidson, K.; Boulton, J. M.; Teowee, G., Sol-gel derived coatings on glass. *Journal of Non-Crystalline Solids* **1997**, 218, 113-122.
188. Yam, C. M.; Kakkar, A. K., Molecular self-assembly of dihydroxy-terminated molecules via acid-base hydrolytic chemistry on silica surfaces: Step-by-step multilayered thin film construction. *Langmuir* **1999**, 15, (11), 3807-3815.

189. Cebeci, F. C.; Wu, Z. Z.; Zhai, L.; Cohen, R. E.; Rubner, M. F., Nanoporosity-driven superhydrophilicity: A means to create multifunctional antifogging coatings. *Langmuir* **2006**, *22*, (6), 2856-2862.
190. Lu, C. H.; Donch, I.; Nolte, M.; Fery, A., Au nanoparticle-based multilayer ultrathin films with covalently linked nanostructures: Spraying layer-by-layer assembly and mechanical property characterization. *Chemistry of Materials* **2006**, *18*, (26), 6204-6210.
191. Schulz, U.; Lau, K.; Kaiser, N., Antireflection coating with UV-protective properties for polycarbonate. *Applied Optics* **2008**, *47*, (13), C83-C87.
192. Li, C. H.; Wilkes, G. L., The mechanism for 3-aminopropyltriethoxysilane to strengthen the interface of polycarbonate substrates with hybrid organic-inorganic sol-gel coatings. *Journal of Inorganic and Organometallic Polymers* **1998**, *8*, (1), 33-45.
193. Gemici, Z.; Shimomura, H.; Cohen, R. E.; Rubner, M. F., Hydrothermal treatment of nanoparticle thin films for enhanced mechanical durability. *Langmuir* **2008**, *24*, (5), 2168-2177.
194. Uhrich, K. E.; Cannizzaro, S. M.; Langer, R. S.; Shakesheff, K. M., Polymeric systems for controlled drug release. *Chemical Reviews* **1999**, *99*, (11), 3181-3198.
195. Choi, C.; Chae, S. Y.; Nah, J. W., Thermosensitive poly(N-isopropylacrylamide)-b-poly(epsilon-caprolactone) nanoparticles for efficient drug delivery system. *Polymer* **2006**, *47*, (13), 4571-4580.
196. Joralemon, M. J.; Murthy, K. S.; Remsen, E. E.; Becker, M. L.; Wooley, K. L., Synthesis, characterization, and bioavailability of mannosylated shell cross-linked nanoparticles. *Biomacromolecules* **2004**, *5*, (3), 903-913.
197. Savic, R.; Luo, L. B.; Eisenberg, A.; Maysinger, D., Micellar nanocontainers distribute to defined cytoplasmic organelles. *Science* **2003**, *300*, (5619), 615-618.
198. Kost, J.; Langer, R., Equilibrium swollen hydrogels in controlled release applications. *Hydro. Medical Pharma* **1987**, *3*, 95-135.
199. Andrianov, A. K.; Cohen, S.; Visscher, K. B.; Payne, L. G.; Allcock, H. R.; Langer, R., Controlled release using ionotropic polyphosphazene hydrogels. *Journal of Controlled Release* **1993**, *27*, (1), 69-77.
200. Guiseppi-Elie, A.; Brahim, S. I.; Narinesingh, D., A chemically synthesized artificial pancreas: Release of insulin from glucose-responsive hydrogels. *Advanced Materials* **2002**, *14*, (10), 743-746.
201. Kajiwar, K.; Rossmurphy, S. B., Polymers-synthetic gels on the move. *Nature* **1992**, *355*, (6357), 208-209.
202. Law, B.; Weissleder, R.; Tung, C. H., Peptide-based biomaterials for protease-enhanced drug delivery. *Biomacromolecules* **2006**, *7*, (4), 1261-1265.
203. Li, J.; Li, X.; Ni, X. P.; Wang, X.; Li, H. Z.; Leong, K. W., Self-assembled supramolecular hydrogels formed by biodegradable PEO-PHB-PEO triblock copolymers and alpha-cyclodextrin for controlled drug delivery. *Biomaterials* **2006**, *27*, (22), 4132-4140.
204. Serizawa, T.; Matsukuma, D.; Akashi, M., Loading and release of charged dyes using ultrathin hydrogels. *Langmuir* **2005**, *21*, (17), 7739-7742.
205. Allouche, J.; Boissiere, M.; Helary, C.; Livage, J.; Coradin, T., Biomimetic core-shell gelatine/silica nanoparticles: A new example of biopolymer-based nanocomposites. *Journal of Materials Chemistry* **2006**, *16*, (30), 3120-3125.

206. Chauvierre, C.; Vauthier, C.; Labarre, D.; Couvreur, P.; Marden, M. C.; Leclerc, L., A new generation of polymer nanoparticles for drug delivery. *Cellular and Molecular Biology* **2004**, 50, (3), 233-239.
207. Huo, Q. S.; Liu, J.; Wang, L. Q.; Jiang, Y. B.; Lambert, T. N.; Fang, E., A new class of silica cross-linked micellar core-shell nanoparticles. *Journal of the American Chemical Society* **2006**, 128, (19), 6447-6453.
208. Steinhauser, I.; Spankuch, B.; Strebhardt, K.; Langer, K., Trastuzumab-modified nanoparticles: Optimisation of preparation and uptake in cancer cells. *Biomaterials* **2006**, 27, (28), 4975-4983.
209. Allouche, J.; Boissière, M.; Hélarly, C.; Livage, J.; Coradin, T., Biomimetic core-shell gelatine/silica nanoparticles: a new example of biopolymer-based nanocomposites. *Journal of Materials Chemistry* **2006**, 16, (30), 3120-3125.
210. Zur Muhlen, A.; Schwarz, C.; Mehnert, W., Solid lipid nanoparticles (SLN) for controlled drug delivery—drug release and release mechanism. *European Journal of Pharmaceutics and Biopharmaceutics* **1998**, 45, (2), 149-155.
211. Chew, S. Y.; Wen, J.; Yim, E. K. F.; Leong, K. W., Sustained release of proteins from electrospun biodegradable fibers. *Biomacromolecules* **2005**, 6, (4), 2017-2024.
212. Jia, H. F.; Zhu, G. Y.; Vugrinovich, B.; Kataphinan, W.; Reneker, D. H.; Wang, P., Enzyme-carrying polymeric nanofibers prepared via electrospinning for use as unique biocatalysts. *Biotechnology Progress* **2002**, 18, (5), 1027-1032.
213. Luong-Van, E.; Grondahl, L.; Chua, K. N.; Leong, K. W.; Nurcombe, V.; Cool, S. M., Controlled release of heparin from poly(epsilon-caprolactone) electrospun fibers. *Biomaterials* **2006**, 27, (9), 2042-2050.
214. Zhang, Y. Z.; Wang, X.; Feng, Y.; Li, J.; Lim, C. T.; Ramakrishna, S., Coaxial Electrospinning of (Fluorescein Isothiocyanate-Conjugated Bovine Serum Albumin)-Encapsulated Poly ([epsilon]-caprolactone) Nanofibers for Sustained Release. *Biomacromolecules* **2006**, 7, (4), 1049-1057.
215. Cui, W. G.; Li, X. H.; Zhu, X. L.; Yu, G.; Zhou, S. B.; Weng, J., Investigation of drug release and matrix degradation of electrospun poly(DL-lactide) fibers with paracetamol inoculation. *Biomacromolecules* **2006**, 7, (5), 1623-1629.
216. Dalton, P. D.; Klinkhammer, K.; Salber, J.; Klee, D.; Moller, M., Direct in vitro electrospinning with polymer melts. *Biomacromolecules* **2006**, 7, (3), 686-690.
217. Verreck, G.; Chun, I.; Rosenblatt, J.; Peeters, J.; Dijck, A. V.; Mensch, J.; Noppe, M.; Brewster, M. E., Incorporation of drugs in an amorphous state into electrospun nanofibers composed of a water-insoluble, nonbiodegradable polymer. *Journal of Controlled Release* **2003**, 92, (3), 349-360.
218. Katti, D. S.; Robinson, K. W.; Ko, F. K.; Laurencin, C. T., Bioresorbable nanofiber-based systems for wound healing and drug delivery: Optimization of fabrication parameters. *Journal of Biomedical Materials Research Part B-Applied Biomaterials* **2004**, 70B, (2), 286-296.
219. Rho, K. S.; Jeong, L.; Lee, G.; Seo, B. M.; Park, Y. J.; Hong, S. D.; Roh, S.; Cho, J. J.; Park, W. H.; Min, B. M., Electrospinning of collagen nanofibers: Effects on the behavior of normal human keratinocytes and early-stage wound healing. *Biomaterials* **2006**, 27, (8), 1452-1461.
220. Li, D.; Xia, Y. N., Electrospinning of nanofibers: Reinventing the wheel? *Advanced Materials* **2004**, 16, (14), 1151-1170.

221. Shin, Y. M.; Hohman, M. M.; Brenner, M. P.; Rutledge, G. C., Electrospinning: A whipping fluid jet generates submicron polymer fibers. *Applied Physics Letters* **2001**, 78, (8), 1149/3.
222. Li, J. X.; He, A. H.; Han, C. C.; Fang, D. F.; Hsiao, B. S.; Chu, B., Electrospinning of hyaluronic acid (HA) and HA/gelatin blends. *Macromolecular Rapid Communications* **2006**, 27, (2), 114-120.
223. Li, L.; Hsieh, Y. L., Chitosan bicomponent nanofibers and nanoporous fibers. *Carbohydrate Research* **2006**, 341, (3), 374-381.
224. Li, L.; Hsieh, Y. L., Ultra-fine polyelectrolyte fibers from electrospinning of poly(acrylic acid). *Polymer* **2005**, 46, (14), 5133-5139.
225. Son, W. K.; Youk, J. H.; Lee, T. S.; Park, W. H., The effects of solution properties and polyelectrolyte on electrospinning of ultrafine poly(ethylene oxide) fibers. *Polymer* **2004**, 45, (9), 2959-2966.
226. Zeng, J.; Aigner, A.; Czubyko, F.; Kissel, T.; Wendorff, J. H.; Greiner, A., Poly (vinyl alcohol) nanofibers by electrospinning as a protein delivery system and the retardation of enzyme release by additional polymer coatings. *Biomacromolecules* **2005**, 6, (3), 1484-1488.
227. Chung, A. J.; Rubner, M. F., Methods of loading and releasing low molecular weight cationic molecules in weak polyelectrolyte multilayer films. *Langmuir* **2002**, 18, (4), 1176-1183.
228. Vazquez, E.; Dewitt, D. M.; Hammond, P. T.; Lynn, D. M., Construction of hydrolytically-degradable thin films via layer-by-layer deposition of degradable polyelectrolytes. *Journal of the American Chemical Society* **2002**, 124, (47), 13992-13993.
229. Peyratout, C. S.; Dahne, L., Tailor-made polyelectrolyte microcapsules: From multilayers to smart containers. *Angewandte Chemie-International Edition* **2004**, 43, (29), 3762-3783.
230. Qiu, X. P.; Leporatti, S.; Donath, E.; Mohwald, H., Studies on the drug release properties of polysaccharide multilayers encapsulated ibuprofen microparticles. *Langmuir* **2001**, 17, (17), 5375-5380.
231. Malaisamy, R.; Bruening, M. L., High-flux nanofiltration membranes prepared by adsorption of multilayer polyelectrolyte membranes on polymeric supports. *Langmuir* **2005**, 21, (23), 10587-10592.
232. Miller, M. D.; Bruening, M. L., Correlation of the swelling and permeability of polyelectrolyte multilayer films. *Chemistry of Materials* **2005**, 17, (21), 5375-5381.
233. Rmaile, H. H.; Farhat, T. R.; Schlenoff, J. B., H-P-gated permeability of variably charged species through polyelectrolyte multilayer membranes. *Journal of Physical Chemistry B* **2003**, 107, (51), 14401-14406.
234. Ai, H.; Jones, S. A.; de Villiers, M. M.; Lvov, Y. M., Nano-encapsulation of furosemide microcrystals for controlled drug release. *Journal of Controlled Release* **2003**, 86, (1), 59-68.
235. De Geest, B. G.; Jonas, A. M.; Demeester, J.; De Smedt, S. C., Glucose-responsive polyelectrolyte capsules. *Langmuir* **2006**, 22, (11), 5070-5074.
236. Ma, Y. J.; Dong, W. F.; Hempenius, M. A.; Mohwald, H.; Vancso, G. J., Redox-controlled molecular permeability of composite-wall microcapsules. *Nature Materials* **2006**, 5, (9), 724-729.

237. Pargaonkar, N.; Lvov, Y. M.; Li, N.; Steenekamp, J. H.; de Villiers, M. M., Controlled release of dexamethasone from microcapsules produced by polyelectrolyte layer-by-layer nanoassembly. *Pharmaceutical Research* **2005**, *22*, (5), 826-835.
238. Shi, X. Y.; Caruso, F., Release behavior of thin-walled microcapsules composed of polyelectrolyte multilayers. *Langmuir* **2001**, *17*, (6), 2036-2042.
239. Chavasit, V.; Kienzlesterzer, C.; Torres, J. A., Formation and characterization of an insoluble polyelectrolyte complex: chitosan-polyacrylic acid. *Polymer Bulletin* **1988**, *19*, (3), 223-230.
240. Petrov, A. I.; Antipov, A. A.; Sukhorukov, G. B., Base-acid equilibria in polyelectrolyte systems: From weak polyelectrolytes to interpolyelectrolyte complexes and multilayered polyelectrolyte shells. *Macromolecules* **2003**, *36*, (26), 10079-10086.
241. Shiratori, S. S.; Rubner, M. F., pH-dependent thickness behavior of sequentially adsorbed layers of weak polyelectrolytes. *Macromolecules* **2000**, *33*, (11), 4213-4219.
242. Harris, J. J.; DeRose, P. M.; Bruening, M. L., Synthesis of passivating, nylon-like coatings through cross-linking of ultrathin polyelectrolyte films. *Journal of the American Chemical Society* **1999**, *121*, (9), 1978-1979.
243. Antipov, A. A.; Sukhorukov, G. B.; Donath, E.; Mohwald, H., Sustained release properties of polyelectrolyte multilayer capsules. *Journal of Physical Chemistry B* **2001**, *105*, (12), 2281-2284.
244. Shirai, M.; Nagatsuka, T.; Tanaka, M., Interaction between dyes and polyelectrolytes & effect of polyanions on mixed dimer formation of cationic dyes. *Makromolekulare Chemie-Macromolecular Chemistry and Physics* **1978**, *179*, (1), 173-179.
245. Baker, R., Controlled release of biologically active agents. *John Wiley & Sons, NY* **1987**.
246. Bromberg, L., Properties of aqueous solutions and gels of poly(ethylene oxide)-b-poly(propylene oxide)-b-poly(ethylene oxide)-g-poly(acrylic acid). *Journal of Physical Chemistry B* **1998**, *102*, (52), 10736-10744.
247. Choi, J.; Rubner, M. F., Influence of the degree of ionization on weak polyelectrolyte multilayer assembly. *Macromolecules* **2005**, *38*, (1), 116-124.
248. Philippova, O. E.; Hourdet, D.; Audebert, R.; Khokhlov, A. R., pH-responsive gels of hydrophobically modified poly(acrylic acid). *Macromolecules* **1997**, *30*, (26), 8278-8285.
249. Gothelf, K. V.; Larsen, A. G., Attachment of alkyltrichlorosilanes to the terminal 3,5-dihydroxyphenyl moiety of a self-assembled thiol monolayer on gold. *Journal of Colloid and Interface Science* **2002**, *255*, (2), 356-362.
250. Huang, J.; Wu, X. Y., Effects of pH, salt, surfactant and composition on phase transition of poly(NIPAm/MAA) nanoparticles. *Journal of Polymer Science Part a-Polymer Chemistry* **1999**, *37*, (14), 2667-2676.
251. Tadanaga, K.; Katata, N.; Minami, T., Formation process of super-water-repellent Al₂O₃ coating films with high transparency by the Sol-Gel method. *Journal of the American Ceramic Society* **1997**, *80*, (12), 3213-3216.
252. Murase, H.; Nanishi, K.; Kogure, H.; Fujibayashi, T.; Tamura, K.; Haruta, N., Interactions between heterogeneous surfaces of polymers and water. *Journal of Applied Polymer Science* **1994**, *54*, (13), 2051-2062.
253. Nakajima, A.; Abe, K.; Hashimoto, K.; Watanabe, T., Preparation of hard super-hydrophobic films with visible light transmission. *Thin Solid Films* **2000**, *376*, (1-2), 140-143.

254. Takeda, K.; Sasaki, M.; Kieda, N.; Katayama, K.; Kako, T.; Hashimoto, K.; Watanabe, T.; Nakajima, A., Preparation of transparent super-hydrophobic polymer film with brightness enhancement property. *Journal of Materials Science Letters* **2001**, 20, (23), 2131-2133.
255. Ferrari, M.; Ravera, F.; Rao, S.; Liggieri, L., Surfactant adsorption at superhydrophobic surfaces. *Applied Physics Letters* **2006**, 89, (5), 053104/3.
256. Mohammadi, R.; Wassink, J.; Amirfazli, A., Effect of surfactants on wetting of superhydrophobic surfaces. *Langmuir* **2004**, 20, (22), 9657-9662.
257. Marmur, A., Underwater superhydrophobicity: theoretical feasibility. *Langmuir* **2006**, 22, (4), 1400-1402.
258. Starov, V. M.; Kosvintsev, S. R.; Velarde, M. G., Spreading of surfactant solutions over hydrophobic substrates. *Journal of Colloid and Interface Science* **2000**, 227, (1), 185-190.
259. Lee, K. S.; Ivanova, N.; Starov, V. M.; Hilal, N.; Dutschk, V., Kinetics of wetting and spreading by aqueous surfactant solutions. *Advances in Colloid and Interface Science* **2008**, 144, (1-2), 54-65.
260. Novoselov, K. S.; Geim, A. K.; Morozov, S. V.; Jiang, D.; Zhang, Y.; Dubonos, S. V.; Grigorieva, I. V.; Firsov, A. A., Electric field effect in atomically thin carbon films. *Science* **2004**, 306, (5696), 666.
261. Jung, I.; Dikin, D. A.; Piner, R. D.; Ruoff, R. S., Tunable electrical conductivity of individual graphene oxide sheets reduced at "low" temperatures. *Nano Letters* **2008**, 8, (12), 4283-4287.
262. Liang, Y.; Wu, D.; Feng, X.; Mullen, K., Dispersion of graphene sheets in organic solvent supported by ionic interactions. *Advanced Materials* **2009**, 21, (17), 1679-1683.
263. Veca, L. M.; Lu, F.; Mezziani, M. J.; Cao, L.; Zhang, P.; Qi, G.; Qu, L.; Shrestha, M.; Sun, Y. P., Polymer functionalization and solubilization of carbon nanosheets. *Chemical Communications* **2009**, 2009, (18), 2565-2567.
264. Kudin, K. N.; Ozbas, B.; Schniepp, H. C.; Prud'Homme, R. K.; Aksay, I. A.; Car, R., Raman spectra of graphite oxide and functionalized graphene sheets. *Nano Letters* **2008**, 8, (1), 36-41.
265. Park, S.; Ruoff, R. S., Chemical methods for the production of graphenes. *Nature Nanotechnology* **2009**, 4, (4), 217-224.
266. Wang, X.; Zhi, L.; Tsao, N.; Tomovi, Z.; Li, J.; Müllen, K., Transparent carbon films as electrodes in organic solar cells. *Angewandte Chemie (International edition in English)* **2008**, 47, (16), 2990.
267. Wang, X.; Zhi, L.; Müllen, K., Transparent, conductive graphene electrodes for dye-sensitized solar cells. *Nano Letters* **2008**, 8, (1), 323.
268. Wehling, T. O.; Novoselov, K. S.; Morozov, S. V.; Vdovin, E. E.; Katsnelson, M. I.; Geim, A. K.; Lichtenstein, A. I., Molecular doping of graphene. *Nano Letters* **2008**, 8, (1), 173-177.
269. Das, A.; Pisana, S.; Chakraborty, B.; Piscanec, S.; Saha, S. K.; Waghmare, U. V.; Novoselov, K. S.; Krishnamurthy, H. R.; Geim, A. K.; Ferrari, A. C.; Sood, A. K., Monitoring dopants by raman scattering in an electrochemically top-gated graphene transistor. *Nature Nanotechnology* **2008**, 3, 210-215.
270. Su, Q.; Pang, S.; Alijani, V.; Li, C.; Feng, X.; Mullen, K., Composites of graphene with large aromatic molecules. *Advanced Functional Materials* **2009**, 21, (31), 3191-3195.

271. Tasis, D.; Tagmatarchis, N.; Bianco, A.; Prato, M., Chemistry of carbon nanotubes. *Chemical Reviews* **2006**, 106, (3), 1105-1136.
272. Berson, S.; De Bettignies, R.; Bailly, S.; Guillerez, S., Poly (3-hexylthiophene) fibers for photovoltaic applications. *Advanced Functional Materials* **2007**, 17, (8), 1377.
273. Li, G.; Shrotriya, V.; Huang, J.; Yao, Y.; Moriarty, T.; Emery, K.; Yang, Y., High-efficiency solution processable polymer photovoltaic cells by self-organization of polymer blends. *Nature Materials* **2005**, 4, (11), 864-868.
274. Reyes-Reyes, M.; Kim, K.; Dewald, J.; Lopez-Sandoval, R.; Avadhanula, A.; Curran, S.; Carroll, D. L., Meso-structure formation for enhanced organic photovoltaic cells. *Organic Letters* **2005**, 7, (26), 5749-5752.
275. Geng, H. Z.; Kim, K. K.; So, K. P.; Lee, Y. S.; Chang, Y.; Lee, Y. H., Effect of acid treatment on carbon nanotube-based flexible transparent conducting films. *Journal of the American Chemical Society* **2007**, 129, (25), 7758-7759.
276. Chen, H.; Muthuraman, H.; Stokes, P.; Zou, J.; Liu, X.; Wang, J.; Huo, Q.; Khondaker, S. I.; Zhai, L., Dispersion of carbon nanotubes and polymer nanocomposite fabrication using trifluoroacetic acid as a co-solvent. *Nanotechnology* **2007**, 18, (41), 415606.
277. Liu, J. Z., J. Zhai, L., Bottom up assembly of poly(3-hexylthiophene) on carbon nanotubes: 2D building blocks for nanoscale circuits. *Macromolecule Rapid Communication* **2009**, 30, (16), 1387-1391.
278. Samitsu, S.; Shimomura, T.; Heike, S.; Hashizume, T.; Ito, K., Effective production of poly (3-alkylthiophene) nanofibers by means of whisker method using anisole solvent: structural, optical, and electrical properties. *Macromolecules* **2008**, 41, (21), 8000-8010.
279. Ihn, K. J.; Moulton, J.; Smith, P., Whiskers of poly (3-alkylthiophene) *Journal of Polymer Science Part B Polymer Physics* **1993**, 31, (6), 735-735.
280. Meille, S. V.; Romita, V.; Caronna, T.; Lovinger, A. J.; Catellani, M.; Belobrzeckaja, L., Influence of molecular weight and regioregularity on the polymorphic behavior of poly (3-decylthiophenes). *Macromolecules* **1997**, 30, (25), 7898-7905.
281. Tashiro, K.; Kobayashi, M.; Kawai, T.; Yoshino, K., Crystal structure change in poly (3-alkyl thiophene) s induced by iodine doping as studied by an organized combination of X-ray diffraction, infrared/Raman spectroscopy and computer simulation techniques. *Polymer* **1997**, 38, (12), 2867-79.
282. Brinkmann, M.; Rannou, P., Effect of molecular weight on the structure and morphology of oriented thin films of regioregular poly (3-hexylthiophene) grown by directional epitaxial solidification. *Advanced Functional Materials* **2007**, 17, (1), 101-108.
283. Amundson, K. R.; Sapjeta, B. J.; Lovinger, A. J.; Bao, Z., An in-plane anisotropic organic semiconductor based upon poly (3-hexyl thiophene). *Thin Solid films* **2002**, 414, (1), 143-149.
284. Tuinstra, F.; Koenig, J. L., Raman spectrum of graphite *Journal of Chemical Physics* **1970**, 53, (3), 11261/5.
285. Ferrari, A. C.; Robertson, J., Interpretation of Raman spectra of disordered and amorphous carbon. *Physical Review B* **2000**, 61, (20), 14095-14107.
286. Pimenta, M. A.; Dresselhaus, G.; Dresselhaus, M. S.; Cancado, L. G.; Jorio, A.; Saito, R., Studying disorder in graphite-based systems by Raman spectroscopy. *Physical Chemistry Chemical Physics* **2007**, 9, (11), 1276-1290.

287. Baibarac, M.; Lapkowski, M.; Pron, A.; Lefrant, S.; Baltog, I., SERS spectra of poly (3-hexylthiophene) in oxidized and unoxidized states. *Journal of Raman Spectroscopy* **1998**, 29, (9), 825-832.
288. Iovu, M. C.; Sheina, E. E.; Gil, R. R.; McCullough, R. D., Experimental evidence for the quasi-“Living” nature of the grignard metathesis method for the synthesis of regioregular poly (3-alkylthiophenes). *Macromolecules* **2005**, 38, (21), 8649-8656.
289. Yamamoto, T.; Komarudin, D.; Arai, M.; Lee, B. L.; Sukanuma, H.; Asakawa, N.; Inoue, Y.; Kubota, K.; Sasaki, S.; Fukuda, T., Extensive studies on [pi]-stacking of poly (3-alkylthiophene-2, 5-diyl)s and poly (4-alkylthiazole-2, 5-diyl)s by optical spectroscopy, NMR analysis, light scattering analysis, and X-ray crystallography. *Journal of the American Chemical Society* **1998**, 120, (9), 2047-2058.
290. Ang, P. K.; Chen, W.; Wee, A. T. S.; Loh, K. P., Solution-gated epitaxial graphene as pH sensor. *Journal of the American Chemical Society* **2008**, 130, (44), 14392-14393.
291. Mohanty, N.; Berry, V., Graphene-based single-bacterium resolution biodevice and DNA transistor: Interfacing graphene derivatives with nanoscale and microscale biocomponents. *Nano Letters* **2008**, 8, (12), 4469-4476.
292. Fowler, J. D.; Allen, M. J.; Tung, V. C.; Yang, Y.; Kaner, R. B.; Weiller, B. H., Practical chemical sensors from chemically derived graphene. *ACS Nano* **2009**, 3, (2), 301-306.
293. Dan, Y.; Lu, Y.; Kybert, N. J.; Luo, Z.; Johnson, A. T., Intrinsic response of graphene vapor sensors. *Nano Letters* **2009**, 9, (4), 1472-1475.
294. Eda, G.; Chhowalla, M., Graphene-based composite thin films for electronics. *Nano Letters* **2009**, 9, (2), 814-818.
295. Pang, S.; Tsao, H. N.; Feng, X.; Müllen, K., Patterned graphene electrodes from solution-processed graphite oxide films for organic field-effect transistors. *Advanced Materials* **2009**, 21, (34), 3488-3491.
296. Lee, C. G.; Park, S.; Ruoff, R. S.; Dodabalapur, A., Integration of reduced graphene oxide into organic field-effect transistors as conducting electrodes and as a metal modification layer. *Applied Physics Letters* **2009**, 95, (2), 023304/3.
297. Lightcap, I. V.; Kosel, T. H.; Kamat, P. V., Anchoring semiconductor and metal nanoparticles on a two-dimensional catalyst mat. storing and shuttling electrons with reduced graphene oxide. *Nano Letters* **2010**, 10, (2), 577-583.
298. Zhang, K.; Zhang, L. L.; Zhao, X. S.; Wu, J., Graphene/polyaniline Nanofiber Composites as Supercapacitor Electrodes. *Chemistry of Materials* **2010**, 22, (4), 1392-1401.
299. Wu, Q.; Xu, Y.; Yao, Z.; Liu, A.; Shi, G., Supercapacitors based on flexible graphene/polyaniline nanofiber composite films. *ACS Nano* **2010**, 4, (4), 1963-1970.
300. Yin, Z.; Wu, S.; Zhou, X.; Huang, X.; Zhang, Q.; Boey, F.; Zhang, H., Electrochemical deposition of ZnO nanorods on transparent reduced graphene oxide electrodes for hybrid solar cells. *Small* **2010**, 6, (2), 307-312.
301. Liu, Z.; Liu, Q.; Huang, Y.; Ma, Y. F.; Yin, S. G.; Zhang, X. Y.; Sun, W.; Chen, Y. S., Organic photovoltaic devices based on a novel acceptor material: Graphene. *Advanced Materials* **2008**, 20, (20), 3924-3930.
302. Liu, Q.; Liu, Z.; Zhang, X.; Zhang, N.; Yang, L.; Yin, S.; Chen, Y., Organic photovoltaic cells based on an acceptor of soluble graphene. *Applied Physics Letters* **2008**, 92, (22), 223303/3.

303. Wu, J.; Becerril, H. A.; Bao, Z.; Liu, Z.; Chen, Y.; Peumans, P., Organic solar cells with solution-processed graphene transparent electrodes. *Applied Physics Letters* **2008**, *92*, (26), 263302/3.
304. Liu, Q.; Liu, Z.; Zhang, X.; Yang, L.; Zhang, N.; Pan, G.; Yin, S.; Chen, Y.; Wei, J., Polymer photovoltaic cells based on solution-processable graphene and P3HT. *Advanced Functional Materials* **2009**, *19*, (6), 894-904.
305. Yasmin, A.; Luo, J. J.; Daniel, I. M., Processing of expanded graphite reinforced polymer nanocomposites. *Composites Science and Technology* **2006**, *66*, (9), 1182-1189.
306. Ramanathan, T.; Abdala, A. A.; Stankovich, S.; Dikin, D. A.; Herrera-Alonso, M.; Piner, R. D.; Adamson, D. H.; Schniepp, H. C.; Chen, X.; Ruoff, R. S., Functionalized graphene sheets for polymer nanocomposites. *Nature Nanotechnology* **2008**, *3*, (6), 327-331.
307. Chen, G. H.; Wu, D. J.; Weng, W. G.; Yan, W. L., Preparation of polymer/graphite conducting nanocomposite by intercalation polymerization. *Journal of Applied Polymer Science* **2001**, *82*, (10), 2506-2513.
308. Ramanathan, T.; Stankovich, S.; Dikin, D. A.; Liu, H.; Shen, H.; Nguyen, S. T.; Brinson, L. C., Graphitic nanofillers in PMMA nanocomposites-An investigation of particle size and dispersion and their influence on nanocomposite properties. *Journal of Polymer Science-B-Polymer Physics Edition* **2007**, *45*, (15), 2097-2112.
309. Chen, G.; Weng, W.; Wu, D.; Wu, C., PMMA/graphite nanosheets composite and its conducting properties. *European polymer journal* **2003**, *39*, (12), 2329-2335.
310. Zheng, W.; Wong, S. C., Electrical conductivity and dielectric properties of PMMA/expanded graphite composites. *Composites Science and Technology* **2003**, *63*, (2), 225-235.
311. Huard, B.; Sulpizio, J. A.; Stander, N.; Todd, K.; Yang, B.; Goldhaber-Gordon, D., Transport measurements across a tunable potential barrier in graphene. *Physical Review Letters* **2007**, *98*, (23), 236803/4.
312. Zheng, W.; Wong, S. C.; Sue, H. J., Transport behavior of PMMA/expanded graphite nanocomposites. *Polymer* **2002**, *43*, (25), 6767-6773.
313. Chunder, A.; Liu, J.; Zhai, L., Reduced graphene oxide/poly (3-hexylthiophene) supramolecular composites. *Macromolecular Rapid Communications* **2009**, *31*, (4), 380-384.
314. Simon, J.; Andre, J. J., Molecular semiconductors: photoelectrical properties and solar cells. *NASA STI/Recon Technical Report A* **1985**, *86*, 21312.
315. Lever, A. B. P.; Hempstead, M. R.; Leznoff, C. C.; Liu, W.; Melnik, M., Recent studies in phthalocyanine chemistry. *Pure and Applied Chemistry* **1986**, *58*, (11), 1467-1476.
316. Zhang, X.; Feng, Y.; Tang, S.; Feng, W., Preparation of a graphene oxide-phthalocyanine hybrid through strong - interactions. *Carbon* **2009**, *48*, (1), 211-216.
317. Nalwa, H. S., *Handbook of organic conductive molecules and polymers: Conductive polymers: spectroscopy and physical properties*. John Wiley & Sons Inc: 1997; Vol. 1-4.
318. Hatton, R. A.; Blanchard, N. P.; Stolojan, V.; Miller, A. J.; Silva, S. R. P., Nanostructured copper phthalocyanine-sensitized multiwall carbon nanotube films. *Langmuir* **2007**, *23*, (11), 6424-6430.
319. Wang, Z.; Zhang, J.; Xing, R.; Yuan, J.; Yan, D.; Han, Y., Micropatterning of organic semiconductor microcrystalline materials and OFET fabrication by "Hot Lift Off". *Journal of the American Chemical Society* **2003**, *125*, (50), 15278-15279.

320. Bao, Z.; Lovinger, A. J.; Dodabalapur, A., Organic field effect transistors with high mobility based on copper phthalocyanine. *Applied Physics Letters* **1996**, 69, (26), 3066/3.
321. Tang, C. W., Two-layer organic photovoltaic cell. *Applied Physics Letters* **1986**, 48, (2), 183/3.
322. Brütting, W.; Bronner, M.; Gotzenbrugger, M.; Opitz, A. In *Ambipolar blends of Cu-Phthalocyanine and fullerene: Charge carrier mobility, electronic structure and their implications for solar cell applications*, 2008; Wiley-VCH Verlag GmbH, P. O. Box 10 11 61, Weinheim, D-69451, Germany: 2008; pp 38-42.
323. Opitz, A.; Bronner, M.; Brütting, W.; Himmerlich, M.; Schaefer, J. A.; Krischok, S., Electronic properties of organic semiconductor blends: ambipolar mixtures of phthalocyanine and fullerene. *Applied Physics Letters* **2007**, 90, (21), 212112/3.
324. Opitz, A.; Bronner, M.; Brütting, W., Ambipolar charge carrier transport in mixed organic layers of phthalocyanine and fullerene. *Journal of Applied Physics* **2007**, 101, (6), 063709/9.
325. Opitz, A.; Bronner, M.; Wagner, J.; Götzenbrugger, M.; Brütting, W. In *Ambipolar organic semiconductor blends for photovoltaic cells*, Proceedings of SPIE, 2008; 2008; p 70020J/9.
326. Nojiri, T.; Alam, M. M.; Konami, H.; Watanabe, A.; Ito, O., Photoinduced electron transfer from phthalocyanines to fullerenes (C60 and C70). *Journal of Physical Chemistry A* **1997**, 101, (43), 7943-7947.
327. Yang, F.; Shtein, M.; Forrest, S. R., Controlled growth of a molecular bulk heterojunction photovoltaic cell. *Nature Materials* **2005**, 4, 37-41.
328. Xue, J.; Rand, B. P.; Uchida, S.; Forrest, S. R., A hybrid planar-mixed molecular heterojunction photovoltaic cell. *Advanced Materials* **2005**, 17, (1), 66-71.
329. Uchida, S.; Xue, J.; Rand, B. P.; Forrest, S. R., Organic small molecule solar cells with a homogeneously mixed copper phthalocyanine: C60 active layer. *Applied Physics Letters* **2004**, 84, (21), 4218/2.
330. Peumans, P.; Bulovi, V.; Forrest, S. R., Efficient, high-bandwidth organic multilayer photodetectors. *Applied Physics Letters* **2000**, 76, (26), 3855/3.
331. Bobisch, C.; Wagner, T.; Bannani, A.; Möller, R., Ordered binary monolayer composed of two organic molecules: Copper-phthalocyanine and 3, 4, 9, 10-perylene-tetracarboxylic-dianhydride on Cu (111). *The Journal of Chemical Physics* **2003**, 119, (18), 9804/5.
332. Wang, Y.; Chen, H. Z.; Li, H. Y.; Wang, M., Fabrication of carbon nanotube/copper phthalocyanine composites with improved compatibility. *Material Science Engineering B* **2005**, 117, 296-301.
333. Shin, H. J.; Kim, S. M.; Yoon, S. M.; Benayad, A.; Kim, K. K.; Kim, S. J.; Park, H. K.; Choi, J. Y.; Lee, Y. H., Tailoring electronic structures of carbon nanotubes by solvent with electron-donating and-withdrawing groups. *Journal of the American Chemical Society* **2008**, 130, (6), 2062-2066.
334. Graupner, R.; Abraham, J.; Vencelová, A.; Seyller, T.; Hennrich, F.; Kappes, M. M.; Hirsch, A.; Ley, L., Doping of single-walled carbon nanotube bundles by Brønsted acids. *Physical Chemistry Chemical Physics* **2003**, 5, (24), 5472-5476.
335. De Wael, K.; Westbroek, P.; Bultinck, P.; Depla, D.; Vandenaabeele, P.; Adriaens, A.; Temmerman, E., Study of the deposition and Raman and XPS characterization of a metal ion tetrasulphonated phthalocyanine layer at gold surfaces: density functional theory

- calculations to model the vibrational spectra. *Electrochemistry Communications* **2005**, *7*, (1), 87-96.
336. Poenitzsch, V. Z.; Winters, D. C.; Xie, H.; Dieckmann, G. R.; Dalton, A. B.; Musselman, I. H., Effect of electron-donating and electron-withdrawing groups on peptide/single-walled carbon nanotube interactions. *Journal of the American Chemical Society* **2007**, *129*, (47), 14724-14732.
337. Rao, A. M.; Eklund, P. C.; Bandow, S.; Thess, A.; Smalley, R. E., Evidence for charge transfer in doped carbon nanotube bundles from Raman scattering. *Nature* **1997**, *388*, (6639), 257-259.
338. Das, A.; Pisana, S.; Chakraborty, B.; Piscanec, S.; Saha, S. K.; Waghmare, U. V.; Novoselov, K. S.; Krishnamurthy, H. R.; Geim, A. K.; Ferrari, A. C., Monitoring dopants by Raman scattering in an electrochemically top-gated graphene transistor. *Nature Nanotechnology* **2008**, *3*, (4), 210-215.
339. Lee, R. S.; Kim, H. J.; Fischer, J. E.; Thess, A.; Smalley, R. E., Conductivity enhancement in single-walled carbon nanotube bundles doped with K and Br. *Nature* **1997**, *388*, (6639), 255-256.
340. Watcharotone, S.; Dikin, D. A.; Stankovich, S.; Piner, R.; Jung, I.; Dommett, G. H. B.; Evmenenko, G.; Wu, S. E.; Chen, S. F.; Liu, C. P., Graphene-silica composite thin films as transparent conductors. *Nano Letters* **2007**, *7*, (7), 1888-1892.
341. Kong, B. S. G., J.; Jung, H.T., Layer-by-layer Assembly of Graphene and Gold Nanoparticles by Vacuum Filtration and Spontaneous Reduction of Gold Ions. *Chemical Communication* **2009**, 2174-2176.

LIST OF RELEVANT PUBLICATIONS

This dissertation is based in part on the following publications:

1. **A. Chunder**, T. Pal, S. Khondaker, L. Zhai, Reduced Graphene Oxide/Copper Phthalocyanine Composite and Its Optoelectrical Properties, *Journal of Physical Chemistry C*, 2010 (Submitted)
2. **A. Chunder**, J. Liu, L. Zhai, Reduced Graphene Oxide and Poly (3- hexylthiophene) Supramolecular Composite, *Macromolecular Rapid Communication*, 2010, 31, 380-384
3. **A. Chunder**, K. Etcheverry, L. Zhai, Fabrication of Antireflection Coatings on Plastics Using the Spraying Layer-by-layer Self-assembly Technique, *Journal of the Society for Information Display*, 2009, 17(4), 389-395
4. **A. Chunder**, K. Etcheverry, G. Londe, H. J. Cho, L. Zhai, Conformal Switchable Superhydrophobic/Hydrophilic Surfaces for Microscale Flow Control, *Colloids and Surfaces A: Physicochemical and Engineering Aspects*, 2008, 131(3), 187-193
5. **A. Chunder**, S. Sarkar, Y. Yu, L. Zhai, Fabrication of Ultrathin Polyelectrolyte Fibers and Their Controlled Release Properties, *Colloids and Surfaces B: Biointerfaces*, 2007, 58(2), 172-179
6. D. Joung, **A Chunder**, L. Zhai and S. I. Khondaker, High Yield Fabrication of Chemically Reduced Graphene Oxide Field Effect Transistors by Dielectrophoresis, *Nanotechnology*, 2010, 21(16), 165202
7. D. Joung, **A Chunder**, L. Zhai, S. Khondaker, Space charge limited conduction with exponential trap distribution in reduced graphene oxide sheets, *Applied Physics Letter*, 2010
8. G. Londe, **A. Chunder**, L. Zhai, H. J. Cho, An Analytical Model for the Wettability Switching Characteristic of a Nanostructured Thermoresponsive Surface, *Applied Physics Letter*, 2009, 94(16), 164104
9. G. Londe, **A. Chunder**, A. Wesser, L. Zhai, H. J. Cho, Microfluidic Valves Based on Superhydrophobic Nanostructures and Switchable Thermosensitive Surface for Lab-on-a-chip (LOC) Systems, *Sensors and Actuators B: Chemical*, 2008, B132 (2), 431-438
10. G. Londe, **A. Chunder**, A. Wesser, L. Zhai, H. J. Cho, A Nanostructured Thermosensitive Smart Surface with Integrated Microheater for Wettability Control, Proceedings of IMECE2008 ASME International Mechanical Engineering Congress and Exposition October 31 – November 6, 2008, Boston, Massachusetts, USA.
11. S. Sarkar, **A. Chunder**, W. Fei, L. An, L. Zhai, Superhydrophobic Mats of Polymer-derived Ceramic Fibers, *Journal of the American Ceramic Society* 2008, 91(8), 2751-2755

12. S. Ghosh, B. K. Sarker, **A. Chunder**, Position Dependent Photodetector from Large Area Reduced Graphene Oxide Thin Films, *Applied Physics Letter*, 2010, 96(16), 3415499/3
13. J. Zou, H. Chen, **A. Chunder**, Y. Yu, Q. Huo, L. Zhai, Preparation of a Superhydrophobic and Conductive Nanocomposite Coating from a Carbon-Nanotube-Conjugated Block Copolymer Dispersion, *Advanced Materials*, 2008, 20(17), 3337
14. Q. Li, J. Liu, J. Zou, **A. Chunder**, Y. Chen, L. Zhai, Synthesis and Electrochemical Performance of Multi-walled Carbon Nanotube/Polyaniline/MnO₂ Ternary Coaxial Nanostructures for Supercapacitors, *Journal of Power Sources*, 2010 (In press)
15. V. Dhir, A. Natarajan, M. Stanceescu, **A. Chunder**, N. Bhargava, M. Das, L. Zhai, P. Molnar, Patterning of Diverse Mammalian Cell Types in Serum Free Medium with Photoablation, *Biotechnology Progress*, 2008, 25(2), 594-603
16. **A. Chunder**, FD146: Section A; General Discussion, *Faraday Discussions*, 2010, XX, 1-23